Development of high resolution large-eddy simulation tools for assessment of turbulent flux measurements.

Zur Erlangung des akademischen Grades eines
DOKTOR-INGENIEURS
von der KIT-Fakultät für
Bauingenieur-, Geo- und Umweltwissenschaften

des Karlsruher Instituts für Technologie (KIT)
genehmigte
DISSERTATION
von
M.Sc. Sadiq Umar Abdul Huq
aus Chennai

Tag der mündlichen
Prüfung: 05.03.2024

Referent: Prof. Dr. Matthias Mauder
Korreferent: Prof. Dr. Olivier Eiff
Korreferent: Prof. Dr. Siegfried Raasch

Karlsruhe (2024)

Abstract

The exchange of energy, matter, and momentum between the Earth's surface and the atmosphere takes place in the atmospheric boundary layer. The eddy covariance (EC) is the most direct method of measuring this exchange. The accuracy of flux measured by this micrometeorological technique is crucial for subgrid parameterisation of numerical weather prediction models, and for forecasting trends in greenhouse gas emissions by earth system models. However, measured turbulent heat fluxes are often underestimated when compared to the total available energy, thus leading to the energy balance closure problem. This imbalance may be due to measurement errors associated with the anemometers, and the inability of single-tower point measurements in capturing the sub-mesoscale transport, among other reasons. In this thesis, these two potential sources of imbalance were evaluated by employing high-resolution large-eddy simulations (LES).

Sonic anemometers play a central role in EC as they provide velocity measurements necessary for flux calculations. In the absence of a reference calibration, the magnitude of error varies vastly across probe-induced flow distortion studies that rely on wind-tunnel tests or field intercomparisons. Under controlled conditions, the uncertainty in error quantification can be reduced by defining etalon in numerical experiments. The flow distortion errors of Campbell CSAT3, a widely used instrument for EC, was evaluated by LES in OpenFOAM®. In the simulations, oscillations to the velocity components were imposed at typical frequencies and amplitudes found in the surface-layer turbulence spectra. The simulations were repeated for different combinations of frequency, amplitude, azimuth angle, and angle-of-attack. The flow distortion, quantified by relative error of standard deviation between the virtual measurement and the input signal, ranged from 3 to 7% for the vertical velocity component depending on the azimuth angle. The frequency of wind speed oscillation was found to be of minor importance at amplitudes typical for surface-layer turbulence. Furthermore, two existing flow distortion correction approaches were evaluated. While both methods reduce error, they do not consider azimuth dependence of the flow distortion.

Sub-mesoscale transport can be investigated by LES only if the surface layer is sufficiently resolved ($O(1\text{ m})$). This order of high-resolution becomes prohibitively expensive to achieve with a single fixed resolution grid for the entire domain. To overcome this computational limitation an LES-within-LES, approach was developed in PALM. This vertical grid nesting enables a finer resolution near the surface, and a coarse resolution grid that resolves the entire atmospheric boundary layer. The two-way nesting algorithm modifies the existing third-order Runge-Kutta time stepping to exchange data between the two grids, and to concurrently integrate both grids in time. The top boundary condition for the nested fine grid is derived from coarse grid quantities and a feedback process updates coarse grid domain

at every time step in the overlapping region. The vertical nesting algorithm was validated with a reference simulation and the scalability on thousands of computational cores was also demonstrated.

Next, an LES study of the LITFASS-2003 campaign was conducted to investigate the energy balance closure in a heterogeneous landscape. A resolution of 1 m in the vertical direction was achieved by employing vertical grid nesting. The composite fluxes derived from field measurements provided lower boundary conditions for the simulation. To calculate ensemble statistics that separate heterogeneity-induced effects from turbulence fluctuations, multiple realisations of the simulation domain were required. The presence of secondary circulations in the surface layer was qualitatively demonstrated. Furthermore, the underestimation was found to be systematic and dependent on height. The dispersive fluxes, induced by secondary circulation, at a typical EC tower height of 10 m was found to be up to 5% of the composite flux prescribed at the surface. Notably, the high-resolution LES enabled the calculation of underestimation at a level previously not possible. However, the missing energy cannot be fully explained as the dispersive flux was much smaller than the imbalance found in field measurements.

Zusammenfassung

Der Austausch von Energie, Materie und Impulsen zwischen der Erdoberfläche und der Atmosphäre findet in der atmosphärischen Grenzschicht statt. Die Eddy-Kovarianz (EC) ist die direkteste Methode zur Messung dieses Austauschs. Die Genauigkeit der mit dieser mikrometeorologischen Technik gemessenen Flüsse ist von entscheidender Bedeutung für die Untergitter-Parametrisierung numerischer Wettervorhersagemodelle und für die Vorhersage von Trends bei Treibhausgasemissionen durch Erdsystemmodelle. Gemessene, turbulente Wärmeströme werden jedoch im Vergleich zur verfügbaren Gesamtenergie oft unterschätzt, was zu dem Problem des Energiebilanzabschlusses führt. Dieses Ungleichgewicht kann unter anderem auf Messfehler bei den Anemometern und auf die Unzulänglichkeit von Punktmessungen mit nur einem Turm zur Erfassung des submesoskaligen Transports zurückgeführt werden. In dieser Arbeit wurden diese beiden potenziellen Ursachen für das Ungleichgewicht mit Hilfe von hochauflösenden Large-Eddy-Simulationen (LES) untersucht.

Ultraschallanemometer spielen eine zentrale Rolle in der EC, da sie Geschwindigkeitsmessungen liefern, die für Flussberechnungen erforderlich sind. Da es keine Referenzkalibrierung gibt, variiert die Größe des Fehlers bei Studien zur sondeninduzierten Strömungsverzerrung, die sich auf Windkanaltests oder Feldvergleiche stützen, erheblich. Unter kontrollierten Bedingungen kann die Unsicherheit bei der Fehlerquantifizierung durch die Definition des Etalons in numerischen Experimenten verringert werden. Die Strömungsverzerrungsfehler von Campbell CSAT3, einem weit verbreiteten Instrument für EC, wurden mit LES in OpenFOAM® bewertet. Bei den Simulationen wurden den Geschwindigkeitskomponenten Oszillationen mit typischen Frequenzen und Amplituden aufgezwungen, die in den Turbulenzspektren der Oberflächenschicht zu finden sind. Die Simulationen wurden für verschiedene Kombinationen von Frequenz, Amplitude, Azimutwinkel und Anstellwinkel wiederholt. Die Strömungsverzerrung, quantifiziert durch den relativen Fehler der Standardabweichung zwischen der virtuellen Messung und dem Eingangssignal, lag für die vertikale Geschwindigkeitskomponente in Abhängigkeit vom Azimutwinkel zwischen 3 und 7%. Es wurde festgestellt, dass die Frequenz der Windgeschwindigkeitsoszillation bei Amplituden, die typisch für Oberflächenschichtturbulenz sind, von geringer Bedeutung ist. Außerdem wurden zwei bestehende Ansätze zur Korrektur von Strömungsverzerrungen bewertet. Beide Methoden verringern zwar den Fehler, berücksichtigen aber nicht die Azimutabhängigkeit der Strömungsverzerrung.

Der submesoskalige Transport kann mit LES nur untersucht werden, wenn die Oberflächenschicht ausreichend aufgelöst ist ($O(1\ \mathrm{m})$). Dieses hohe Auflösungsniveau ist mit einem einzigen Gitter mit fester Auflösung für das gesamte Gebiet nur mit unverhältnismäßig großem Aufwand zu erreichen. Um diese Berechnungsbeschränkung zu überwinden, wurde in PALM ein

LES-in-LES-Ansatz entwickelt. Diese vertikale Gitterverschachtelung ermöglicht eine feinere Auflösung in Oberflächennähe. Der Zwei-Wege-Schachtelungsalgorithmus modifiziert das bestehende Runge-Kutta-Zeitschrittverfahren dritter Ordnung, um Daten zwischen den beiden Gittern auszutauschen und beide Gitter zeitlich zu integrieren. Die obere Randbedingung für das feine Gitter wird aus den Größen des groben Gitters abgeleitet, und ein Rückkopplungsprozess aktualisiert den Bereich des groben Gitters bei jedem Zeitschritt in der überlappenden Region. Der vertikale Verschachtelungsalgorithmus wurde anhand einer Referenzsimulation validiert und die Skalierbarkeit auf Tausenden von Rechenkernen wurde ebenfalls nachgewiesen.

Als nächstes wurde eine LES-Studie der LITFASS-2003-Kampagne durchgeführt, um den Energiebilanzabschluss in einer heterogenen Landschaft zu untersuchen. Durch vertikale Verschachtelung des Gitters wurde eine Auflösung von 1 m in vertikaler Richtung erreicht. Die aus Feldmessungen abgeleiteten Flüsse lieferten die unteren Randbedingungen für die Simulation. Um Ensemble-Statistiken zu berechnen, die die heterogenitätsbedingte Effekte von Turbulenzfluktuationen trennen, waren mehrere Realisierungen des Simulationsbereichs erforderlich. Die Existenz von Sekundärzirkulationen in der Oberflächenschicht konnte qualitativ nachgewiesen werden. Außerdem wurde festgestellt, dass die Unterschätzung systematisch und höhenabhängig ist. Es wurde nachgewiesen, dass die durch die Sekundärzirkulation verursachten dispersiven Flüsse bei einer typischen EC-Turmhöhe von 10 m bis zu 5% des an der Oberfläche vorgeschriebenen Flusses betragen. Insbesondere die hochauflösende LES ermöglichte die Berechnung der Unterschätzung auf einem Niveau, das zuvor nicht möglich war. Die fehlende Energie kann jedoch nicht vollständig erklärt werden, da der dispersive Fluss viel kleiner war als das bei Feldmessungen festgestellte Ungleichgewicht.

Contents

Acknowledgements

First and foremost, I would like to extend my utmost gratitude to Matthias Mauder for his unfaltering support and for going above and beyond as my thesis supervisor. This work would not have been possible without him and it has been an absolutely rewarding experience to work with him.

I thank my colleague Frederik De Roo for the stimulating scientific discussions and, at the same time, for encouraging me to explore the stunning natural beauty of Garmisch-Partenkirchen.

Thanks to rest of the TABLe crew, Sha Zhang, Konstantin Kröniger, Fabian Eder, and Basit Khan, for the camaraderie and support during my doctoral studies. I also thank Matthias Zeeman, HaPe Schmid, and Gil Bohrer for the enjoyable conversations.

I would like to extend my thanks to Siegfried Raasch for hosting me at Hannover and for the invaluable support provided by his team.

In addition, I am indebted to Michael Manhart for introducing me to the field during my Masters and for motivating my doctoral research plans.

I am deeply grateful to my friends for their constant encouragement, to my grandparents, parents, and siblings for standing by me every step of the way. Finally, a special thanks to Nazia for being my stalwart supporter throughout this journey and for pushing me to cross the finish line.

List of manuscripts

This dissertation presented in cumulative form consists of three manuscripts. The manuscripts have been submitted to the peer-reviewed journals Boundary-Layer Meteorology, Geoscientific Model Development and Meteorologische Zeitschrift. The first two manuscripts have already been published and the third manuscript is currently under review.

Manuscripts included in this thesis:

Huq, S., Roo, F. D., Foken, T., & Mauder, M. (2017). Evaluation of probe-induced flow distortion of campbell CSAT3 sonic anemometers by numerical simulation. Boundary-Layer Meteorology, 165 (1), 9–28. https://doi.org/10.1007/s10546-017-0264-z

Huq, S., Roo, F. D., Raasch, S., & Mauder, M. (2019). Vertically nested LES for high-resolution simulation of the surface layer in PALM (version 5.0). Geoscientific Model Development, 12 (6), 2523–2538. https://doi.org/10.5194/gmd-12-2523-2019

Huq, S., De Roo, F., Sühring, M., Wanner, L., & Mauder, M. (2023). High-resolution ensemble LES energy balance closure study of the LITFASS-2003 campaign. Meteorologische Zeitschrift (under review).

1. Introduction

The atmospheric boundary layer (ABL), which is the lowest part of the troposphere, sustains life on Earth. The ABL facilitates the exchange of energy, mass, and momentum between the Earth's surface and the atmosphere. A comprehensive understanding of the energy budget of this biosphere-atmosphere exchange is vital for: parameterisation of unresolved scales in numerical weather prediction models; projection of future greenhouse gas concentrations (Rebmann et al., 2018); and atmospheric modelling in earth system models to study climate change. In the following sections, turbulence in the atmosphere and flux measurement methods in the surface layer are introduced. A brief overview of the energy balance closure (EBC) problem is described. The need and benefit of large-eddy simulations (LES) is presented. Lastly, the main objectives of this thesis are listed.

1.1. Turbulent flux measurements in the surface-layer

The ABL is defined by Stull (1988) as the part of the troposphere directly influenced by the Earth's surface. The solar radiation warms the Earth's surface thus leading to the development of the turbulent boundary layer. The ABL is classified as stable or unstable based on the atmospheric stratification; the processes studied in this thesis focus on the unstable convective boundary layer that is typical in the daytime. The convective boundary layer is further categorised by three layers, namely the surface layer, the mixed layer, and the entrainment zone (Stull, 1988). The terms micrometeorology and boundary layer meteorology are, at times, used interchangeably in older literature, but in its modern usage, the term refers to the study of turbulent time and space scales common in the atmospheric surface layer. Foken (2008a) defines atmospheric surface layer as the lowest 5-10% of the ABL with depths ranging from 0.5 to 2 km and time scale shorter than the diurnal cycle. The exchange of energy and gasses are quantified by fluxes calculated from their fluctuations.

The eddy-covariance (EC) is a direct method, i.e without the need for any empirical constants (Foken, 2008a), to measure the fluxes. The EC method works under the assumptions of Taylor's frozen eddy hypothesis (Taylor, 1938) and steady-state conditions. By invoking Reynolds decomposition, the covariance can be written as (Mauder et al., 2021) ,

$$F_s = \overline{ws} = \overline{w}\ \overline{s} + \overline{w's'} \tag{1.1}$$

where the overbar indicates sufficient time-averaging. By enforcing an additional requirement of horizontally homogeneous surface, the mean vertical velocity becomes zero. The

flux can thus be represented just by the covariance of the fluctuations, $\overline{w's'}$. The sonic anemometer (Fig. 1.1) plays a central role in the eddy covariance system. It enables measuring fluctuations of three components of velocity at a high frequency (10-20 Hz) to capture the turbulence spectrum. The errors associated with the sonic anemometers are discussed in the following section and also in Chapter 2.

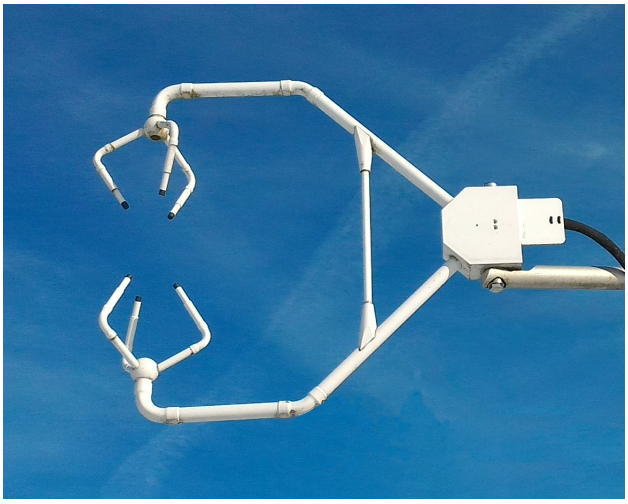

Figure 1.1.: A Campbell CSAT3 sonic anemometer deployed in the field. Modified after Huq et al. (2017) (Appendix B).

.

1.2. The Energy Balance Closure Problem

The net solar radiation (R_n) can be partitioned in to sensible (H), latent (LE) and ground (G) heat fluxes,

$$R_n = H + LE + G. \tag{1.2}$$

The energy balance is characterised as the ratio between the turbulent fluxes ($H + LE$) and the available energy ($R_n - G$). The energy balance is considered closed only if the ratio is one. However, multiple studies have reported underclosure (Oncley et al., 2007; Wilson et al., 2002; Franssen et al., 2010).

The many reasons for the underclosure have been critically reviewed by Culf et al. (2004), Foken (2008b), Leuning et al. (2012) and more recently by Mauder et al. (2020). The broad classification of the error according to Mauder et al. (2020) are instrument errors, data processing errors, sources of energy such as canopy heat storage that are not considered in Eq. 1.2, and more importantly, the sub-mesoscale transport. From the studies of Mauder et al. (2006) for the LITFASS-2003 field campaign and Mauder et al. (2007) for the EBEX-2003, Mauder et al. (2020) concludes that quality checks and appropriate corrections are important but they are not significant contributors to the energy imbalance. The canopy

heat storage term is found to be large for tall vegetation forest sites (Leuning et al., 2012) but this term is expected to be low for short vegetation.

The instrument inter-comparison conducted during the Energy Balance Experiment (EBEX-2000) by Oncley et al. (2007) did not find any systematic bias in open-path infrared hygrometers. The closed-path hygrometers, on the other hand, are prone to errors due to tube dampening (Halswanter et al., 2009). The net radiation measurement has also been improved by the use of pyranometer for the shortwave and pyregeometer for longwave radiation measurements (Mauder et al., 2020). The error related to ground heat flux can be minimized by installing the flux plates at appropriate depth and by recording high-resolution temperature profile (Liebethal et al., 2005). However, the measurement errors in velocity fluctuations by sonic anemometers is still a concern. The magnitude of error for the vertical velocity fluctuations is reported between 3 to 14% (Kochendorfer et al., 2012; Mauder, 2013; Frank et al., 2013; Horst et al., 2015). The wide error range is attributed to the probe-induce flow distortion which is also referred to as transducer-shadow effects. Since a measurement reference or etalon is not available, instrument intercomparisson experiments (Kaimal et al., 1990; Mauder et al., 2007) or wind-tunnel studies (Wieser et al., 2001) need to be conducted. The quasi-laminar inflow in wind-tunnels tend to overestimate the flow distortion. The field inter-comparison can only characterize whether the instruments are precise but the accuracy cannot be confirmed due to lack of an absolute reference (Horst et al., 2015). The Campbell CSAT3 anemometer has been adopted as the standard instrument in many long-term measurement networks FLUXNET (Baldocchi, 2014), ChinaFLUX (Yu et al., 2006) and TERENO (Zacharias et al., 2011). Therefore, an alternative numerical experiment evaluating the flow-distortion error in CSAT3 by large-eddy simulation is presented in Chapter 2.

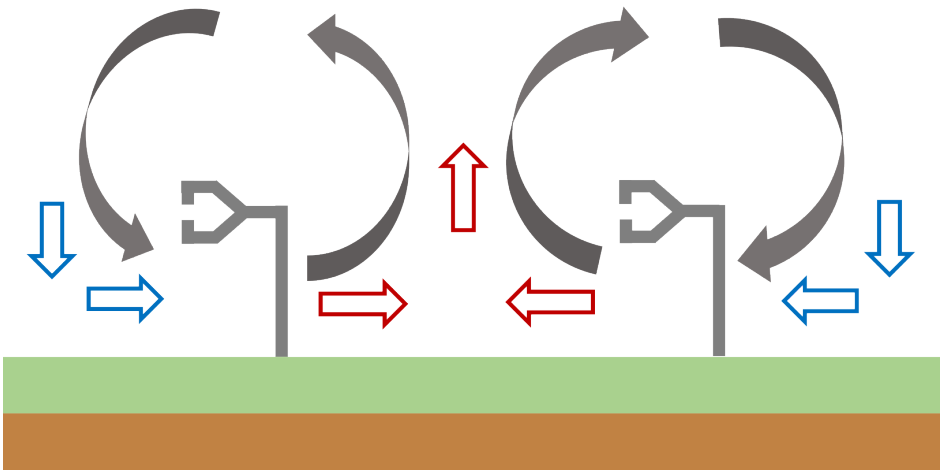

Figure 1.2.: Schematic of quasi-stationary turbulent organised structures (grey arrows). The warm (red) air transported upwards by secondary circulations appear as advection locally, with respect to the tower. These standing eddies that are not propagated by mean wind within the flux-averaging time frame will not be captured by single tower EC systems. Modified after Mauder et al. (2020) and Mauder et al. (2008).

The sub-mesoscale transport is believed to be the primary reason for the energy balance closure problem Mauder et al. (2020). Turbulence in the atmosphere is known to develop organized structures. Two common characteristic patterns found even over homogeneous surfaces are roll vortices and hexagonal cell-like structures. If these persistent large-scale structures are not transported by mean wind within the EC averaging time frame they cannot be captured by a single tower (Segal and Arritt, 1992; Etling and Brown, 1993). While in most cases, the presence of such structures is expected to lead to an underestimation of the measured heat flux, Prabha et al. (2007) show in an LES study that measurement in the vicinity of the roll vortices could even lead to an overestimation. Letzel and Raasch (2003) used the term thermally induced mesoscale circulations (TMC) to represent the secondary circulations that arise from the horizontal pressure gradient induced by differential heating in heterogeneous surface. A schematic of quasi-stationary structures and the inability of a single tower EC system to measure these eddies is depicted in Fig 1.2. Mauder et al. (2020) note that the secondary circulations manifest locally as advection and horizontal flux divergence, and non-locally as dispersive flux. Raupach and Shaw (1982) further emphasize the importance of dispersive fluxes arising from spatial covariance. Mahrt (1998) recommend spatial eddy covariance in addition to the temporal resolution of the EC to capture the large-scale low-frequency eddies. By adopting a multi-tower to calculate spatially-averaged fluxes, Mauder et al. (2010) confirm that a large portion of the energy residual can be explained by sub-mesoscale contribution. The systematic underestimation by EC measurements is also confirmed by large-eddy simulation studies of Kanda et al. (2004) and Huang et al. (2008).

1.3. Large-Eddy Simulation

Large Eddy Simulation (LES) is a powerful tool for the simulation of turbulence. LES has its origins in the study of atmospheric turbulence (Smagorinsky, 1963) but has also gained popularity in industrial applications. The most elegant method of solving the Navier-Stokes equations is the Direct Numerical Simulation (DNS) that resolves all turbulent scales. A typical Reynolds number (Re) for ABL flows is in the order of 10^7. The number of grid points needed by DNS is then roughly given by $Re^{\frac{9}{4}}$ (Fröhlich, 2006) which makes such a simulation computationally infeasible. The fundamental idea of LES is to resolve the large energy containing eddies and model the small scale motions. A schematic of turbulence spectrum in Fig. 1.3 shows the range of scales resolved and modelled by LES. While standard LES can satisfactorily resolve the ABL, the desired resolution in the surface-layer is a challenge. In such cases, an LES-within-LES presented in Chapter 2 will be beneficial. Unlike the field measurements, the LES numerical experiments can be executed in controlled conditions which are advantageous for parameter studies (Huang et al., 2008; De Roo and Mauder, 2018). Furthermore, the three-dimensional spatial realization of turbulence provides unparalleled insight to answer questions on the energy imbalance. Studies of Kanda et al. (2004) and Steinfeld et al. (2007) have been key in understanding the role of secondary circulations. Following these studies, Huq et al. (2023) (Appendix D) aims to evaluate the contribution of dispersive fluxes to the energy budget in the surface layer.

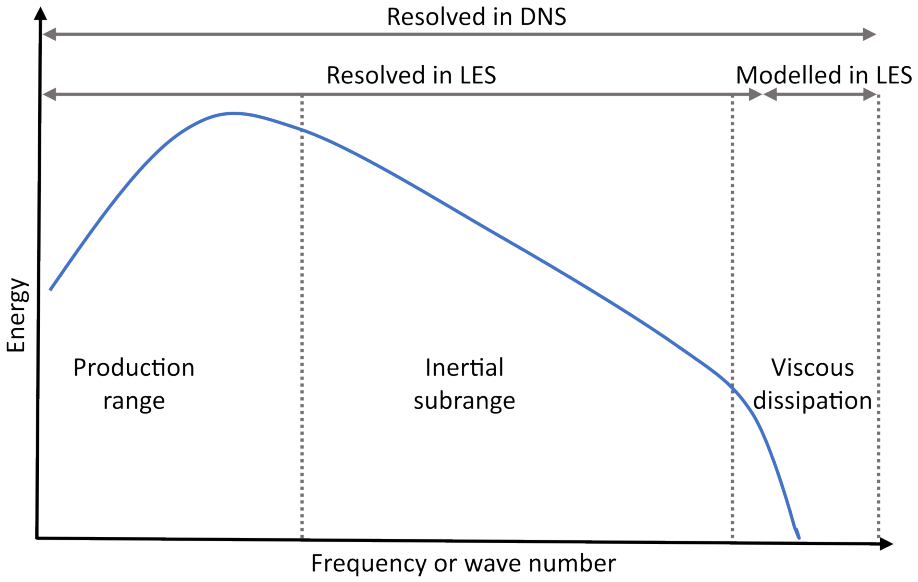

Figure 1.3.: Schematic of turbulence spectrum after Garratt (1994) and the scales resolved by Direct Numerical Simulation and Large-Eddy simulations after Fröhlich (2006).

1.4. Research objectives

The three main objectives of this thesis are: to evaluate probe-induced flow distortion; to develop a two-way nesting algorithm to achieve high resolution in the surface layer; and finally, to use this newly developed vertical nesting for high-resolution simulation to study how the sub-mesoscale transport contributes to energy imbalance in a realistic heterogeneous simulation. Firstly, Huq et al. (2017) (Appendix B) aim to address the following points

- the magnitude of the error due to probe-induced flow distortion,
- if vertical and horizontal velocity components are equally affected by the transducer shadow effect,
- dependence of the error on azimuth angle and angle-of-attack, and
- if the frequency of oscillation of the wind speed has any influence on the error.

Secondly, Huq et al. (2019) (Appendix C) develop an LES-within-LES model, validate the results and evaluate the computational efficiency. Lastly, Huq et al. (2023) (Appendix D) aim to

- find evidence for the presence of secondary circulations in the surface layer,
- understand spatial variability of the fluxes and energy balance,

- calculate dispersive fluxes in the surface layer to quantify the vertical transport by secondary circulations, and

- identify if there is an underclosure bias and find its dependence on height.

In the following chapter the set-up of the numerical experiments and the development of the vertical grid nesting method are described. In Chapter 3, the results of the three studies are presented and discussed. The major findings of this thesis are emphasized in Chapter 4.

2. Methods

To investigate the energy balance closure problem, two different large-eddy simulation models were employed. The influence of probe-induced flow distortion is investigated using OpenFOAM®, as the body-fitted mesh capability allows resolving the sonic anemometer geometry. On the other hand, PALM is suitable to study the sub-mesoscale transport in the atmospheric boundary layer. In the following section, the set-up of the numerical experiment for the flow distortion study is described. In the subsequent section, the development of vertical grid nesting algorithm and the high-resolution LES set-up of the LITFASS-2003 campaign are described.

2.1. Numerical simulation of probe-induced flow distortion

The open source computational fluid dynamics program OpenFOAM® (Weller et al., 1998) solves the discretised governing equations by finite-volume method. The LES subgrid-scale fluxes are modelled by an algebraic Smagorinsky model (Fureby et al., 1997). An implicit second-order backward scheme was chosen for the time integration and the PISO (Issa, 1986) procedure handles the pressure-velocity calculation since the flow is assumed to be incompressible. A conservative fixed time step was selected such that the Courant-Friedrichs-Lewy number does not exceed 1. The snappyHexMesh utility was used to generate the body-fitted mesh of the three-dimensional CSAT3 sonic anemometer geometry located within a numerical wind-tunnel that extends 1 m in all three directions. The 6.4 mm transducer pin was resolved by a 3 mm mesh and the mesh size was gradually relaxed to 12.5 mm near the boundaries. The simulation is made computationally feasible by assuming periodicity in the vertical (z) and spanwise (y) directions. An oscillating inflow in the streamwise direction (x) with frequency and amplitude selected from model spectra by Kaimal et al. (1972) provides fluctuations that are typical in the inertial-subrange. Mean streamwise direction wind speed (u) of 2 ms^{-1}, that is typically found at a height of 2 m in field measurements, and mean vertical velocity (w) of 0 ms^{-1} were chosen. Three sets of cases (X,Y and Z) are simulated as listed in Table 2.1. The cases are labelled such that two digits following the alphabet indicates the azimuth angle of the anemometer and the last two digits represent the angle-of-attack. The mesh generation process is repeated for each combination of azimuth angle and angle of attack, by rotating the geometry around the vertical axis for the former and rotating about the spanwise axis for the latter. The mean wind and amplitude are the same between X and Y case but w of Y oscillates at a higher frequency. The Z cases have a constant inflow signal. The objectives of the numerical experiments are to quantify the

Case	Azimuth angle (°)	Angle-of-attack (°)	Sine inflow signal
X0000	0	0	$\overline{u} = 2\,ms^{-1}$
X3000	30	0	$\overline{w} = 0\,ms^{-1}$
X6000	60	0	$u_{freq} = 0.1\,Hz$
X9000	90	0	$u_{amp} = 1\,ms^{-1}$
			$w_{freq} = 0.1\,Hz$
			$w_{amp} = 0.5\,ms^{-1}$
Y0000	0	0	$\overline{u} = 2\,ms^{-1}$
Y3000	30	0	$\overline{w} = 0\,ms^{-1}$
Y6000	60	0	$u_{freq} = 0.1\,Hz$
Y9000	90	0	$u_{amp} = 1\,ms^{-1}$
			$w_{freq} = 1.0\,Hz$
			$w_{amp} = 0.5\,ms^{-1}$
Z0000	0	0	$\overline{u} = 2\,ms^{-1}$
Z0005	0	5	$\overline{w} = 0\,ms^{-1}$
Z0025	0	25	$u_{amp} = 0\,ms^{-1}$
Z3000	30	0	$w_{amp} = 0\,ms^{-1}$
Z3005	30	5	
Z3025	30	25	
Z6000	60	0	
Z6005	60	5	
Z6025	60	25	
Z9000	90	0	
Z9005	90	5	
Z9025	90	25	

Table 2.1.: List of cases simulated by Huq et al. (2017) and the varying parameters: Azimuth angle, angle-of-attack and the velocity inflow amplitude and frequency.

magnitude of the error due to probe-induced flow distortion, to identify if both u and w are equally affected, dependence on azimuth angle and angle-of-attack, and the influence of wind speed fluctuation frequency (Huq et al. (2017) (Appendix B)).

The total simulated time is 70 s. After a spin-up of 10 s, which corresponds to one period of oscillation of u for X and Y cases, the data is captured for the next 60 s. Virtual measurements were recorded by 11 virtual probes in each of the three sonic paths, between the lower and corresponding upper transducer pins, with the midpoint being at the intersection of the three paths. The instantaneous velocity components are then calculated by averaging the measurements from the 33 probes. Three references were recorded to identify the appropriate reference or the etalon. A probe was placed 0.3 m in front of the transducer in the undisturbed region (AddProb), a reference simulation without any geometry in the domain (RefSim) and taking the input signal as the reference (InFlow). The distortion errors are then calculated for all three references. Finally, two existing transducer correction methods were validated. Both methods apply correction based on the angle (θ) between the velocity

vector and the transducer path. Kaimal et al. (1990) does not apply any correction for θ between 75 and 90 degrees (Eq.2.1). Horst et al. (2015) apply correction for all range of θ (Eq.2.2).

$$v_m = \begin{cases} v(0.85 + \frac{0.16\theta}{75}) & 0 \leq \theta \leq 75 \\ v & 75 \leq \theta \leq 90 \end{cases} \tag{2.1}$$

$$v_m = v(0.84 + 0.16sin\theta) \tag{2.2}$$

2.2. High-resolution LES in PALM: model development and simulation set-up

The Parallelized Large-eddy simulation Model (PALM) by Raasch and Schröter (2001) and Maronga et al. (2015) has been established as a valuable tool for ABL research. PALM solves the non-hydrostatic incompressible Navier-Stokes equations in the Boussinesq approximation by finite different method. The six prognostic equations solved by PALM are three components of velocity (u, v, w), potential temperature (θ), humidity (q) and the sub-grid scale kinetic energy (e). The equations discretised by a Cartesian grid are filtered over the grid volume. Following the convention of Maronga et al. (2015) the over bar denoting the filtered variables is omitted for readability except for the SGS fluxes that are denoted by double prime. Table 2.2 lists the symbols used in the following equations. The prognostic equations for conservation of mass, energy and moisture for the resolved variables read as

$$\frac{\partial u_i}{\partial t} = -\frac{\partial u_i\, u_j}{\partial x_j} - \varepsilon_{ijk} f_j u_k + \varepsilon_{i3k} f_3 u_{k_{\mathrm{g}},j} - \frac{1}{\rho_0}\frac{\partial \pi^*}{\partial x_i} + g\frac{\theta_{\mathrm{v}} - \langle\theta_{\mathrm{v}}\rangle}{\theta_{\mathrm{v}}}\delta_{i3} - \frac{\partial}{\partial x_j}\left(\overline{u_i'' u_j''} - \frac{2}{3}e\delta_{ij}\right), \tag{2.3}$$

$$\frac{\partial u_j}{\partial x_j} = 0, \tag{2.4}$$

$$\frac{\partial \theta}{\partial t} = -\frac{\partial u_j\, \theta}{\partial x_j} - \frac{\partial}{\partial x_k}\left(\overline{u_j'' \theta''}\right) - \frac{L_{\mathrm{V}}}{c_p \Pi}\Psi_{q_{\mathrm{v}}}, \tag{2.5}$$

$$\frac{\partial q_{\mathrm{v}}}{\partial t} = -\frac{\partial u_j\, q_{\mathrm{v}}}{\partial x_j} - \frac{\partial}{\partial x_k}\left(\overline{u_j'' q_{\mathrm{v}}''}\right) + \Psi_{q_{\mathrm{v}}}. \tag{2.6}$$

The LES sub-grid scales (SGS) are modelled according to Deardorff (1980) with modifications to 1.5 order closure parameterisation proposed by Moeng and Wyngaard (1988) and

Saiki et al. (2000) that assumes proportionality between the energy transport by the SGS eddies and the local gradients of the mean quantities. The prognostic equation for the sub-grid scale kinetic energy and the modelled SGS fluxes reads as

$$\frac{\partial e}{\partial t} = -u_j \frac{\partial e}{\partial x_j} - \left(\overline{u_i'' u_j''}\right) \frac{\partial u_i}{\partial x_k} + \frac{g}{\theta_{\mathrm{v},0}} \overline{u_3'' \theta_{\mathrm{v}}''} - 2K_m \frac{\partial e}{\partial x_j} - \epsilon \,, \tag{2.7}$$

$$\overline{u_i'' u_j''} - \frac{2}{3} e \delta_{ij} = -K_m \left(\frac{\partial u_i}{\partial x_j} + \frac{\partial u_j}{\partial x_i} \right) , \tag{2.8}$$

$$\overline{u_i'' \theta''} = -K_h \frac{\partial \theta}{\partial x_i} \,, \tag{2.9}$$

and

$$\overline{u_i'' q_v''} = -K_h \frac{\partial \theta}{\partial x_i} \,. \tag{2.10}$$

A complete description of the equations in PALM is found in Maronga et al. (2015).

Table 2.2.: Symbols in the governing equations. List modified after Huq et al. (2017) (Appendix B).

Symbol	Description
f_i	Coriolis parameter
ρ_0	Density of dry air at the surface
π^*	Modified perturbation pressure
g	Gravitational acceleration
θ_v	Virtual potential temperature
L_v	Latent heat of vaporization
C_p	Heat capacity of dry air at constant pressure
q_v	Specific humidity
Ψ_{q_v}	Source/sink term of q_v
Π	Exner function for converting between temperature and potential temperature
K_h	SGS eddy diffusivity of heat
K_m	SGS eddy diffusivity of momentum

The prognostic equations discretised on a staggered Arakawa C grid have the scalars evaluated at the center of the grid volume and the velocities evaluated at the faces. Advection terms can be evaluated with either a fifth-order upwind scheme (Wicker and Skamarock,

2002) or by a second order scheme (Piacsek and Williams, 1970). A third-order Runge-Kutta (RK3) scheme with three sub-steps (Williamson, 1980) integrates the discretised equations in time. The studies in the following sections apply periodic boundary conditions in the lateral boundaries enabling the use of an efficient Fast-Fourier Transform based pressure solver. The lower boundary condition for the horizontal momentum equation is derived by assuming Monin-Obukhov Similarity Theory (MOST) between the surface and the first grid point. PALM parallelises the solution process by decomposing the domain in to sub-domains and the data exchange between the processing cores is achieved via Message Passing Interface (MPI) library.

2.2.1. Vertically nested LES

An LES-within-LES method was developed by Huq et al. (2019) to achieve higher resolution in the surface layer. A coarse grid (CG) parent domain simulates the entire atmospheric boundary layer, while a fine grid (FG) child domain, with limited vertical extent, overlaps the parent domain at the surface. The horizontal extent of both the grids are identical, enabling the use of periodic conditions at the lateral boundaries. The nesting ratio, defined as the ratio of the CG spacing and the FG spacing, has to be an integer value but can be either an even or odd number. Schematic diagrams of the overlapping grid and an example of staggered grid for an odd nesting ratio is shown in Fig. 2.1.

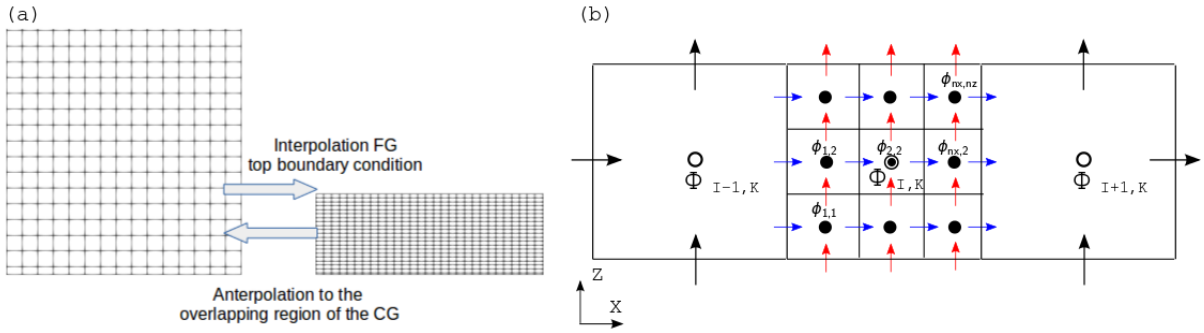

Figure 2.1.: (a) Schematic of the coarse resolution parent grid and the fine resolution child grid. The FG overlaps the CG at the bottom, the data exchange between the coarse grid and the fine grid are represented by arrows. CG sends the data needed for FG top boundary condition. The feedback from the FG updates the CG quantities. (b) Schematic of staggered Arakawa C grid, the larger cell represents the CG and the divided cell represents fine grid at a nesting ratio of 3. The horizontal and vertical arrows in black are CG velocity and pressure, respectively. Likewise, the coloured arrows represent FG velocities. The hollow and filled circles indicate CG and FG pressure, respectively. The scalar quantities of CG and FG are annotated with symbols Φ and ϕ, respectively. The indices I and K correspond to CG and the FG indices are indicated as a function of nesting ratio nx and nz in the x and y direction, respectively. Modified after Huq et al. (2019) (Appendix C).

The two-way nesting algorithm of Huq et al. (2019) starts with splitting the available compu-

tational cores defined by the user between the CG and FG. At time zero, CG is initialized by the standard LES approach and then the FG is initialized by interpolating the CG quantities. There is also a provision to delay the start of the nested simulation until the CG reaches a fully turbulent state. Both grids are concurrently integrated in time but are restricted to have identical time step. PALM automatically calculates the time step that satisfies the Courant-Friedrichs-Lewy condition individually for both grids and the more conservative value of the two is chosen by the nesting method. As shown in Fig. 2.2, the prognostic equations of both grids are first solved concurrently. The values of u,v,w,θ and q from the FG are then fed back to the CG; this process is referred to as 'anterpolation' by Sullivan et al. (1996). The coarse grid then solves the Poisson equation for pressure and updates the u,v,w,θ and q fields. At this stage, the top boundary condition for the FG is interpolated from the CG fields. The FG then solves the Poisson equation for pressure and anterpolates TKE to the CG. This process is repeated for the three Runge-Kutta 3 sub-steps. The interpolation of fields from CG to define the FG top boundary condition is performed according to Clark and Farley (1984) which satisfies conservation condition of Kurihara et al. (1979). The anterpolation from the FG to CG is done according to Clark and Hall (1991). The anterpolation of TKE needed special attention as the FG resolves the turbulence better and the SGS motion are weaker compared to CG (Sullivan et al., 1996). To preserve the sum of resolved kinetic energy and SGS kinetic energy, anterpolation of TKE maintains the Germano identity (Germano et al., 1991). The computational performance is improved by creating MPI derived data type that exchanges data arrays that are not contiguous in memory more efficiently.

To validate the nesting algorithm, a convective boundary layer simulation with two overlapping grids at a nesting ratio of 5 was designed by Huq et al. (2019) (Appendix C). The CG domain extends up to 1.65 km, the FG overlaps the CG but the vertical extent is limited to 320 m. Both grids have equal lateral extent allowing use of periodic boundary conditions in the lateral directions. Dirichlet condition is applied at the top and bottom for velocities with zero vertical velocity and the horizontal component is set to geostrophic wind. The pressure and humidity are set to zero gradient Neumann condition at the top and bottom. The potential temperature bottom boundary is set by gradient computed by MOST from the prescribed surface heat flux and roughness length. The simulation parameters are listed in Table 2.3. The two-way nesting algorithm is validated by comparing the results against two stand-alone reference simulations with same vertical extent as the CG. The reference with CG resolution is labelled SA-C and the other with FG resolution is labelled SA-F. The grid resolution and the number of grid points in the three simulations are listed in Table 2.4, SA-F has roughly 5 times more grid points than the nested CG and FG points combined.

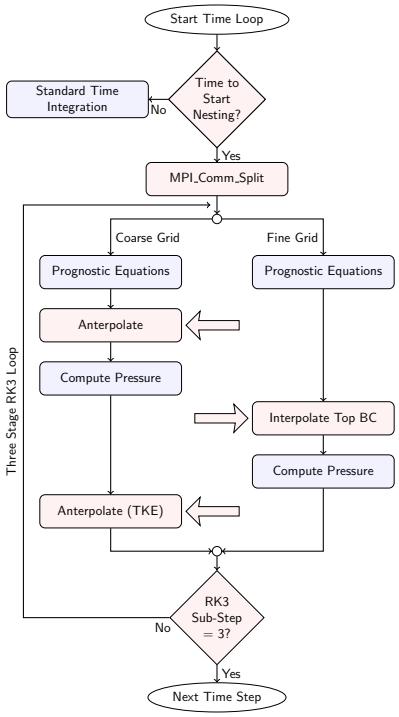

Figure 2.2.: The sequence of actions and the exchange of data executed by the two-way interaction algorithm visualised by a flowchart. The new routines implemented for the nesting are highlighted in red. Transfer data between the two grids is indicated by arrows. Figure modified after Huq et al. (2019) (Appendix C).

2.2.2. Simulation of LITFASS-2003 campaign

The LITFASS-2003 campaign over a heterogeneous land surface around the meteorological observatory in Lindenberg, Germany by Beyrich and Mengelkamp (2006) was designed to assess different area-averaging strategies of the surface flux. The campaign covered different land surface types and the local fluxes over these land surfaces were the focus of micro-meteorological measurements. Therefore, LITFASS-2003 provides an ideal dataset to study the energy balance closure problem in order to understand the influence of surface heterogeneity in inducing secondary circulations. Huq et al. (2023) selected a sub-region of this campaign consisting mostly of agricultural land with flat topography for this LES study. The vegetation classification shown in Fig. 2.3(a) is obtained from Coordinated Information on the European Environment (CORINE) dataset, published by the European Environment Agency, modified by Maronga and Raasch (2013). The simulation is driven by composite fluxes derived for 30 May 2003 from multiple energy balance stations by Beyrich et al. (2006). The composite fluxes available at 30 minute intervals are linearly interpolated as shown in Fig. 2.3(c and d). The simulated day was cloud free and characterized by weak Easterly geostrophic wind of 2 $\mathrm{m\,s^{-1}}$. By employing vertical nesting of Huq et al. (2019), a resolution of 1 m in the vertical and 2 m in the horizontal directions were achieved. Periodic boundary conditions are applied in the lateral direction. At the top boundary of the parent coarse grid, a Dirichlet condition of zero vertical velocity and horizontal velocity equal to

Table 2.3.: Connvective boundary layer simulation parameters to validate two-way nesting. List modified after Huq et al. (2019) (Appendix C).

Simulation Parameters	Value
Domain Size:	4.0 x 4.0 x 1.65 km^3
Fine grid vertical extent:	320 m
Kinematic surface heat flux:	$H_s = 0.1$ K m s^{-1}
Kinematic surface humidity flux:	$\lambda E_s = 4$ x 10^{-4} kg kg^{-1}m s^{-1}
Geostrophic wind:	$u_g = 1$ m s^{-1} , $v_g = 0$ m s^{-1}
Roughness length	0.1 m
Simulated time:	10800 s
Spin-up time:	9000 s
Averaging interval:	1800 s

Table 2.4.: Domain discretisation parameters of the validation simulation for nested grids, coarse and fine resolution reference. List modified after Huq et al. (2019) (Appendix C).

Case	No. of grid points	(dx,dy,dz) m	Grid points per CPU
Coarse Grid (CG)	200 x 200 x 80 = 3.2 x 10^6	20, 20, 20	1.6 x 10^5
Fine Grid (FG)	1000 x 1000 x 80 = 80 x 10^6	4, 4, 4	1.0 x 10^6
Total			
Standalone Coarse (SA-C)	200 x 200 x 80 = 3.2 x 10^6	20, 20, 20	1.6 x 10^5
Standalone Fine (SA-F)	1000 x 1000 x 400 = 400 x 10^6	4, 4, 4	1.0 x 10^6

geostrophic wind is applied. The fine child grid top boundary conditions are interpolated from the coarse grid. A Neumann condition for the scalar quantities, namely potential temperature, humidity, turbulent kinetic energy, and pressure, is applied at the top and bottom boundaries. A 3.5 hour period from 1030 to 1400 UTC was simulated. The initial 3 hours was considered as spin-up time for turbulence to develop. In the last 30 minutes, a conservative fixed timestep was used to capture data. To calculate ensemble statistics, multiple realisations of the domain were needed. The model was compiled with appropriate compiler flags for deterministic floating point operation and the initial perturbation imposed on the domain was controlled by a random seed. The five realisations are labelled LIT-A, LIT-B, LIT-C, LIT-D and LIT-E. The nested grid configuration and the simulation parameters are summarised in Table 2.5. A complete description of the simulation setup is presented in Huq et al. (2023) (Appendix D).

The energy balance ratio (EBR) is defined as the ratio of the turbulent flux to the prescribed surface flux reads as

$$EBR = \frac{\rho \cdot C_p \cdot \overline{w'\theta'} + \rho \cdot L_v \cdot \overline{w'q'}}{H_0 + LE_0}\,; \tag{2.11}$$

where ρ, C_p and L_v are air density, specific heat of air and latent heat of vaporisation, respectively, needed to convert the kinematic flux to dynamic flux. Following the convention

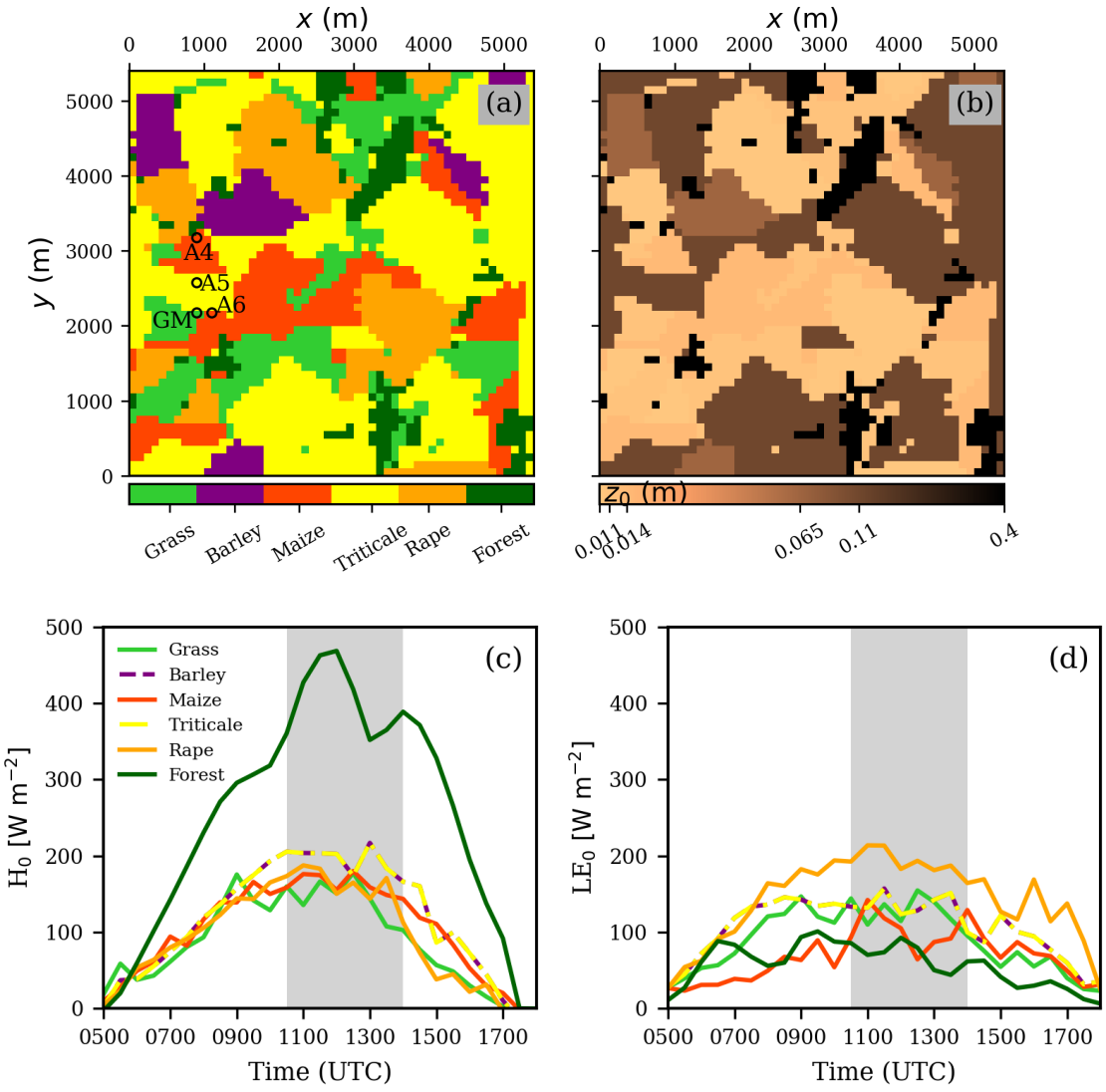

Figure 2.3.: The land surface classification derived from the CORINE dataset for the simulated area (a) and surface roughness (b). The composite surface fluxes of sensible (c) and latent (d) heat on the simulated day 30 May 2003. The period simulated in this study is shaded in grey. Composite flux for barley and triticale are identical but the surface roughness are not. Modified after Huq et al. (2023) (Appendix D).

Table 2.5.: LITFASS-2003 LES simulation parameters. Modified after Huq et al. (2023) (Appendix D.)

Simulation Parameters	**Value**
Parent domain size	5.4 x 5.4 x 2.2 km^3
Child grid vertical extent	72 m
Parent grid resolution (dx,dy,dz)	6 m, 6 m, 3 m
Child grid resolution (dx,dy,dz)	2 m, 2 m, 1 m
Surface heat flux, H_0	time-varying interpolated composite fluxes following Beyrich et al. (2006) (Fig. 2.3c)
Surface humidity flux, LE_0	time-varying interpolated composite fluxes following Beyrich et al. (2006) (Fig. 2.3d)
Geostrophic wind	$u_g = -2$ m s^{-1} (Easterly), $v_g = 0$ m s^{-1}
Roughness length	depending on vegetation type from CORINE dataset (Fig. 2.3b)
Density, ρ	1.204 Kg K^{-1}
Specific heat of air, C_p	1005 J Kg^{-1} K^{-1}
Latent heat of vaporization, L_v	$2.5 \cdot 10^6$ J Kg^{-1}
Simulated time	12600 s (10:30 UTC - 14:00 UTC)
Spin-up time	10800 s (13:30 UTC - 13:30 UTC)
Data capture & temporal-averaging interval	1800 s (13:30 UTC - 14:00 UTC)
Number of realisations for ensemble statistics, N	5

of Huq et al. (2023), the double prime, single prime, angle brackets and asterisk denote SGS flux, temporal fluctuation, horizontal spatial mean and deviation from spatial mean, respectively. Time-averaged turbulent flux (covariance of temporal fluctuations) was not a standard output in PALM 4.0. Therefore, an user code calculated the total flux at each time step and the time-averaged total flux was written at the end of the 30-minute averaging period.

$$\overline{w\theta} = \overline{w \cdot \theta + w"\theta"} \,. \tag{2.12}$$

The sensible heat flux was then calculated from the total flux, $\overline{w}$, and $\overline{\theta}$ as

$$\overline{w'\theta'} = \overline{w\theta} - \overline{w} \cdot \overline{\theta} \,. \tag{2.13}$$

The dispersive sensible flux (H_{disp}) was computed as,

$$\langle \overline{w^*}\,\overline{\theta^*} \rangle = \langle (\overline{w} - \langle \overline{w} \rangle) \cdot \left(\overline{\theta} - \langle \overline{\theta} \rangle \right) \rangle \,; \tag{2.14}$$

Similarly, by replacing θ with specific humidity, q in the above equations, the vertical latent heat fluxes and dispersive latent heat fluxes (LE_{disp}) were calculated. The mean of the heat flux from all the realisation results in the ensemble-averaged fluxes,

$$H_{ens} = \rho \cdot C_p \cdot \frac{1}{N} \sum_{i=1}^{N} \overline{w'\theta'}_i, \tag{2.15}$$

and

$$LE_{ens} = \rho \cdot L_v \cdot \frac{1}{N} \sum_{i=1}^{N} \overline{w'q'}_i \,. \tag{2.16}$$

The ensemble-averaged EBR was obtained by calculating mean of the EBR of all realisations since the 30-minute averaged surface flux in the denominator of equation 2.17 is identical in all the runs.

$$EBR_{ens} = \frac{1}{N} \sum_{i=1}^{N} EBR_i. \tag{2.17}$$

3. Results and Discussion

The results of the LES simulations from Chapter 2 are presented and objectively discussed in this chapter. The evaluated probe-induced flow distortion errors from numerical experiments and potential methods to correct for the errors are presented in the following section. In the subsequent sections, the vertical nesting algorithm is validated and the results of the simulation of the LITFASS-2003 campaign are presented.

3.1. Evaluation of probe-induced flow distortion

The wake behind the transducer pin in Fig 3.1 is inclined at an angle closer to the angle of attack of the inflow at the visualised instance. In general, the wake enters the sonic measurement path only at large angle-of-attack and the majority of the measurement volume is undisturbed except for the region in the immediate vicinity of the transducer. The mean vertical velocity calculated from the 33 virtual probes agrees well with the input signal for all cases as seen in Fig. 3.2. However, the mean u-component only shows agreement for the X and Y cases, and the Z cases with zero angle-of-attack. The relative error of standard deviation is a better measure to quantify the flow-distortion since only the turbulent fluctuations are relevant for EC technique. The standard deviation errors relative to RefSim, AddProb and Inflow for the vertical velocity are shown in Table 3.1. The error starts from 3% and increases up to 7% with the increase in azimuth angle. Comparing, X0000, the case with lowest error, with Y0000 shows the error also increases marginally with increase in frequency of oscillation. The errors calculated with different reference data only have negligible differences. Applying the corrections of Kaimal et al. (1990) and Horst et al. (2015) reduce the error.

Friebel et al. (2009) show that the CSAT3 anemometer errors are significant only for wind sector of 160 to 200 degrees which is in good agreement with this numerical experiment. Kochendorfer et al. (2012) estimated 14% in a field study with tilted CSAT3 anemometer which has been previously disputed by other field intercomparison studies (Mauder et al., 2007; Loescher et al., 2005) as noted by Mauder (2013). This study too finds no evidence for such high error for the standard-deviation of the w-component. The relative error in the range of between 3-5% reported by Horst et al. (2015) is similar to the estimates of this study.

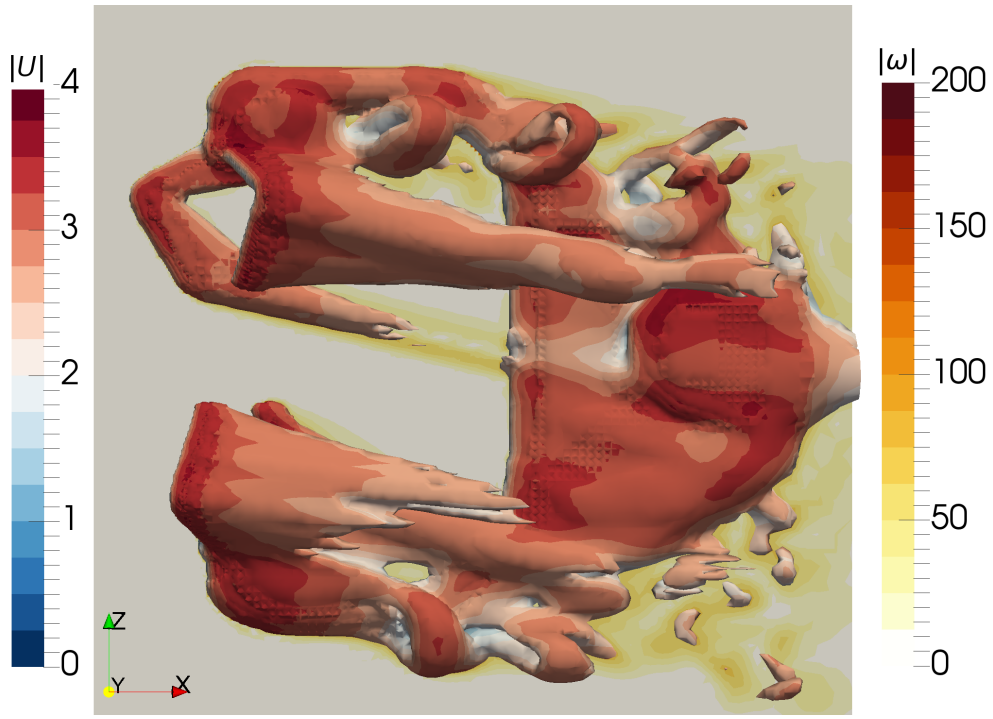

Figure 3.1.: Isosurface of the magnitude of instantaneous vorticity at time = 63 s is colored by velocity magnitude for case Y0000. The vorticity magnitude of X-Z slice is shown in the background. The wake of the transducer pin and the supporting structure are noticeable. Modified after Huq et al. (2017) (Appendix B).

Additionally, from a field intercomparison of two vertically mounted CSAT3 anemometers with two horizontally mounted CSAT3, Frank et al. (2013) found the contribution of flow distortion error to the vertical fluxes to be less for the horizontally mounted configuration. This is in agreement with Huq et al. (2017) where they show that the relative error of the standard deviation of w is twice as large as that of the u component (data not shown). Furthermore, the corrections of Kaimal et al. (1990) and Horst et al. (2015) correct by about 1-3% of the error but do not fully compensate for the error. One reason for the remaining errors could be explained by the lack of azimuth-angle dependence in the correction factors.

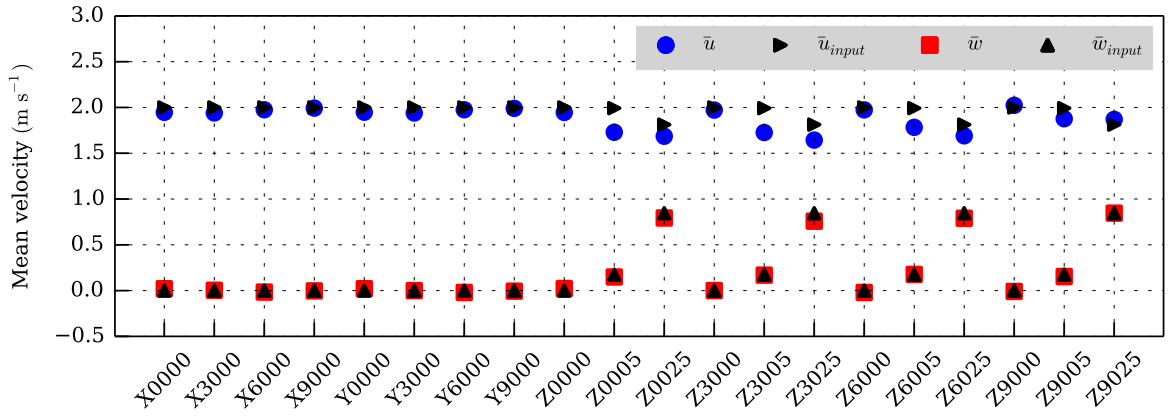

Figure 3.2.: Mean velocity of the u- and w- components from the virtual probes and the mean inflow velocities. Modified after Huq et al. (2017) (Appendix B).

Case	$\boldsymbol{RE\sigma_w}$ **(RefSim)**	$\boldsymbol{RE\sigma_w}$ **(AddProb)**	$\boldsymbol{RE\sigma_w}$ **(InFlow)**	$\boldsymbol{RE\sigma_{w,Kaimal}}$	$\boldsymbol{RE\sigma_{w,Horst}}$
X0000	3.13	3.20	3.48	1.95	0.37
X3000	5.98	6.07	6.32	3.35	2.72
X6000	6.33	6.39	6.67	2.68	2.56
X9000	7.16	7.32	7.50	5.14	3.97
Y0000	4.93	4.62	4.97	3.13	1.44
Y3000	6.91	6.59	6.95	4.3	3.46
Y6000	5.18	4.87	5.21	1.93	1.7
Y9000	6.78	6.57	6.82	4.48	3.13

Table 3.1.: The error of the standard deviation of the w-component relative to three different reference measurements. And the last two columns are the relative errors after applying the corrections. Modified after Huq et al. (2017) (Appendix B).

3.2. Validation of vertical grid nesting

The validity of the nesting algorithm is confirmed by plotting the vertical heat flux profile which is the most important quantity calculated by EC technique. PALM calculates turbulent fluctuations (w'', θ'') as the spatial deviation from the instantaneous horizontal average. The covariance of the spatial fluctuations are then horizontally averaged (denoted by angle brackets) and also averaged in time (denoted by overbar) to arrive at the heat flux ($\langle\overline{w''\theta''}\rangle$). The vertical profiles in Fig. 3.3 are normalised by the surface fluxes. In the surface layer, a good agreement between the FG profile and SA-F is found for both resolved and SGS fluxes. In the region above the FG, the CG agrees with the reference simulations. The ability of the nested grid to resolve turbulence scales is verified by analysing the spectra shown in Fig. 3.4. The fine grid SGS TKE spectra is in good agreement with the reference SA-F for all wave numbers.

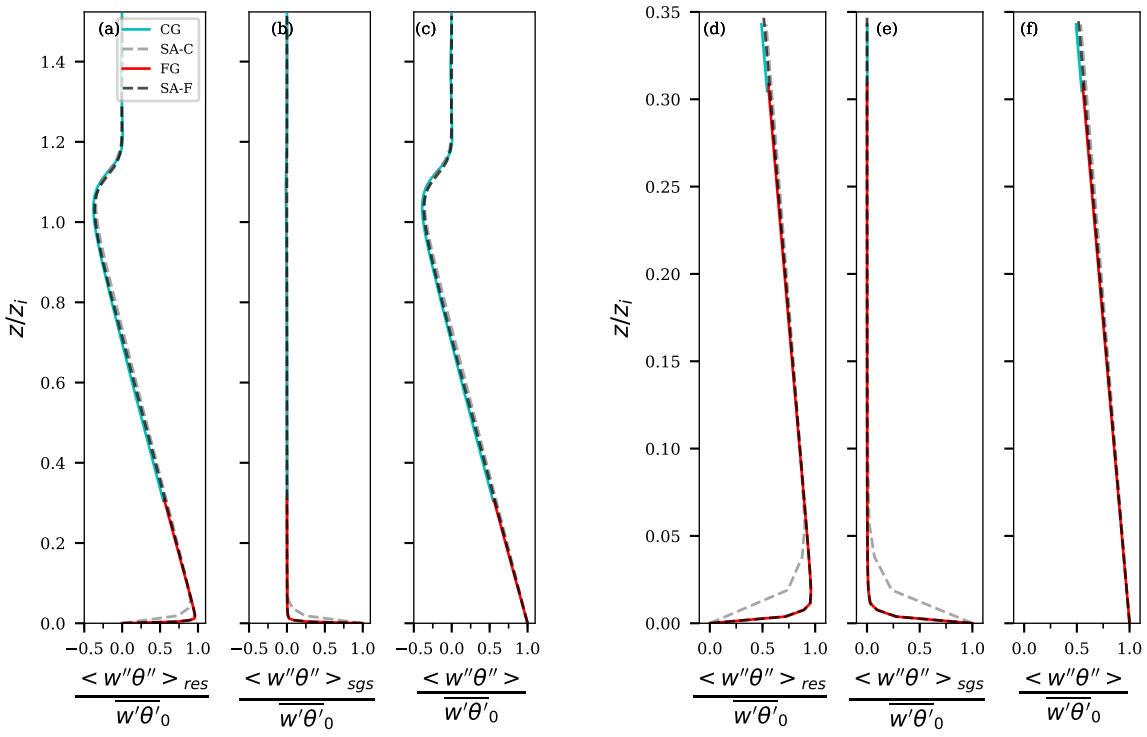

Figure 3.3.: Vertical profile of the heat flux for the full domain (a,b and c) and a zoomed-in view of the surface layer (d,c and f). The heat flux is horizontally averaged and normalised by the surface heat flux. The resolved (a and d), sub-grid (b and e), and total flux (c and f) profiles are visualised. The two-way nested FG (red) is in good agreement with the stand-alone reference simulation (SA-F, black) for the resolved and SGS fluxes and consequently, for the total flux. Modified after Huq et al. (2019) (Appendix C.)

The FG velocity spectra too is in good agreement with SA-F for higher wave numbers and at the peak. As expected, at lower wave numbers the velocity spectra follows the coarse reference (SA-C) as the largest eddies are only resolved by CG. The coarse grid spectra of

both SGS TKE and w at levels beyond the FG are in good agreement with the reference simulation. Further validation of the FG top boundary condition and SGS turbulent kinetic energy are discussed in Huq et al. (2019). A comparable accuracy between the FG and SA-F in the surface layer is achieved while drastically reducing the memory requirement since SA-F needs 5 times more grid points. Huq et al. (2019) perform another set of simulations to demonstrate the scalability of the algorithm on up to 15000 CPU cores.

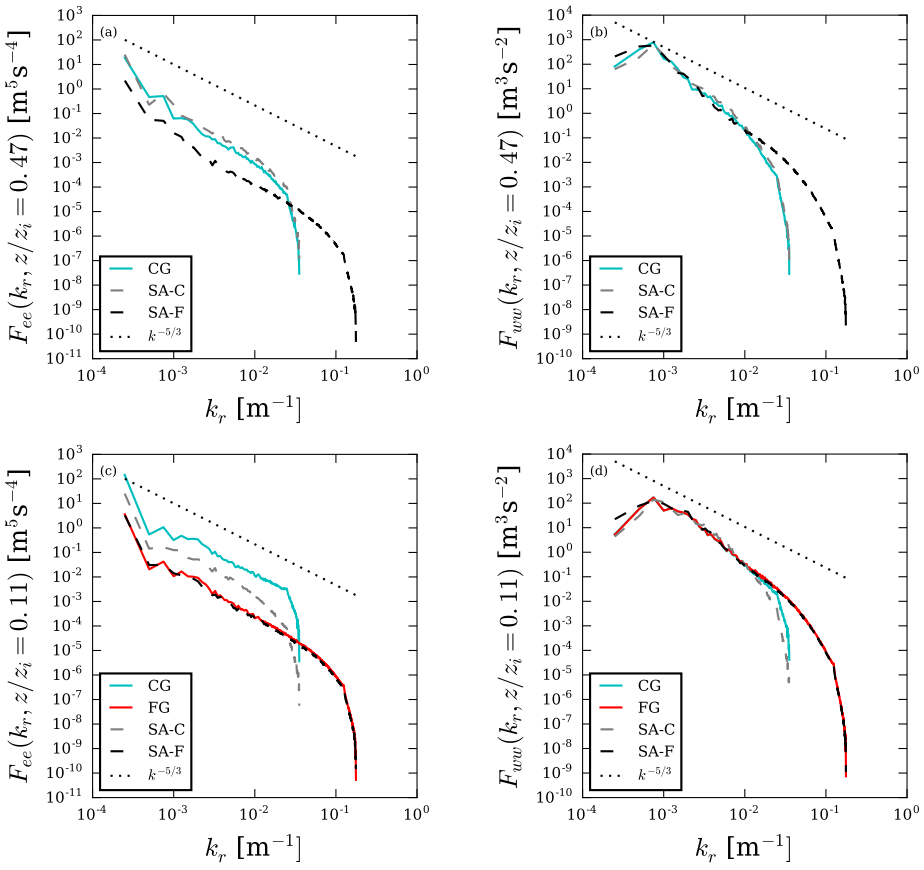

Figure 3.4.: The SGS turbulent kinetic energy (e) spectra (a and c), and vertical velocity (w) spectra (b and d) at $z/z_i = 0.47$ beyond the FG vertical extent (a and b) and at $z/z_i = 0.11$ in the surface layer(c and d); k_r is the horizontal wavenumber. The FG spectra is in good agreement with the stand-alone reference (SA-F) in the surface layer for both e and w. In the CG, at levels above the FG extent the spectra follows the coarse stand-alone reference (SA-C) as expected. Modified after Huq et al. (2019) (Appendix C.)

3.3. Energy balance closure analysis of LITFASS-2003 campaign

The high-resolution LES performed to study the energy balance closure in a heterogeneous landscape is presented in this section. Only results at or above a height of 10 m is analysed since the near-wall turbulence is parameterised, the lowest few grid points tend to be unreliable which is a general limitation of LES. The vertical resolution has been a limiting factor in other studies which inhibits the visualisation of the turbulent structures in the surface layer (De Roo et al. (2018). Along with the grid resolution, the aspect ratio of the grid volume is also important as high aspect ratio grids are not suitable for isotropic subgrid models. This study strikes a good balance with the resolution of 1 m in the vertical and 2 m in the lateral directions. Another limitation is drawing conclusions from the results of one realisation of the domain even as Maronga and Raasch (2013) have illustrated the need for ensemble-averaging to separate the heterogeneity-induced signals from turbulent fluctuations. While more realisations will lead to better statistics, the computational cost is a limiting factor which also restricted this study to only 5 realisations. Huq et al. (2023) have demonstrated the presence of structures in the surface layer that persist even after sufficient time-averaging and ensemble-averaging, This is qualitative evidence for the existence of the secondary circulation in the surface layer (data not shown).

The sensible heat fluxes, latent heat flux and EBR at a height of 10 m are shown in Fig. 3.5 for one realisation LIT-C and for the ensemble-averaged. The heat fluxes at this vertical level still correlate with the surface heterogeneity; this is in agreement with Maronga and Raasch (2013) where they simulated the same day of the LITFASS-2003 campaign. The turbulent fluctuations have not vanished even after 30-minute time averaging as it is evident from the heat flux plots that appear noisy. On the contrary, most of the noise has vanished after ensemble-averaging. The benefit of ensemble-averaging is evident from the EBR in Fig. 3.5(f) where the areas of overestimation and underestimation are concentrated at the edges of the land use type patches. The probability density function (PDF) of the time-averaged and ensemble-averaged heat fluxes normalised by the surface fluxes and of the EBR are shown in Fig. 3.6. The peak and the median of the heat fluxes decrease with height and the median is below one for all cases. The systematic underclosure and dependence on height is further emphasised by the tail to the left. No observable dependence on height or overclosure is noticeable in the tail to the right except for the latent heat flux which shows marginal dependence with height. The shape of the EBR PDF resembles that of the sensible heat flux. The vertical transport by secondary circulation is characterised by dispersive flux. The dispersive flux normalised by surface flux in Fig. 3.7 clearly shows both H_{disp} and LE_{disp} increase with height. Though the trend is same for all ensemble members, the variability between the members highlights the importance of ensemble-averaging in studying heterogeneity-induced effects. At a height of 10 m, the H_{disp} and LE_{disp} are 2% and 5% respectively. Previous LES studies have not found significant underestimation at this height likely due to limited grid resolution.

This study has quantified the dispersive flux at 10 m height. However, the magnitude is

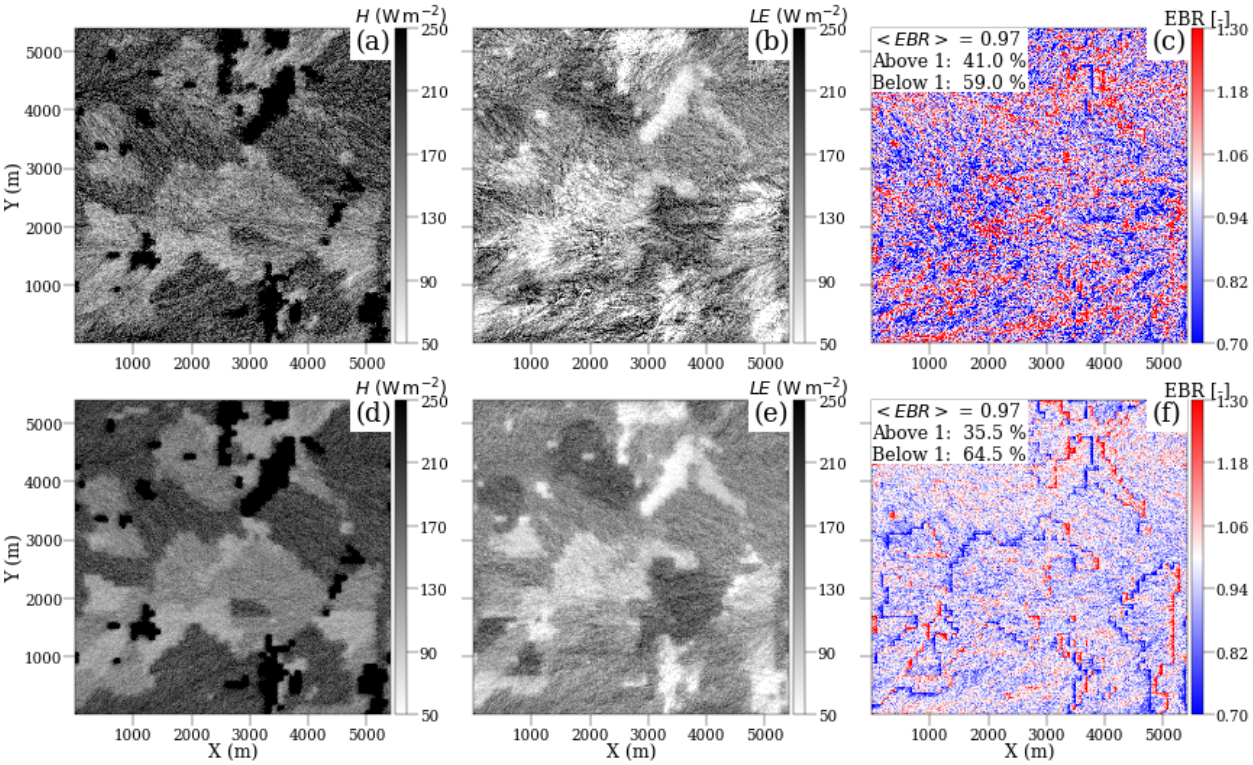

Figure 3.5.: Spatial plot of time-averaged sensible heat flux (a,d), latent heat flux (b,e) and EBR (c,f)of one realisation LIT-C (top) and the ensemble average of all realisation (bottom) at a height of 10 m. The pattern of fluxes still show characteristics of the underlying surface heterogeneity at this height. After ensemble-averaging, EBR (f) clearly shows areas of under- and overestimation which are more pronounced near the edge of land-use classes. Modified after Huq et al. (2023) (Appendix D).

still smaller compared to the imbalance found at this level in EC measurements. If a finer resolution LES will capture more secondary circulation in the surface layer is an open question. Reasons other than the secondary circulations should also be considered as the factors influence the energy balance residual, for example energy storage, flux footprint etc.. The feedback between secondary circulation and surface temperature cannot be captured if the simulation is driven by prescribing surface fluxes, thus a land-surface model should be included to consider this coupling. The reason for the dispersive latent heat flux being higher than the dispersive sensible heat flux in this study is not clear. One potential explanation is entrainment of dry air that causes different response to the secondary circulation. Nevertheless, the greater contribution of mesoscale fluxes to the latent heat flux was also observed by Maronga and Raasch (2013) in their simulation of the LITFASS-2003 experiment. On the contrary, for a heterogenous landscape in Canada, Eder et al. (2014) reported mesoscale energy transport contributed equally to the sensible and latent heat flux. Therefore, the partitioning could be be dependent on other factors like the heterogeneity of the landscape and meteorological conditions.

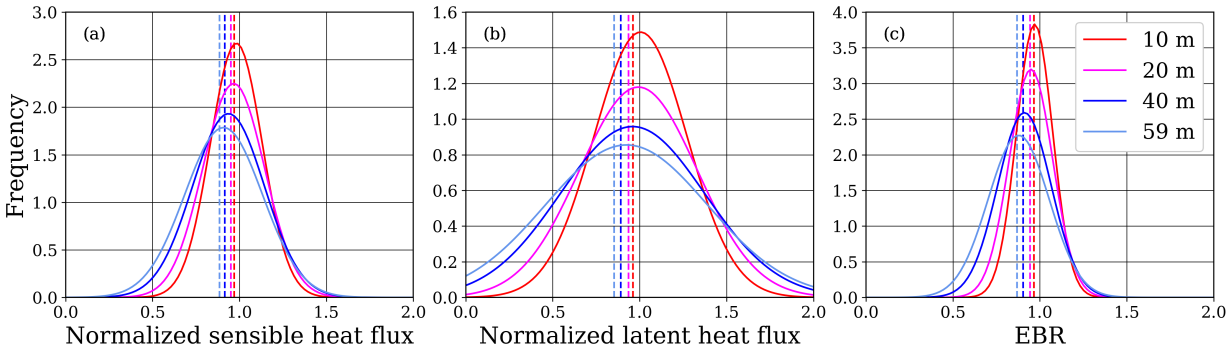

Figure 3.6.: The horizontal variability characterised by probability density function at different height levels of the time-averaged and ensemble-averaged sensible heat flux (a) and latent heat flux (b), normalised by the respective surface flux and the EBR (c) at different vertical levels. The median (dashed lines) is below one for all quantities at all height levels. The systematic underestimation and its dependence on height is noticeable from the spread in the left tail and also from the peaks shifting further below one. Modified after Huq et al. (2023) (Appendix D).

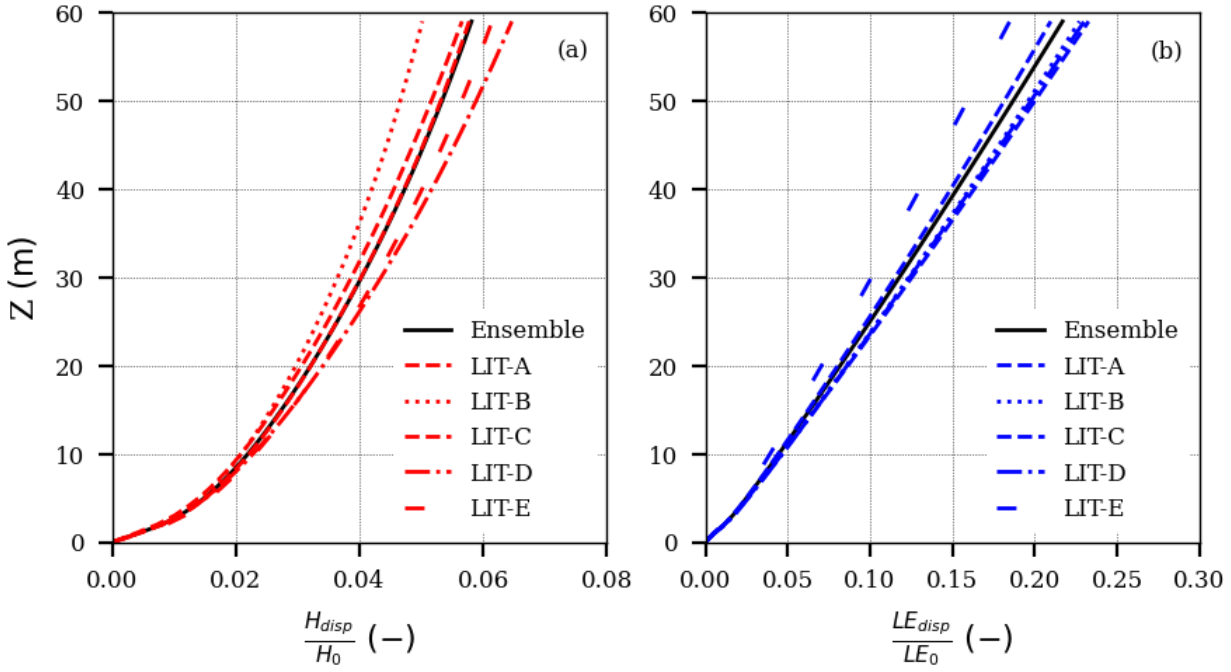

Figure 3.7.: Dispersive sensible (a) and latent (b) heat fluxes normalised by surface fluxes is a key quantity to characterize secondary circulations that are not captured by single point measurement. The dispersive flux increases with height for both H_{disp} and LE_{disp}, this trend is shared by all realisations including the ensemble-averaged profile. LE_{disp} shows stronger increase with height compared to H_{disp}. At a height of 10 m LE_{disp} is 5% of the latent heat flux at the surface. Modified after Huq et al. (2023) (Appendix D).

4. Conclusions

This thesis sheds light on the energy balance closure problem through three large-eddy simulation studies. While there are many reasons theorised to be contributing factors for the energy imbalance (Foken (2008b), Leuning et al. (2012), Mauder et al. (2020)), this thesis focussed on two commonly considered reasons, namely errors in velocity measurements due to probe-induced flow distortion and the inability of single tower eddy-covariance to capture the sub-mescoscale fluxes.

Probe-induced flow distortion of Campbell CSAT3 sonic anemometer was studied in a numerical wind tunnel by employing LES in OpenFOAM®. The region close to the transducer pin was resolved at millimetre resolution since the dampening effect caused by drag in the first few millimetres of the virtual measurement path was suspected to be the source of the anemometer measurement error. The inflow velocity components were imposed by oscillations at frequencies and amplitudes typically found in the surface-layer turbulence spectra, and the values were chosen from model spectra by Kaimal et al. (1972). The inflow signal provides a better representation of turbulence in the atmospheric boundary layer than a quasi-laminar steady flow conditions of wind-tunnel tests. Additionally, the inflow signal and measurements of the undisturbed flow serve as an absolute reference or etalon which are not available for field intercomparison experiments. Huq et al. (2017) (Appendix B) show that the error is spectrum-independent for wind fluctuations of magnitude that are typical for surface-layer turbulence. Therefore, atmospheric stability and measurement height do not play a significant role in measurement errors which is in agreement with Horst et al. (2015). The probe-induced dampening effect, depending on the azmimuth angle, for w-fluctuations was found to be 3 to 7% while u-fluctuations errors were only 1 to 3%. Consequently, mounting the anemometer horizontally could potentially reduce the dampening effect for the w-component which is in agreement with Frank et al. (2013). The correction proposed by Horst et al. (2015) reduces the magnitude of the error considerably but the correction does not consider the azimuth dependence. The error in scalar fluxes, for example, heat and CO_2 fluxes, will be of the same magnitude as the standard deviation of the w component. The above results are applicable only for CSAT3. The numerical experiment designed in this study should be repeated for other models of sonic anemometer to formulate instrument specific flow-distortion correction and such experiments may also help in structural design of new anemometers.

An LES-within-LES algorithm was developed to enable high-resolution ($O(1$ m$)$) in the surface layer at a reasonable computational cost. In this approach, a fine grid with limited vertical extent sits on top of a coarse grid in the surface layer. The concurrently parallel two-way interaction algorithm integrates both the grids in time. The interpolation and

anterpolation methods are energy-conserving. The anterpolation of the turbulent kinetic energy follows the Germano identity to conserve the total kinetic energy (Germano et al., 1991; Sullivan et al., 1996). The sequence of actions and data exchange between the grids at every Runge-Kutta-3 sub-step ensure numerical stability. A Message Passing Interface derived data type was created for efficient communication of data that are not contiguous in memory. Huq et al. (2019) (Appendix C) demonstrate the scalability of the algorithm on up to 15000 computational cores. The nesting scheme is validated by a convective boundary layer simulation. The vertical temperature flux in the surface layer shows perfect agreement with the reference stand alone simulation. The spectra of subgrid-scale turbulent kinetic energy and vertical velocity too show good agreement for the fine grid in the surface layer, while needing only one-fourth of the computational resources of the reference simulation. This nested version of PALM has also been successfully used by De Roo et al. (2018) to achieve high-resolution in the surface layer.

Energy balance closure in a heterogeneous landscape was studied by LES simulation of the LITFASS-2003 campaign. The surface-layer was resolved by a resolution of 1 m in the vertical and 2 m in the horizontal directions by employing nested grids. The heterogeneity effects were isolated from the turbulence fluctuations by calculating ensemble averages from five realisations of the domain. Huq et al. (2023) (Appendix D) demonstrated the presence of turbulent structures in the surface layer that do not vanish even after time and ensemble-averaging. The influence of the secondary circulation on the energy imbalance was evaluated by calculating dispersive flux at 10 m height. At that height, dispersive flux account for up to 5% of the prescribed surface fluxes. The magnitude of dispersive flux indicates that Taylor's frozen turbulence hypothesis may not always be valid in the surface layer and this translates directly into an underestimation of the fluxes measured by single-tower eddy covariance systems. However, this magnitude cannot fully explain the imbalance as it is much lower than the imbalance of about 15% on average found at many sites (Foken et al., 2010; Stoy et al., 2013). This study also found that underclosure is more prevalent than overclosure. The underclosure increases with height and can be as large as 20% at 60 m height for dispersive latent heat flux. The high spatial resolution in this study has enabled evaluation of energy balance closure in the surface layer. However, this study is still limited in the duration simulated due to computational resource constraints. The simulation of a diurnal cycle will enable more meaningful comparison of the virtual measurements with field measurements. The influence of time-averaging period and footprint of the fluxes can then be more effectively studied. To answer the question of energy partitioning and to evaluate local advection, a control volume approach can be beneficial (De Roo and Mauder, 2018; Eder et al., 2015). Additionally, a land-surface model should be included in future studies to consider the potential feedback between the secondary circulations and surface fluxes.

Bibliography

Baldocchi, D. (2014). Measuring fluxes of trace gases and energy between ecosystems and the atmosphere – the state and future of the eddy covariance method. *Global Change Biology*, 20(12):3600–3609.

Beyrich, F., Leps, J.-P., Mauder, M., Bange, J., Foken, T., Huneke, S., Lohse, H., Lüdi, A., Meijninger, W. M. L., Mironov, D., Weisensee, U., and Zittel, P. (2006). Area-averaged surface fluxes over the litfass region based on eddy-covariance measurements. *Boundary-Layer Meteorology*, 121(1):33–65.

Beyrich, F. and Mengelkamp, H.-T. (2006). Evaporation over a heterogeneous land surface: EVA_GRIPS and the LITFASS-2003 experiment—an overview. *Boundary-Layer Meteorology*, 121(1):5–32.

Clark, T. L. and Farley, R. D. (1984). Severe downslope windstorm calculations in two and three spatial dimensions using anelastic interactive grid nesting: A possible mechanism for gustiness. *J Atmos Sci*, 41:329–350.

Clark, T. L. and Hall, W. D. (1991). Multi-domain simulations of the time dependent navier stokes equation: Benchmark error analyses of nesting procedures. *J Comput Phys*, 92:456–481.

Culf, A. D., Foken, T., and Gash, J. H. C. (2004). *The Energy Balance Closure Problem*, page 159–166. Springer Berlin Heidelberg.

De Roo, F. and Mauder, M. (2018). The influence of idealized surface heterogeneity on virtual turbulent flux measurements. *Atmospheric Chemistry and Physics*, 18(7):5059–5074.

De Roo, F., Zhang, S., Huq, S., and Mauder, M. (2018). A semi-empirical model of the energy balance closure in the surface layer. *PLOS ONE*, 13(12):e0209022.

Deardorff, J. W. (1980). Stratocumulus-capped mixed layers derived from a three-dimensional model. *Bound.-Lay. Meteorol.*, 18:495–527.

Eder, F., Roo, F. D., Kohnert, K., Desjardins, R. L., Schmid, H. P., and Mauder, M. (2014). Evaluation of two energy balance closure parametrizations. *Boundary-Layer Meteorology*, 151(2):195–219.

Eder, F., Roo, F. D., Rotenberg, E., Yakir, D., Schmid, H. P., and Mauder, M. (2015). Secondary circulations at a solitary forest surrounded by semi-arid shrubland and their impact on eddy-covariance measurements. *Agricultural and Forest Meteorology*, 211-212:115–127.

Etling, D. and Brown, R. A. (1993). Roll vortices in the planetary boundary layer: A review. *Boundary-Layer Meteorology*, 65(3):215–248.

Foken, T. (2008a). *Micrometeorology*. Springer, Berlin, Germany, 2008 edition.

Foken, T. (2008b). The energy balance closure problem: An overview. *Ecological Applications*, 18(6):1351–1367.

Foken, T., Mauder, M., Liebethal, C., Wimmer, F., Beyrich, F., Leps, J.-P., Raasch, S., DeBruin, H. A. R., Meijninger, W. M. L., and Bange, J. (2010). Energy balance closure for the LITFASS-2003 experiment. *Theoretical and Applied Climatology*, 101(1-2):149–160.

Frank, J. M., Massman, W. J., and Ewers, B. E. (2013). Underestimates of sensible heat flux due to vertical velocity measurement errors in non-orthogonal sonic anemometers. *Agricultural and Forest Meteorology*, 171–172:72–81.

Franssen, H. H., Stöckli, R., Lehner, I., Rotenberg, E., and Seneviratne, S. (2010). Energy balance closure of eddy-covariance data: A multisite analysis for european fluxnet stations. *Agricultural and Forest Meteorology*, 150(12):1553–1567.

Friebel, H. C., Herrington, T. O., and Benilov, A. Y. (2009). Evaluation of the flow distortion around the campbell scientific csat3 sonic anemometer relative to incident wind direction. *Journal of Atmospheric and Oceanic Technology*, 26(3):582–592.

Fröhlich, J. (2006). *Large Eddy Simulation turbulenter Strömungen*. Vieweg & Teubner, Wiesbaden, Germany, 2006 edition.

Fureby, C., Tabor, G., Weller, H. G., and Gosman, A. D. (1997). A comparative study of subgrid scale models in homogeneous isotropic turbulence. *Physics of Fluids*, 9(5):1416–1429.

Garratt, J. R. (1994). *Cambridge atmospheric and space science series: The atmospheric boundary layer*. Cambridge University Press, Cambridge, England.

Germano, M., Piomelli, U., Moin, P., and Cabot, W. H. (1991). A dynamic subgrid scale eddy viscosity model. *Phys. Fluid A*, 3:7.

Halswanter, A., HAMMERLE, A., and WOHLFAHRT, G. (2009). Open-path vs. closed-path eddy covariance measurements of the net ecosystem carbon dioxide and water vapour exchange: A long-term perspective. *Agricultural and Forest Meteorology*, 149(2):291–302.

Horst, T. W., Semmer, S. R., and Maclean, G. (2015). Correction of a non-orthogonal, three-component sonic anemometer for flow distortion by transducer shadowing. *Boundary-Layer Meteorology*, 155(3):371–395.

Huang, J., Lee, X., and Patton, E. G. (2008). A modelling study of flux imbalance and the influence of entrainment in the convective boundary layer. *Boundary-Layer Meteorology*, 127(2):273–292.

Huq, S., De Roo, F., Sühring, M., Wanner, L., and Mauder, M. (2023). High-resolution ensemble les energy balance closure study of the litfass-2003 campaign. *Meteorologische Zeitschrift (under review)*.

Huq, S., Roo, F. D., Foken, T., and Mauder, M. (2017). Evaluation of probe-induced flow distortion of campbell CSAT3 sonic anemometers by numerical simulation. *Boundary-Layer Meteorology*, 165(1):9–28.

Huq, S., Roo, F. D., Raasch, S., and Mauder, M. (2019). Vertically nested LES for high-resolution simulation of the surface layer in PALM (version 5.0). *Geoscientific Model Development*, 12(6):2523–2538.

Issa, R. (1986). Solution of the implicitly discretised fluid flow equations by operator-splitting. *Journal of Computational Physics*, 62(1):40–65.

Kaimal, J. C., Gaynor, J. E., Zimmerman, H. A., and Zimmerman, G. A. (1990). Minimizing flow distortion errors in a sonic anemometer. *Boundary-Layer Meteorology*, 53(1-2):103–115.

Kaimal, J. C., Wyngaard, J. C., Izumi, Y., and Coté, O. R. (1972). Spectral characteristics of surface-layer turbulence. *Quarterly Journal of the Royal Meteorological Society*, 98(417):563–589.

Kanda, M., Inagaki, A., Letzel, M. O., Raasch, S., and Watanabe, T. (2004). LES study of the energy imbalance problem with eddy covariance fluxes. *Boundary-Layer Meteorology*, 110(3):381–404.

Kochendorfer, J., Meyers, T. P., Frank, J., Massman, W. J., and Heuer, M. W. (2012). How well can we measure the vertical wind speed? implications for fluxes of energy and mass. *Boundary-Layer Meteorology*, 145(2):383–398.

Kurihara, Y., Tripoli, G. J., and Bender, M. A. (1979). Design of a movable nested-mesh primitive equation model. *Monthly Weather Review*, 107(3):239–249.

Letzel, M. O. and Raasch, S. (2003). Large eddy simulation of thermally induced oscillations in the convective boundary layer. *Journal of the Atmospheric Sciences*, 60(18):2328–2341.

Leuning, R., van Gorsel, E., Massman, W. J., and Isaac, P. R. (2012). Reflections on the surface energy imbalance problem. *Agricultural and Forest Meteorology*, 156:65–74.

Liebethal, C., Huwe, B., and Foken, T. (2005). Sensitivity analysis for two ground heat flux calculation approaches. *Agricultural and Forest Meteorology*, 132(3–4):253–262.

Loescher, H., Ocheltree, T., Tanner, B., Swiatek, E., Dano, B., Wong, J., Zimmerman, G., Campbell, J., Stock, C., Jacobsen, L., Shiga, Y., Kollas, J., Liburdy, J., and Law, B. (2005). Comparison of temperature and wind statistics in contrasting environments among different sonic anemometer–thermometers. *Agricultural and Forest Meteorology*, 133(1–4):119–139.

Mahrt, L. (1998). Flux sampling errors for aircraft and towers. *Journal of Atmospheric and Oceanic Technology*, 15(2):416–429.

Maronga, B., Gryschka, M., Heinze, R., Hoffmann, F., Kanani-Sühring, F., Keck, M., Ketelsen, K., Letzel, M. O., Sühring, M., and Raasch, S. (2015). The parallelized large-eddy simulation model (palm) version 4.0 for atmospheric and oceanic flows: model formulation, recent developments, and future perspectives. *Geoscientific Model Development*, 8(8):2515–2551.

Maronga, B. and Raasch, S. (2013). Large-eddy simulations of surface heterogeneity effects on the convective boundary layer during the litfass-2003 experiment. *Boundary-Layer Meteorology*, 146(1):17–44.

Mauder, M. (2013). A comment on "how well can we measure the vertical wind speed? implications for fluxes of energy and mass" by kochendorfer et al. *Boundary-Layer Meteorology*, 147(2):329–335.

Mauder, M., Desjardins, R. L., Pattey, E., Gao, Z., and van Haarlem, R. (2008). Measurement of the sensible eddy heat flux based on spatial averaging of continuous ground-based observations. *Boundary-Layer Meteorology*, 128(1):151–172.

Mauder, M., Desjardins, R. L., Pattey, E., and Worth, D. (2010). An attempt to close the daytime surface energy balance using spatially-averaged flux measurements. *Boundary-Layer Meteorology*, 136(2):175–191.

Mauder, M., Foken, T., Aubinet, M., and Ibrom, A. (2021). *Eddy-Covariance Measurements*, pages 1473–1504. Springer International Publishing, Cham.

Mauder, M., Foken, T., and Cuxart, J. (2020). Surface-energy-balance closure over land: A review. *Boundary-Layer Meteorology*.

Mauder, M., Liebethal, C., Göckede, M., Leps, J.-P., Beyrich, F., and Foken, T. (2006). Processing and quality control of flux data during litfass-2003. *Boundary-Layer Meteorology*, 121(1):67–88.

Mauder, M., Oncley, S. P., Vogt, R., Weidinger, T., Ribeiro, L., Bernhofer, C., Foken, T., Kohsiek, W., De Bruin, H. A. R., and Liu, H. (2007). The energy balance experiment ebex-2000. part ii: Intercomparison of eddy-covariance sensors and post-field data processing methods. *Boundary-Layer Meteorology*, 123(1):29–54.

Moeng, C.-H. and Wyngaard, J. C. (1988). Spectral analysis of large-eddy simulations of the convective boundary layer. *J. Atmos. Sci.*, 45:3573–3587.

Oncley, S. P., Foken, T., Vogt, R., Kohsiek, W., DeBruin, H. A. R., Bernhofer, C., Christen, A., Gorsel, E. v., Grantz, D., Feigenwinter, C., Lehner, I., Liebethal, C., Liu, H., Mauder, M., Pitacco, A., Ribeiro, L., and Weidinger, T. (2007). The energy balance experiment ebex-2000. part i: overview and energy balance. *Boundary-Layer Meteorology*, 123(1):1–28.

Piacsek, S. A. and Williams, G. P. (1970). Conservation properties of convection difference schemes. *J. Comput. Phys.*, 198:500–616.

Prabha, T. V., Karipot, A., and Binford, M. W. (2007). Characteristics of secondary circulations over an inhomogeneous surface simulated with large-eddy simulation. *Boundary-Layer Meteorology*, 123(2):239–261.

Raasch, S. and Schröter, M. (2001). Palm - a large-eddy simulation model performing on massively parallel computers. *Meteorologische Zeitschrift*, 10(5):363–372.

Raupach, M. R. and Shaw, R. H. (1982). Averaging procedures for flow within vegetation canopies. *Boundary-Layer Meteorology*, 22(1):79–90.

Rebmann, C., Aubinet, M., Schmid, H., Arriga, N., Aurela, M., Burba, G., Clement, R., De Ligne, A., Fratini, G., Gielen, B., Grace, J., Graf, A., Gross, P., Haapanala, S., Herbst, M., Hörtnagl, L., Ibrom, A., Joly, L., Kljun, N., Kolle, O., Kowalski, A., Lindroth, A., Loustau, D., Mammarella, I., Mauder, M., Merbold, L., Metzger, S., Mölder, M., Montagnani, L., Papale, D., Pavelka, M., Peichl, M., Roland, M., Serrano-Ortiz, P., Siebicke, L., Steinbrecher, R., Tuovinen, J.-P., Vesala, T., Wohlfahrt, G., and Franz, D. (2018). Icos eddy covariance flux-station site setup: a review. *International Agrophysics*, 32(4):471–494.

Saiki, E. M., Moeng, C.-H., and Sullivan, P. P. (2000). Large-eddy simulation of the stably stratified planetary boundary layer. *Bound.-Lay. Meteorol.*, 95:1–30.

Segal, M. and Arritt, R. W. (1992). Nonclassical mesoscale circulations caused by surface sensible heat-flux gradients. *Bulletin of the American Meteorological Society*, 73(10):1593–1604.

Smagorinsky, J. (1963). General circulation experiments with the primitive equations: I. the basic experiment*. *Monthly Weather Review*, 91(3):99–164.

Steinfeld, G., Letzel, M. O., Raasch, S., Kanda, M., and Inagaki, A. (2007). Spatial representativeness of single tower measurements and the imbalance problem with eddy-covariance fluxes: results of a large-eddy simulation study. *Boundary-Layer Meteorology*, 123(1):77–98.

Stoy, P. C., Mauder, M., Foken, T., Marcolla, B., Boegh, E., Ibrom, A., Arain, M. A., Arneth, A., Aurela, M., Bernhofer, C., Cescatti, A., Dellwik, E., Duce, P., Gianelle, D., van Gorsel, E., Kiely, G., Knohl, A., Margolis, H., McCaughey, H., Merbold, L., Montagnani, L., Papale, D., Reichstein, M., Saunders, M., Serrano-Ortiz, P., Sottocornola, M., Spano, D., Vaccari, F., and Varlagin, A. (2013). A data-driven analysis of energy balance closure across fluxnet research sites: The role of landscape scale heterogeneity. *Agricultural and Forest Meteorology*, 171–172:137–152.

Stull, R. (1988). *An Introduction to Boundary Layer Meteorology*. Springer Netherlands.

Sullivan, P. P., McWilliams, J. C., and Moeng, C.-H. (1996). A grid nesting method for large-eddy simulation of planetary boundary layer flows. *Bound-Layer Meteorol*, 80:167–202.

Taylor, G. I. (1938). The spectrum of turbulence. *Proceedings of the Royal Society of London. Series A - Mathematical and Physical Sciences*, 164(919):476–490.

Weller, H. G., Tabor, G., Jasak, H., and Fureby, C. (1998). A tensorial approach to computational continuum mechanics using object-oriented techniques. *Computers in Physics*, 12(6):620–631.

Wicker, L. J. and Skamarock, W. C. (2002). Time-splitting methods for elastic models using forward time schemes. *Mon. Wea. Rev.*, 130:2008–2097.

Wieser, A., Fiedler, F., and Corsmeier, U. (2001). The influence of the sensor design on wind measurements with sonic anemometer systems. *Journal of Atmospheric and Oceanic Technology*, 18(10):1585–1608.

Williamson, J. H. (1980). Low-storage runge-kutta schemes. *J. Comput. Phys.*, 35:48–56.

Wilson, K., Goldstein, A., Falge, E., Aubinet, M., Baldocchi, D., Berbigier, P., Bernhofer, C., Ceulemans, R., Dolman, H., Field, C., Grelle, A., Ibrom, A., Law, B., Kowalski, A., Meyers, T., Moncrieff, J., Monson, R., Oechel, W., Tenhunen, J., Valentini, R., and Verma, S. (2002). Energy balance closure at fluxnet sites. *Agricultural and Forest Meteorology*, 113(1–4):223–243.

Yu, G.-R., Wen, X.-F., Sun, X.-M., Tanner, B. D., Lee, X., and Chen, J.-Y. (2006). Overview of chinaflux and evaluation of its eddy covariance measurement. *Agricultural and Forest Meteorology*, 137(3–4):125–137.

Zacharias, S., Bogena, H., Samaniego, L., Mauder, M., Fuß, R., Pütz, T., Frenzel, M., Schwank, M., Baessler, C., Butterbach-Bahl, K., Bens, O., Borg, E., Brauer, A., Dietrich, P., Hajnsek, I., Helle, G., Kiese, R., Kunstmann, H., Klotz, S., Munch, J. C., Papen, H., Priesack, E., Schmid, H. P., Steinbrecher, R., Rosenbaum, U., Teutsch, G., and Vereecken, H. (2011). A network of terrestrial environmental observatories in germany. *Vadose Zone Journal*, 10(3):955–973.

A. Contributions to collaborative publications

This thesis presented in the cumulative form consists of three first-author publications. The contribution of the first author and the co-authors to each publication is specified in this section.

Appendix B

Huq, S., Roo, F. D., Foken, T., & Mauder, M. (2017). Evaluation of probe-induced flow distortion of campbell CSAT3 sonic anemometers by numerical simulation. Boundary-Layer Meteorology, 165 (1), 9–28. https://doi.org/10.1007/s10546-017-0264-z

I designed the original experiment alongside Matthias Mauder and Frederik De Roo with suggestions from Thomas Foken. I conducted the mesh generation, simulations, data processing, and visualisation. I wrote the original draft supervised by Matthias Mauder. Frederik De Roo contributed to the manuscript preparation and Thomas Foken reviewed the manuscript. Funding acquisition and administration was by Matthias Mauder.

Appendix C

Huq, S., Roo, F. D., Raasch, S., & Mauder, M. (2019). Vertically nested LES for high-resolution simulation of the surface layer in PALM (version 5.0). Geoscientific Model Development, 12 (6), 2523–2538. https://doi.org/10.5194/gmd-12-2523-2019

I was the main developer of the model code, with Frederik De Roo as side developer, Siegfried Raasch supporting the code development, and Matthias Mauder, Siegfried Raasch and Frederik De Roo supervising the development. I designed the experiment with Frederik De Roo, Siegfried Raasch, and Matthias Mauder. I conducted the experiment and performed the validation. I did the visualisation and wrote the original draft, with contribution from Frederik De Roo, and review and editing by Siegfried Raasch and Matthias Mauder. Funding acquisition and administration was by Matthias Mauder.

Appendix D

Huq, S., De Roo, F., Sühring, M., Wanner, L., & Mauder, M. (2023). High-resolution ensemble LES energy balance closure study of the LITFASS-2003 campaign. Meteorologische Zeitschrift (under review)

I designed the experiment with Matthias Mauder and Frederik De Roo. Matthias Sühring provided field measurement data for the simulated domain and user routine to read the files. I further developed the user routine for data capturing alongside Frederik De Roo. I wrote the proposal for computing time at Leibniz Supercomputing Center which was reviewed by Frederik De Roo. I conducted the simulation and data processing. Luise Wanner contributed to the discussion on the flux calculation approach. I wrote the original draft of the manuscript supervised by Matthias Mauder. Frederik De Roo and Matthias Sühring critically reviewed the manuscript. Funding acquisition and administration was by Matthias Mauder.

B. Evaluation of probe-induced flow distortion of campbell CSAT3 sonic anemometers by numerical simulation

Huq, S., Roo, F. D., Foken, T., & Mauder, M. (2017). Evaluation of probe-induced flow distortion of campbell CSAT3 sonic anemometers by numerical simulation. Boundary-Layer Meteorology, 165 (1), 9–28. https://doi.org/10.1007/s10546-017-0264-z

Boundary-Layer Meteorol
DOI 10.1007/s10546-017-0264-z

RESEARCH ARTICLE

Evaluation of Probe-Induced Flow Distortion of Campbell CSAT3 Sonic Anemometers by Numerical Simulation

Sadiq Huq[1] · **Frederik De Roo**[1] · **Thomas Foken**[2] · **Matthias Mauder**[1]

Received: 18 November 2016 / Accepted: 16 May 2017

Abstract The Campbell CSAT3 sonic anemometer is one of the most popular instruments for turbulence measurements in basic micrometeorological research and ecological applications. While measurement uncertainty has been characterized by field experiments and wind-tunnel studies in the past, there are conflicting estimates, which motivated us to conduct a numerical experiment using large-eddy simulation to evaluate the probe-induced flow distortion of the CSAT3 anemometer under controlled conditions, and with exact knowledge of the undisturbed flow. As opposed to wind-tunnel studies, we imposed oscillations in both the vertical and horizontal velocity components at the distinct frequencies and amplitudes found in typical turbulence spectra in the surface layer. The resulting flow-distortion errors for the standard deviations of the vertical velocity component range from 3 to 7%, and from 1 to 3% for the horizontal velocity component, depending on the azimuth angle. The magnitude of these errors is almost independent of the frequency of wind speed fluctuations, provided the amplitude is typical for surface-layer turbulence. A comparison of the corrections for transducer shadowing proposed by both Kaimal et al. (Proc Dyn Flow Conf, 551–565, 1978) and Horst et al. (Boundary-Layer Meteorol 155:371–395, 2015) show that both methods compensate for a larger part of the observed error, but do not sufficiently account for the azimuth dependency. Further numerical simulations could be conducted in the future to characterize the flow distortion induced by other existing types of sonic anemometers for the purposes of optimizing their geometry.

Keywords CSAT3 · Flow distortion · Large-eddy simulation · Sonic anemometer · Transducer-shadow effect

Matthias Mauder
matthias.mauder@kit.edu

1 Institute of Meteorology and Climate Research – Atmospheric Environmental Research, Karlsruhe Institute of Technology, Garmisch-Partenkirchen, Germany

2 Bayreuth Center of Ecology and Environmental Research, University of Bayreuth, Bayreuth, Germany

Published online: 14 June 2017

1 Introduction

The eddy-covariance method has been well established to measure the energy and matter exchange between the surface and the atmosphere. Sonic anemometers are at the core of those micrometeorological measurement systems, whose accuracy is, therefore, crucial for any research on biosphere-atmosphere interactions. Fluxes of energy, water, and CO_2 are currently measured at several hundred long-term FLUXNET sites around the world (Baldocchi 2014) for which the CSAT3 anemometer (Campbell Scientific Inc., Logan, Utah, USA) is one of the most popular instruments within this network. The CSAT3 anemometer has been commercially available for more than 20 years, and has become the standard instrument of several national networks, e.g., ChinaFLUX (Yu et al. 2006), TERENO (Zacharias et al. 2011) and NEON (SanClements et al. 2014).

The accuracy of commonly used sonic anemometers is nevertheless still discussed, because a reference calibration is not readily available. Transducer-shadow effects or more general probe-induced flow distortion are suspected to be larger than what was previously thought (Kochendorfer et al. 2012), where non-orthogonal sonic arrays are found to be particularly prone to flow distortion (Frank et al. 2013). However, the magnitude of the error found for the CSAT3 anemometer differs considerably between different studies, with reports ranging from 3% to 14% for the vertical component of velocity fluctuations (Kochendorfer et al. 2012; Mauder 2013; Frank et al. 2013; Horst et al. 2015). As this situation is unsatisfactory, we wish to revisit older theoretical analyses to shed more light on this issue.

Wyngaard (1981) developed the first theory on probe-induced flow-distortion effects in which linear effects dominate, with second-order effects neglected. The theory was validated by wind-tunnel experiments, which showed that transducer-shadow effects are directly proportional to the ratio of the transducer diameter d to the sonic path length L (Kaimal 1978; Wyngaard and Zhang 1985), indicating that for $d/L < 0.05$, the resulting attenuation $<10\%$. The increased theoretical understanding led to the development of improved instruments that minimize flow distortion. For example, the transducer diameter d is to be as small as possible, with its shape aerodynamically optimized (Hanafusa et al. 1982), the sensor should be as vertically symmetrical as possible (Wyngaard 1988), and the support structure should be minimized (Dyer 1981; Kaimal et al. 1990). Wyngaard (1981) also pointed out that great care should be taken to avoid cross talk between the three velocity components because a potential-flow correction during post-processing is not possible. Kaimal (2013) gives a chronological account of the conception of sonic anemometry and the development of non-orthogonal anemometers.

These considerations led to the design of an optimized sonic-anemometer array, the so-called UW probe developed at the University of Washington (Zhang et al. 1986), which has three non-orthogonal intersecting acoustic paths tilted 60° from the horizontal plane, while supported only from behind. The 60° angle was chosen because it facilitates a more accurate determination of the vertical velocity component than does a 45° angle. This novel geometry became a model for the CSAT3-anemometer design, resulting in less flow distortion for than for previously available sonic anemometers, while being particularly optimized for the measurement of vertical fluxes (Foken and Oncley 1995).

Two possibilities to evaluate the error of sonic anemometers have included wind-tunnel studies (e.g. Kaimal and Gaynor 1983; Christen et al. 2001; Wieser et al. 2001), and side-by-side field intercomparison experiments (e.g. Dyer et al. 1982; Mauder et al. 2007; Tsvang et al. 1985), both of which have advantages, but also weaknesses. While wind-tunnel tests are conducted with steady flow under quasi-laminar conditions, the instruments are typically

deployed in the atmospheric boundary layer, where they experience a wide spectrum of turbulent fluctuations. As flow distortion depends on the turbulence intensity (Wyngaard 1981), wind-tunnel-based flow-distortion corrections tend to overestimate the true magnitude of flow distortion (Högström and Smedman 2004).

Field intercomparisons are conducted under real-world conditions. Sonic anemometers have been available for about 50 years, and it was the initial interest of the pioneers of this technique to compare the instruments under natural conditions within the so-called international turbulence comparison experiments (Miyake et al. 1971; Tsvang et al. 1973; Dyer et al. 1982; Tsvang et al. 1985), where the optimal anemometer design was the focus of research. Because of influences of the sensor and nearby devices on the degree of flow distortion (Dyer 1981), it was decided that the instruments should be installed perpendicular to the mean flow at a suitable distance from each other to help minimize this problem. Experimental sites at Tsimlyansk (Russia, 1970 and 1981) and Conargo (Australia, 1976) were considered to be ideal for such studies due to their horizontal homogeneity. The basic assumption for such comparisons was a homogeneous measuring field to ensure nearly identical turbulent characteristics for all instruments. Unfortunately, the anemometers compared then are no longer actively used. Hence, a comparison experiment following these assumptions with most of the available sonic anemometers was realized in California in the summer of 2000 (Mauder et al. 2007). Another possibility is the comparison of differently oriented sonic-anemometer arrays to detect flow distortion (Kaimal et al. 1990; Horst et al. 2015). Traditionally, only turbulence statistics are compared between different instruments, because sensors do not sample the same realization of the turbulence field due to the separation between sensors necessary to avoid cross-contamination. Recently, different sonic anemometers were placed within one integral length scale, i.e. with a separation of less than 2 m (Kochendorfer et al. 2012), to compare even instantaneous turbulence.

In any event, field intercomparisons always have the difficulty of defining an absolute reference or etalon, since it is only possible to compare one instrument with another. Nevertheless, good agreement in different statistics measured by two instruments independently over the same surface increases the confidence in the measurements. Such experiments are, therefore, very useful in characterizing the precision of sonic measurements. For example, if sonic anemometers are to be deployed at different sites at a later date, it is important to know at what scale differences are able to be detected. However, even with good agreement between two instruments, both could potentially be equally inaccurate (Horst et al. 2015).

A third possibility will be explored here, which returns to the idea of an etalon having well-known characteristics, while being stable for long time periods. For past field intercomparison experiments, the etalon was realized by using the same instrument in different comparison experiments (Mauder et al. 2007; Goodrich et al. 2016). In the following, the characteristics of a sonic anemometer are determined numerically by large-eddy simulation (LES), where a series of numerical simulations of the flow around a sonic anemometer with oscillating winds will be conducted. Within this model set-up, the undisturbed wind velocities can also be determined. The results aim to answer the following questions:

- How large are the measurement errors that arise from probe-induced flow distortion?
- Are the measurements of the vertical velocity component w and horizontal velocity component u equally affected by flow distortion?
- To what extent does the flow distortion error differ with varying azimuth and angle-of-attack?
- How does the frequency of wind-speed fluctuations affect the flow-distortion error?

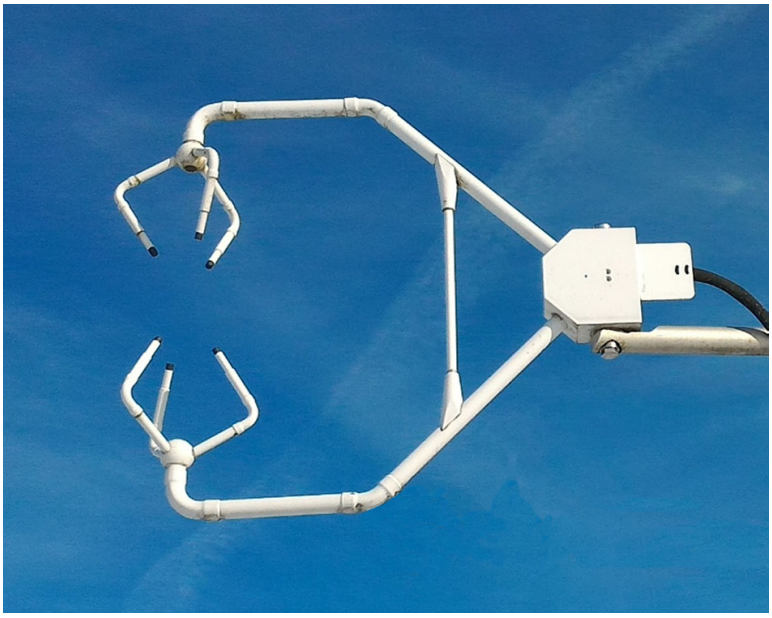

Fig. 1 A CSAT3 sonic anemometer

We consider such a numerical experiment as an important step towards a true comparability between different anemometers, and thus complementing the findings from experiments in the real world. For this study, the CSAT3 sonic anemometer (Campbell Scientific Inc., Logan, Utah) was selected, because the construction details and all software calculations in the firmware were readily provided upon request by the manufacturer. Figure 1 shows a CSAT3 sonic anemometer deployed at a field site. However, the same analysis can be conducted for any other sonic-anemometer model in principle. As a first step, the flow-distortion issue is addressed for fixed mean wind speeds and fixed frequencies for the horizontal and vertical wind components. Here, the focus is on the frequency dependence of the flow distortion. In a planned second study, the simulation will be extended to natural turbulence spectra.

2 Methods

2.1 LES in OpenFOAM®

OpenFOAM® is an open source C++ library for solving the partial differential equations commonly encountered in continuum mechanics (Weller et al. 1998). The LES models in OpenFOAM® have also been employed to simulate atmospheric boundary-layer flows (Schlegel et al. 2012). The OpenFOAM® version 2.3 is used here to solve the governing equations on a co-located unstructured mesh by the finite-volume method. An algebraic Smagorinsky model is employed to model the subgrid-scale fluxes (Fureby et al. 1997). The discretized equations are integrated in time by an implicit second-order backward scheme. As the fluid is assumed to be incompressible, the PISO (Pressure Implicit with Splitting of Operator) algorithm is used for handling the velocity-pressure coupling (Issa 1985).

For each case, the total simulated time is 70 s. The velocity field in the flow domain is initialized with a uniform value of zero, with a prescribed time-varying inlet velocity. The spin-up time of 10 s corresponds to one period of oscillation of u for the X and Y cases described below, which is sufficient for the initial wake around the anemometer to develop. The data required for computing the turbulent statistics are recorded for the next 60 s of

the simulation. The discretized equations are integrated in time in fixed steps of 2×10^{-4} s such that the maximal Courant–Friedrichs–Lewy number is always maintained below a value of 1.

2.2 Mesh Generation

The mesh generation is a critical step in the analysis that directly influences the accuracy of the simulation. While the domain size and the resolution of the mesh are the key factors, the use of a larger domain and smaller mesh spacing results in a higher computational cost. To make this investigation computationally feasible, we neglect the fact that the anemometer is usually situated within the inertial sublayer, which relaxes the need for a larger domain typically required for a fully-developed wall-bounded flow. Furthermore, not having to resolve the wall reduces the number of grid points. Consequently, the flow in vertical (z) and spanwise (y) directions is assumed to be periodic. The numerical wind tunnel is 1 m long in all three directions, and the origin of the domain is set to coincide with the intersection point of the three transducer path lengths. For cases with a 90° azimuth angle, the domain is extended by 0.2 m on one side of the spanwise direction to maintain the distance between the anemometer structure and the periodic boundary. The input signals for u and w are prescribed at the inlet for the streamwise (x) direction. A constant pressure boundary condition is applied at the outlet. The domain extent in the streamwise direction is sufficient as the magnitude of the velocity at the inflow is always positive, and an appropriate boundary condition is applied at the outlet. The domain extent in the vertical and spanwise directions is also sufficient, since the streamwise flow dominates and the periodic boundaries are placed sufficiently far away from the anemometer structure.

The smallest spatial resolution required is dictated by the diameter of the transducer pin. Since the pin is only 6.4 mm in diameter, a mesh spacing of at most 3 mm is needed in the vicinity of that surface to satisfactorily resolve the geometry. In the coarsest region, the mesh spacing is 12.5 mm, followed by the first refinement region, where the spacing is 6 mm. The finest resolution at the surface of the anemometer is between 1 mm and 2.5 mm. A constant-flux layer is assumed in the first cell adjacent to the anemometer surface. The refinement regions in the domain and the resolution around the transducer surface are shown in Fig. 2. Four different meshes were generated for different azimuth angles. Additional meshes for angle-of-attacks of 5° and 25° at a 0° azimuth angle were also generated. The unstructured mesh containing mostly hexahedral cells and some polyhedral cells is generated using a mesh generation tool in OpenFOAM® (the so-called *snappyHexMesh* utility). The meshes meet the common quality requirements for cell aspect ratio and non-orthogonality.

2.3 Simulation Set-Up

The wind velocity and the frequency for the horizontal and vertical components were selected to be close to typical values found in the field. Therefore, the model spectra by Kaimal et al. (1972) were used to find values in the inertial subrange close to the energy maximum. For an arbitrary measurement height of 2 m, the mean horizontal wind speed $\bar{u}$ was chosen as $2\,\mathrm{m\,s^{-1}}$ with a sinusoidal variation of peak amplitude $u_{\mathrm{amp}} = 1\,\mathrm{m\,s^{-1}}$ and a frequency of $u_{\mathrm{freq}} = 0.1\,\mathrm{Hz}$; the mean vertical wind speed $\bar{w}$ was set to zero with a sinusoidal variation of peak amplitude $w_{\mathrm{amp}} = 0.5\,\mathrm{m\,s^{-1}}$ and a frequency of $w_{\mathrm{freq}} = 1.0\,\mathrm{Hz}$ (case Y). The relevant positions within the turbulence spectra are shown in Fig. 3. In addition, we also conducted simulations where both u and w have the same frequency of oscillation (0.1 Hz, case X), as well as a set of simulations with a constant wind speed and no oscillations, which is similar

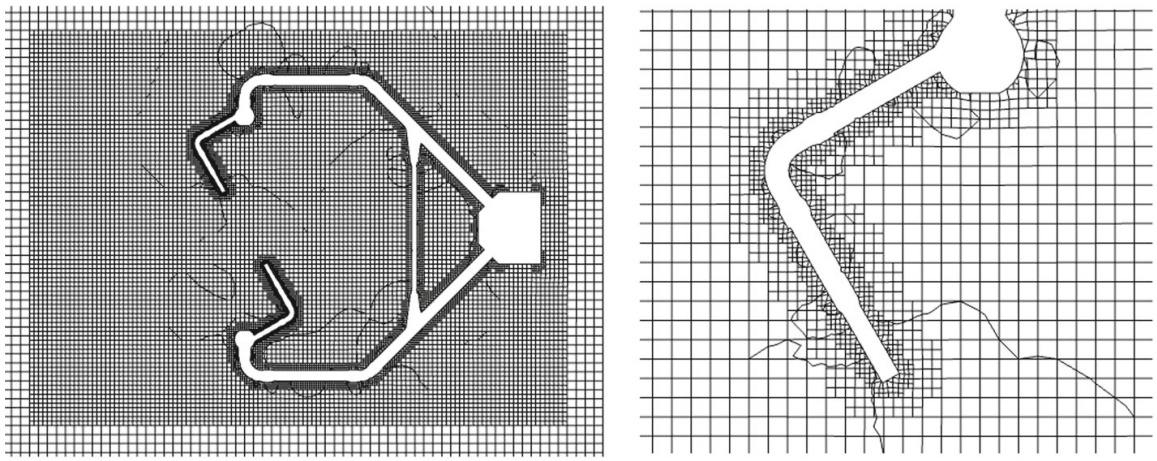

Fig. 2 Mesh cross-section at the centre of the domain for the anemometer at a zero azimuth angle. Regions of domain refinement (*left*), and the mesh near the surface of the transducer (*right*), are shown. Only two of the six transducer pins are visible in the left sub-panel. While creating a cross-section of the unstructured three-dimensional mesh, some spurious lines are formed in the resulting two-dimensional mesh, although these artefacts do not exist in the computational domain

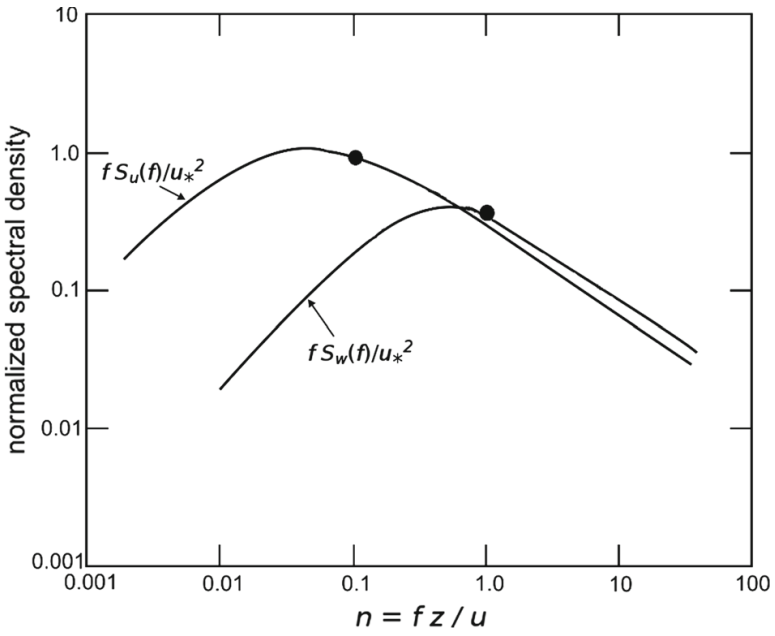

Fig. 3 Position of the chosen simulation characteristics (*black filled circle*) for the horizontal component of the velocity u and the vertical component of the velocity w in comparison with the model spectra (modified after Kaimal et al. 1972)

to wind-tunnel studies (case Z). The oscillating velocity components of case Y are shown in Fig. 4.

Simulations for all three cases X, Y and Z were conducted for four different azimuth angles (0°, 30°, 60° and 90°). For case Z, we also varied the angle-of-attack three times (0°, 5° and 25°), together with the angle-of-attack that is changing constantly due to the imposed oscillations for the X and Y cases. The input parameters for the 28 simulations are listed in Table 1. The cases are coded such that the first character indicates the sinusoidal input signal, with the following two digits signifying the azimuth angle, and the last two digits representing the angle-of-attack.

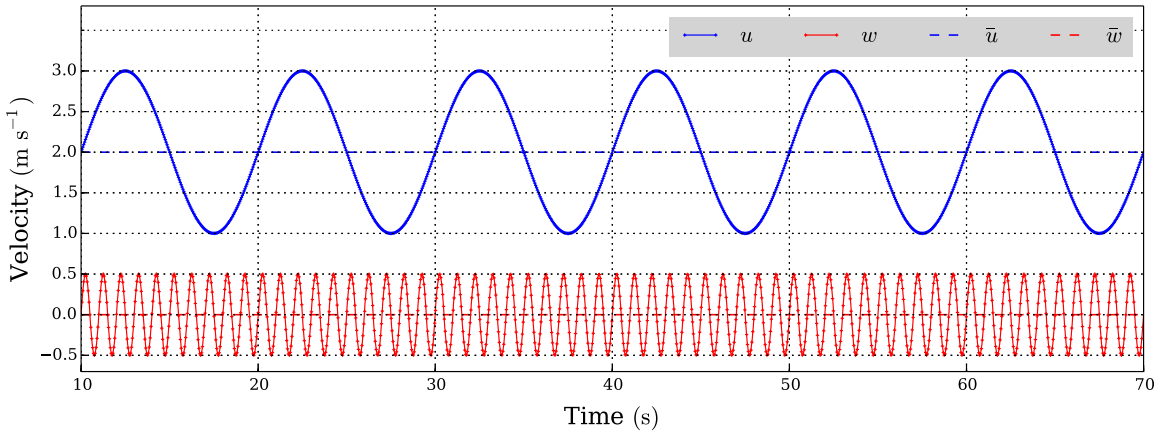

Fig. 4 Time series of u and w at the inflow along with their mean for case Y

Table 1 Overview of all simulation parameters describing the azimuth angle and the mean angle-of-attack realized by variations of the oscillating inflow signal (X- and Y-cases and Z0000) and by rotating the anemometer in the model domain (all other Z-cases)

Case	Azimuth angle (°)	Angle-of-attack (°)	Sine inflow signal
X0000	0	0	$\bar{u} = 2\,\mathrm{ms}^{-1}$
X3000	30	0	$\bar{w} = 0$
X6000	60	0	$u_{\mathrm{freq}} = 0.1\,\mathrm{Hz}$
X9000	90	0	$u_{\mathrm{amp}} = 1\,\mathrm{ms}^{-1}$
			$w_{\mathrm{freq}} = 0.1\,\mathrm{Hz}$
			$w_{\mathrm{amp}} = 0.5\,\mathrm{ms}^{-1}$
Y0000	0	0	$\bar{u} = 2\,\mathrm{ms}^{-1}$
Y3000	30	0	$\bar{w} = 0$
Y6000	60	0	$u_{\mathrm{freq}} = 0.1\,\mathrm{Hz}$
Y9000	90	0	$u_{\mathrm{amp}} = 1\,\mathrm{ms}^{-1}$
			$w_{\mathrm{freq}} = 1.0\,\mathrm{Hz}$
			$w_{\mathrm{amp}} = 0.5\,\mathrm{ms}^{-1}$
Z0000	0	0	$\bar{u} = 2\,\mathrm{ms}^{-1}$
Z0005	0	5	$\bar{w} = 0$
Z0025	0	25	$u_{\mathrm{amp}} = 0$
Z3000	30	0	$w_{\mathrm{amp}} = 0$
Z3005	30	5	
Z3025	30	25	
Z6000	60	0	
Z6005	60	5	
Z6025	60	25	
Z9000	90	0	
Z9005	90	5	
Z9025	90	25	

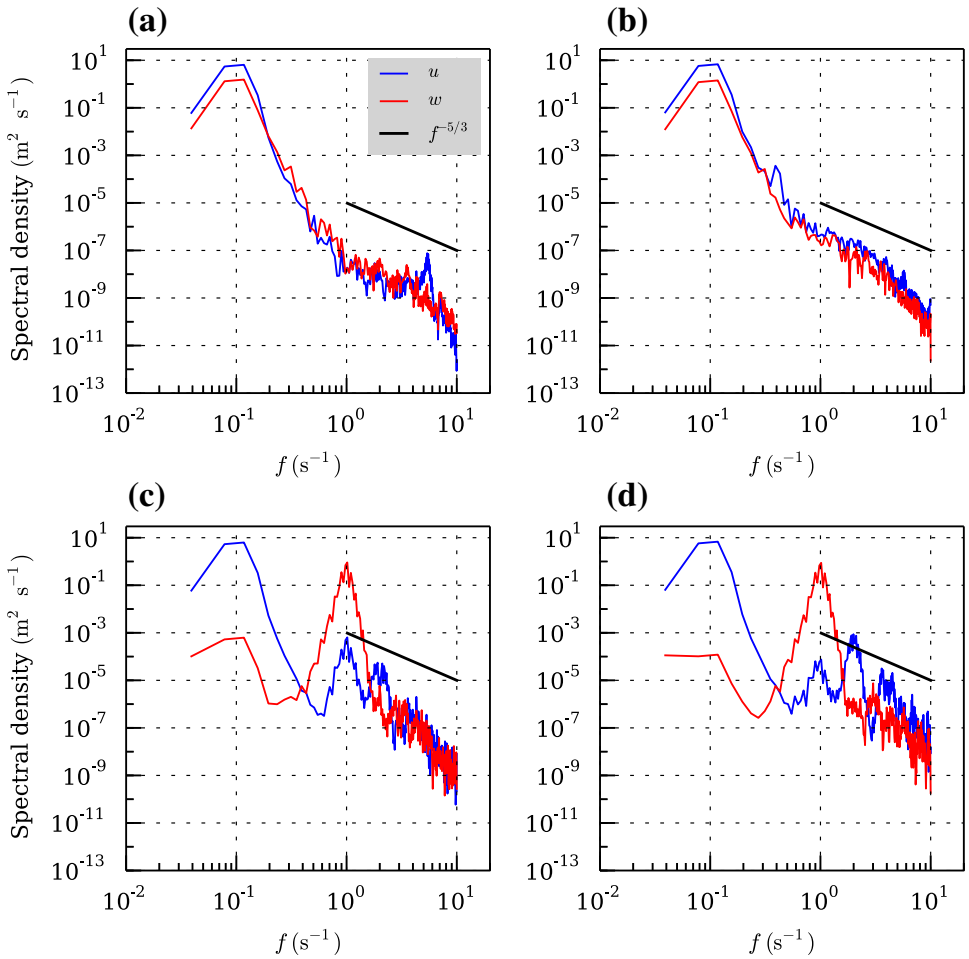

Fig. 5 Spectral density of the u and w velocity components for cases: **a** X0000, **b** X9000, **c** Y0000, and **d** Y9000

The spectra derived from the virtual sonic anemometer measurements are shown in Fig. 5. The peaks of the respective input signals at 0.1 and 1 Hz can clearly be identified. However, it is interesting to note that part of the turbulent kinetic energy has already been transferred to smaller eddies along the turbulence cascade, even though the distance from the left boundary of the simulation domain is only 0.5 m. This is indicated by an inertial subrange starting at frequencies of about 0.5 Hz for the X cases (Fig. 5a, b) and at about 2 Hz for the Y cases (Fig. 5c, d). For the Y cases, harmonics in the turbulence cascade region of the horizontal component can also be observed. One can also see that there are some minor differences in the spectra depending on the azimuth angle, which is 0° for the two left subpanels (Fig. 5a, c) and 90° for the two right subpanels (Fig. 5b, d).

In fact, when rotating the set of three transducer pins 60° in the xy-plane, and turning the anemometer upside down ($z \rightarrow -z$), the latter effectively exchanging the orientation of the upper three pins for that of the lower three pins, the configuration of the transducer is identical to the orientation before rotation. Therefore, we expect the response of the flow to behave similarly for azimuth angles that differ by 60°, at least if the inflow does not change under the operation $z \rightarrow -z$. For the Y cases, the input velocity has no preferred directionality along the z-axis, because the w-frequency is 10 times higher than the u-frequency and the inflow u and w signals are effectively decoupled. Note that the locus of the input velocity shown in Fig. 6b remains unchanged when the sign of w is reversed. For the X cases, however, w and u have the same frequency and vary in phase, which means that a positive w is correlated with higher wind speeds, and negative w with lower wind speeds. Therefore, the locus of

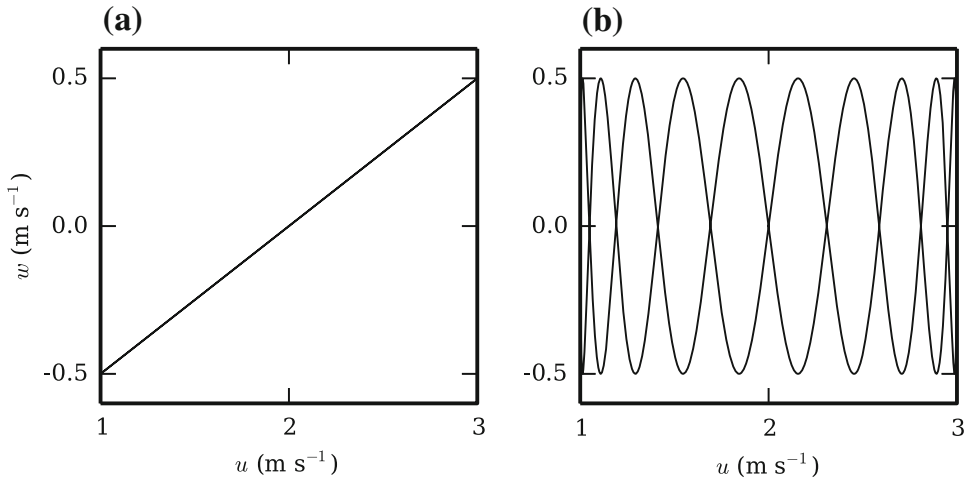

Fig. 6 Locus of input flow speed l m s^{-1} for case X (**a**) and case Y (**b**)

the input velocity for the X cases becomes different when the sign of w is reversed under the operation $z \rightarrow -z$. Hence, we cannot expect the results for φ and $\varphi + 60°$ to behave similarly for the X cases.

2.4 Virtual Measurement

The flow distortion by the sonic anemometer is studied by analyzing the velocity fluctuations recorded by a virtual probe inside the simulation domain. The vertical distance between the tips of the lower and upper transducers is 0.1 m. The distance between a matching pair of transducers, i.e. the path length, is 0.12 m. For each pair of transducers, velocity measurements are collected at 11 points along the acoustic path over a length of 0.115 m. In the first cell adjacent to the surface of the anemometer the turbulence is parameterized in an LES, due to the lack of resolved turbulence in this region of the flow, the data collected there are unreliable. The virtual path length is accordingly shortened by 2.5 mm on either side. The 33 values from the three virtual paths are averaged to arrive at a single instantaneous value for u, v and w. The virtual probe collects data at 100 Hz, which is then re-sampled by block averaging to 20 Hz during post-processing, corresponding to the typical frequency for recording field measurements.

The reference measurement for the velocity (i.e. the measurement of the undisturbed flow) is assessed by three different methods. The first is by replicating the virtual probe, but offset by 0.3 m from the anemometer in the spanwise direction (AddProb). The data are presumed to be reliable there since the grid spacing in the reference region is approximately the same as in the transducer path length. One alternative method is to perform separate reference simulations on a structured grid without the anemometer being present in the domain (RefSim). Another alternative method is to directly take the input signal as the reference with which to compare the virtual measurements (InFlow). The influence of the different measurement concepts was tested (see Sect. 4.2) and the InFlow reference was found to be the most appropriate here.

3 Results

3.1 Qualitative Analysis

The wake behind the transducers and the supporting structure in the top part of the anemometer is illustrated in Fig. 7, where for a dominant streamwise velocity component, the wakes of the

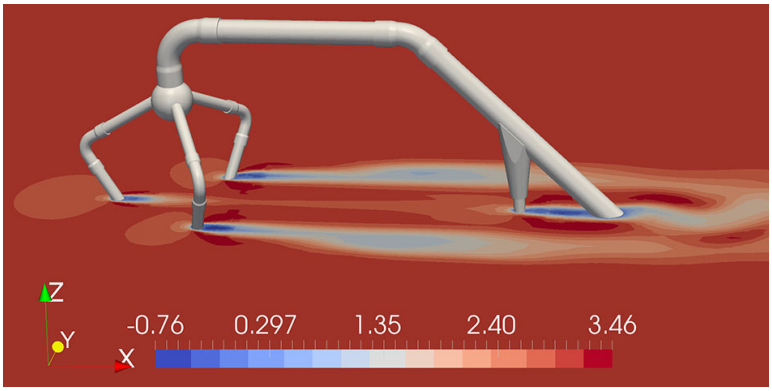

Fig. 7 An illustration of the wake behind the transducers by means of a cross-section of the instantaneous u-velocity component in m s^{-1} at an arbitrary z-level for the case Y0000 at time = 63 s. The anemometer geometry is superimposed for clarity

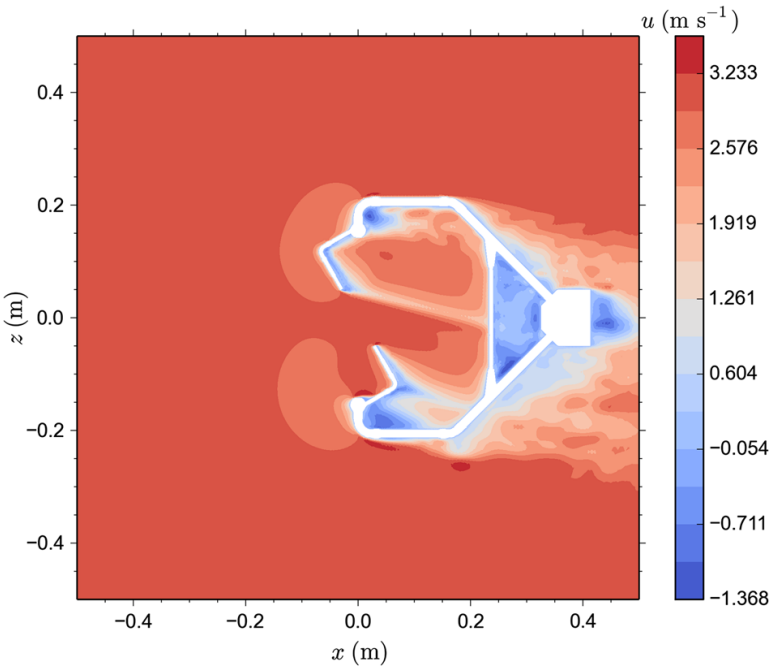

Fig. 8 Instantaneous u-velocity component at the cross-section in the middle of the domain for the case Y0000, time = 63 s, as in Fig. 7; the wind velocity components are $u = 2.95\,\mathrm{m\,s^{-1}}$ and $w = 0$. Only two of the six transducer pins are visible. A stagnation area in front of the transducers and a recirculation area to the rear side are observed. The wake behind the anemometer is inclined downwards as a result of negative values of w prescribed in the earlier timesteps

transducers and the supporting structure do not interact. The pulsating velocity of the inflow means that the flow strikes the anemometer at a different angle-of-attack at each timestep, as under naturally turbulent conditions. In Fig. 8, the wake behind the anemometer is tilted downwards due to the non-zero angle-of-attack of the flow, where a recirculation region immediately behind the transducer is also seen. Just above the bottom transducer pin, there is a region of increased flow speed, which will affect the anemometer measurements. Although the instantaneous w-velocity component in the measurement volume of the sonic anemometer is exactly zero in Fig. 8, the wake downwind of the instrument moves below the instrument, because this area of the simulation domain is still influenced by the negative w values applied earlier as the input signal. The downwind wake, which is clearly resolved by our LES, can be considered as being fully turbulent. The second largest structural elements, i.e. the supporting

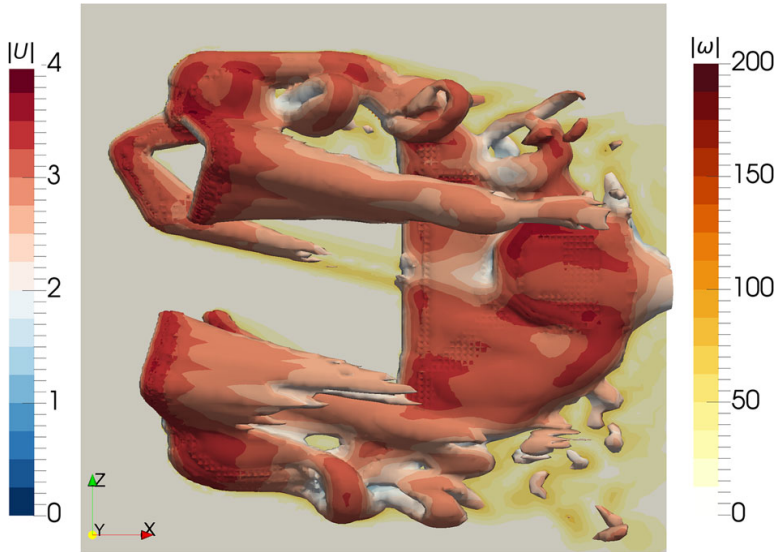

Fig. 9 Isosurface (at 66 Hz) of the magnitude of instantaneous vorticity coloured by the velocity magnitude $|U|$ in m s^{-1} (*blue to red*). The background image shows the vorticity magnitude $|\omega|$ in Hz (*white to red*, but only the *yellow part* is visible outside of the isosurface). This figure shows the case Y0000 at time = 63 s, as in Fig. 7. Only one measurement path is fully visible (*upper-left* transducer to *lower-right* transducer); the other two visible transducers are both frontal parts belonging to two different measurement paths. The corresponding transducers at the back are not visible at this viewing angle. The structure of the vortices is discussed in Sect. 4.1

arm along with the spherical joint that connects the three transducers at the top and bottom respectively, cause vortex shedding. However, the wakes generated by the transducer pins, which are much smaller in diameter than the rest of the anemometer structure, appear to be at least partly of a laminar character far downwind, because no fluctuations are visible there. However, the wake region immediately near the pins is certainly turbulent. These observations are confirmed by the vorticity plot in Fig. 9, where the swirls are distorted to some extent by the oscillating input signal. It is noteworthy that the flow in the actual measurement volume appears to be largely undisturbed, with flow distortion only visible in those grid cells of the measurement path that are very close to the transducer pin.

3.2 Quantitative Analysis

As expected, the mean vertical velocity component is measured accurately for almost all simulated cases, as depicted in Fig. 10. Furthermore, the mean u-component agrees well with the input signal for all the X and Y cases, and those Z cases with zero angle-of-attack. Unexpectedly, the error of the mean u-component is larger for constant flow speeds with a 5° angle-of-attack than with a 25° angle-of-attack.

For flux measurements, the accuracy of the mean velocities is almost irrelevant because the average is always subtracted when calculating a covariance. Only turbulent fluctuations must be captured accurately as is evident from the analysis of the standard deviations of the velocity components (Fig. 11). In our simulations, the relative error of the u-component is generally less than 4% and less than 7% for the w-component, but varying with the azimuth angle. While part of the difference between the relative errors of u and w arises from their different normalizations, because the standard deviation of u is larger than that of w, the absolute error of the standard deviation of w is also larger than that of u (not shown). The smallest errors of the w-component, which is critical for measurements of vertical fluxes,

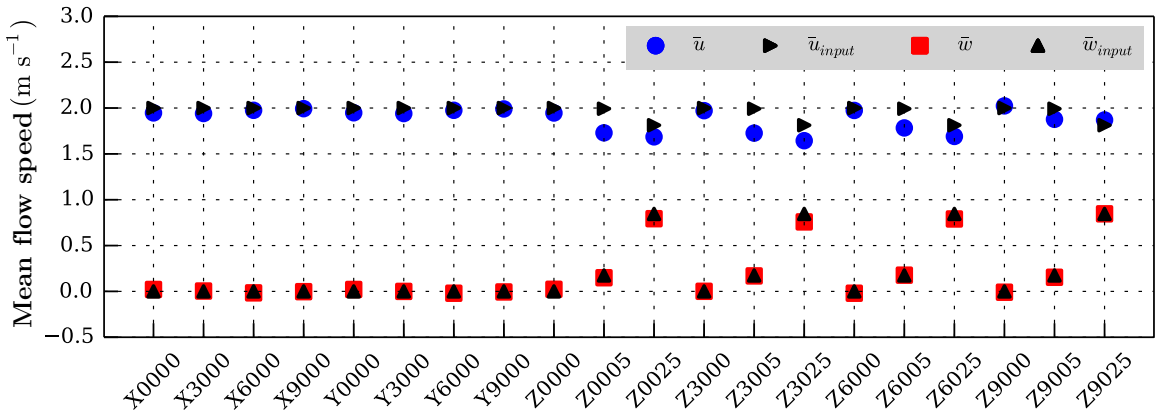

Fig. 10 Mean flow speed measured by the virtual sonic anemometer for the u-component ($\bar{u}$) and for the w-component ($\bar{w}$). The *triangles* indicate the corresponding component of the input signal for reference. The x-axis shows the different simulated cases listed in Table 1

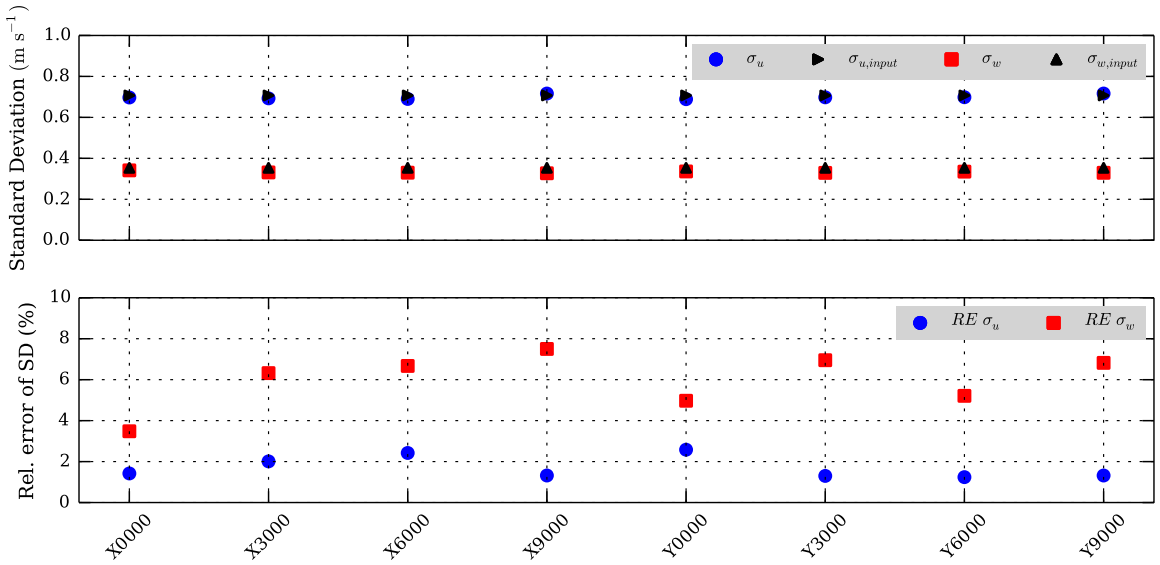

Fig. 11 In the *top subpanel*, the virtual CSAT3-measurements of velocity fluctuations are compared with the input signal for reference by plotting the standard deviations of u (σ_u) and w (σ_w). In the *bottom subpanel*, the relative error of the virtual standard deviation measurements ($RE\sigma_u$ and $RE\sigma_w$) is shown. Labels X and Y denote cases with a different frequency of oscillation; the trailing digits in the label indicate the azimuth angle of the anemometer

occurs for azimuth angles of 0°, becoming only 3% for the X case with w-oscillations of 0.1 Hz, and 5% for the Y case with 1-Hz oscillations.

4 Discussion

We align our discussion of the results along the concepts of internal and external validity (Campbell and Stanley 1963), which were originally proposed for experiments in the area of social sciences, but may also be useful here to emphasize the significance of the numerical experiment. If an experiment is not internally valid, we cannot say that the observed results have a causal relationship with the input parameters. If an experiment is not externally valid, results cannot be said to hold outside of the experimental setting, and thus, even if internally valid, they are still irrelevant outside the experiment (Jiménez-Buedo and Miller 2010). The relationship between internal and external validity is often described as a trade-off in

which laboratory experiments typically have the highest internal validity, but lowest external validity, and pure observational data collected in the field have the lowest internal validity, but highest external validity (Roe and Just 2009).

4.1 Internal Validity of the Wake Regions

We investigate, firstly, the degree to which the wake regions have been resolved. The anemometer consists of different structural components, each of which leads to the generation of a wake. As seen in Fig. 8, the wake of the transducer pin has a different appearance compared with the wake of the support arm and the wake of the central structure on the right. To discuss the wake behind an immersed structure, we need to first introduce the Reynolds numbers (Re) related to the individual components, while restricting our analysis to one transducer pin, the support arm on the top, and the central structure on the right side, with diameters (D) of 6.4, 15.9 and 100 mm, respectively. With a kinematic viscosity of $\nu = 1.5 \times 10^{-5}\,\mathrm{m^2\,s^{-1}}$ and the mean wind speed of $\bar{u} = 2\,\mathrm{m\,s^{-1}}$, the Reynolds numbers are 850, 2100 and 13,333, respectively, where $Re = \bar{u}D/\nu$. The latter value is above the critical Reynolds number for turbulent flow. Following Williamson (1996), for the two larger values ($Re > 1000$), the turbulent wake region behind the cylinder consists of von Kármán vortices interspersed with many other turbulent elements. For the transducer pin, we, therefore, expect a regular von Kármán vortex street. Hence, the pulsating flow in the x-direction may lead to vortex shedding, depending on the orientation of the structural element. However, we have to take into account that the central structure on the right is not entirely cylindrically shaped, and the support arm is actually aligned with the mean flow direction in the case of a zero mean angle-of-attack. From the oscillating flow in the z-direction, we expect no vortex shedding because of the zero mean vertical velocity.

In addition, the pulsating inflow leads to the further complication that, in theory, the vortex street interacts with the harmonic perturbation on the mean inflow. For oscillating cylinders in steady flow, Karniadakis and Triantafyllou (1989) found that the interaction between the vortex street and the oscillation depends on the ratio of the oscillation frequency to the vortex-shedding frequency (f_s), and the ratio between the amplitude of the oscillation and the diameter of the cylinder. The oscillation frequency at the inflow is 1 Hz at most here, where the frequency of vortex shedding is estimated from the Strouhal number, $St = Df_s/\bar{u}$, which is approximately 0.2 for $Re < 10^4$ (Sakamoto and Haniu 1990), leading to $f_s = 50\,\mathrm{Hz}$ for the anemometer pins. Therefore, the ratio of the frequencies here is 1/50. To determine the ratio of the length scales, we adapt the case of the oscillating cylinder to our case of a pulsating inflow. Changing the frame of reference, the amplitude of the oscillating cylinder is obtained from the amplitude of the velocity fluctuation ($1\,\mathrm{m\,s^{-1}}$) divided by the angular frequency (6 Hz) of the pulsating inflow, yielding the ratio of the length scales of about 0.15/0.01. As both the frequency and length-scale ratios are significantly different from unity, there cannot be a significant alteration of the wake by the low-frequency unsteady inflow.

By taking a closer look at Fig. 9, we notice the vortices detaching from the turbulent wake at the upper arm, while we do not observe a von Kármán street in the wake of the transducer pin, which also appears smoothed in Fig. 8. Therefore, although it is possible that the mesh in front of the supporting structure is not fine enough to resolve the individual von Kármán vortices in the wake behind the transducers, the average behaviour of the wake has been adequately resolved, even though the individual turbulent elements are not. Furthermore, the wake from the transducer pins only crosses the measurement paths for large angles-of-attack. Although the drag coefficient could alter slightly when the von Kármán vortices are resolved, this cannot significantly change the conclusions of the study, especially since the

drag coefficient actually drops when a laminar boundary layer develops into a von Kármán street. Hence, for the same mean velocity, the drag will be even smaller in the case of the resolved von Kármán street due to its lower drag coefficient.

4.2 Internal Validity of the Virtual Measurements

Naturally, the internal validity of the presented virtual measurements is high, because the experiment is conducted completely under controlled conditions as it is purely numerical. Any unwanted external disturbances common to experiments in the field are excluded, with measurement errors thereby reduced to the numerical precision of the simulation. Nevertheless, the design of the virtual sonic anemometer measurement, i.e. the exact definition of the sampling points and the sampling interval, may have an influence on the resulting flow-distortion error. Moreover, while the choice of the reference measurement will influence the resulting error estimate, it is uncertain by how much.

We first consider the importance of the exact location of the virtual measurements within the acoustic paths. As described above, we have placed 11 virtual probes in each of the three sonic paths of the anemometer to mimic the actual volume-averaging sampling of the real anemometer. The space between two virtual probes is defined to be larger than the local grid resolution to avoid the same grid cell being sampled twice, resulting in the sampling of every second grid cell within the measurement paths, whereby there are more than 20 grid cells along a path of 0.115 m at a grid resolution of 0.006 m. Since the qualitative analysis showed that the flow in the measurement volume is rather homogeneous, the 11 virtual probes are sufficient because the sampling points are equidistant and the area in the direct vicinity of the transducer pin is well represented. However, if the two sampling points at the ends of each virtual measurement path were to not be taken into account appropriately, the resulting error in the measurement of the standard deviation would even have the opposite sign (data not shown). The opposite sign appears due to mass conservation as the flow slightly speeds up at the centre of the measurement volume as it circumvents the bluff body of the anemometer. Directly next to the transducer pin, the flow is reduced due to drag.

The other question concerns the best reference for calculating the measurement error, or in other words, the exact definition of the etalon, for which we tested three different possibilities:

(a) a separate reference simulation (RefSim),
(b) additional virtual probes (AddProb),
(c) the prescribed input signal (InFlow).

The difference between a, b, and c are quite small (Table 2), and each has advantages and disadvantages. The RefSim reference has the advantage that the position of the virtual measurement in the simulation domain is the same, but the mesh is inevitably slightly different, with high computational costs. The AddProb reference has advantages in that the distance from the left domain boundary is the same and no additional simulation is necessary, but it is uncertain to what extent the addition probes are really undisturbed. This is especially a problem for the 90° azimuth angle, since a larger computational domain is required to prevent the wake penetrating the periodic spanwise boundary. The InFlow reference also does not require any additional simulation; the signal is certainly undisturbed, but the turbulent cross-talk between the u and w velocity components along the 0.5-m distance between the left boundary and the anemometer position are not reflected. We chose the InFlow reference for the presentation of the results in Sect. 3, because the comparison with the RefSim results shows that the mismatch in measurement position of 0.5 m in the flow direction is not critical.

4.3 External Validity

Our LES simulation can be assumed to have a higher external validity than wind-tunnel studies, because we applied a pulsating inflow with fluctuations oriented in both frequency and amplitude at conditions typical for the inertial sublayer of the atmospheric surface layer, where flux measurements are usually conducted. To assess the external validity of our simulations further, our results are compared with other studies with the aim of characterizing the probe-induced flow distortion of the CSAT3 anemometer.

Friebel et al. (2009) show that the CSAT3 anemometer has no significant error of the mean wind speed with the exception of the wind sector of 160°–200°, which is in very good agreement with our results. Furthermore, the error of u-fluctuations is found to be about twice as large for the zero azimuth as for the other flow angles, which is also reported by, e.g., Li et al. (2013), who, as a consequence, propose a different planar fit for the wind sector corresponding to the ±30° azimuth.

From a field experiment with two horizontally-mounted RM Young 81000 sonic anemometers as reference instruments, Kochendorfer et al. (2012) determine an error estimate of 14% for the standard deviation of the w-component as measured by a tilted CSAT3 anemometer, which is much larger than both our findings, as well as that from all previous field intercomparison experiments, where the CSAT3 anemometer was even chosen as the reference on account of its minimal flow distortion (Foken and Oncley 1995; Loescher et al. 2005; Mauder et al. 2006, 2007). Therefore, we interpret this discrepancy between the error estimate of Kochendorfer et al. (2012) and our results as an indication that the experimental design of the former study was flawed, as previously pointed out by Mauder (2013).

Frank et al. (2013) compared two vertically-mounted CSAT3 anemometers with two horizontally-mounted CSAT3 anemometers to conclude that the horizontally-mounted CSAT3 is less influenced by flow distortion for measuring vertical fluxes. This is confirmed by our results also showing the relative error of the standard deviation of w being approximately twice as large as the relative error for the standard deviation of u. While we agree with this aspect of their study, it is not clear how the error of $\overline{w'T_s'}$ can be larger than the error of standard deviation of w (σ_w). While the error of $\overline{w'T_s'}$ may theoretically be smaller than that of σ_w, provided the time series of the w-component is affected by spikes uncorrelated with the time series of T_s, a larger error of the flux implies an additional error in the measurement of T_s. Indeed, Horst et al. (2015) demonstrate that flow distortion can also affect the sonic temperature measurement, which may explain these differences in σ_{Ts}. Nevertheless, the experimental design of Frank et al. (2013) has the disadvantage that the sensors are placed within the roughness sublayer over a forest, where the turbulence is heavily affected by coherent structures and the instantaneous angle-of-attack can be very large, especially as their site is also sloped. Moreover, the flow is often dominated by coherent structures during stable stratification, resulting in larger angles-of-attack than that tested here.

For the standard deviation of the w-component, Horst et al. (2015) report a relative error of between 3 and 5%, which is almost the same as our error. We suspect the error from our numerical experiment is slightly larger because the turbulence intensity is not quite as large as in the field, where more intense turbulence tends to weaken flow-distortion effects. Moreover, it is interesting that Horst et al. (2015) find the error to be independent of measurement height and stability, implying that the frequency of turbulent fluctuations does not influence measurement error, at least within the range usually found in atmospheric boundary-layer flows. Hence, Horst et al. (2015) also confirm our finding that the flow-distortion error is not systematically different between the X and Y cases, although the w-frequency differs by one order of magnitude.

Table 2 Relative errors of the virtual standard deviation measurement of the w-component in % for three different possibilities of defining the "true" velocity. In addition, the relative errors based on the InFlow reference are provided after applying the corrections of Kaimal (1978) and Horst et al. (2015)

Case	$RE\sigma_w$ (RefSim)	$RE\sigma_w$ (AddProb)	$RE\sigma_w$ (InFlow)	$RE\sigma_{w,\mathrm{Kaimal}}$	$RE\sigma_{w,\mathrm{Horst}}$
X0000	3.13	3.20	3.48	1.95	0.37
X3000	5.98	6.07	6.32	3.35	2.72
X6000	6.33	6.39	6.67	2.68	2.56
X9000	7.16	7.32	7.50	5.14	3.97
Y0000	4.93	4.62	4.97	3.13	1.44
Y3000	6.91	6.59	6.95	4.3	3.46
Y6000	5.18	4.87	5.21	1.93	1.7
Y9000	6.78	6.57	6.82	4.48	3.13

4.4 Flow-Distortion Correction

The concept of transducer-shadow effects in sonic anemometry actually goes back to the ground-breaking work of Kaimal (1978), see also Kaimal et al. (1990), where a linear dependence of the transducer-shadow effect on the ratio between the path length and transducer diameter was found (which is about 18 for the CSAT3), and

$$v_{\mathrm{m}} = \begin{cases} v\left(0.84 + \frac{0.16\theta}{75}\right); & 0^\circ \le \theta \le 75^\circ \\ v; & 75^\circ \le \theta \le 90^\circ \end{cases} \tag{1}$$

Here, v_{m} is the measured velocity component obtained from each acoustic path separately, and θ is the instantaneous angle between the velocity vector and the respective acoustic path. Furthermore, Horst et al. (2015) similarly suggested

$$v_{\mathrm{m}} = v\left(0.84 + 0.16\sin\theta\right), \tag{2}$$

which depends on the sine of the flow angle. We applied both corrections (Eqs. 1, 2) to the high-frequency data of our virtual measurements and the results are presented in Table 2. Accordingly, the error of the standard deviation of the w-component indeed becomes smaller after applying the corrections proposed in the literature. Both corrections reduce the error of σ_w by about 1–3%, while the Horst-correction is slightly larger and, therefore, closer to the reference value of our simulations. However, neither of the two corrections fully compensates for the error in σ_w.

In the fundamental literature concerning the optimal design of the sonic anemometer (Wyngaard and Zhang 1985; Zhang et al. 1986; Wyngaard 1988), the importance of minimizing flow distortion of the vertical component of the wind velocity is stressed, because the spectrum of the vertical component has its maximum typically at frequencies of about one magnitude larger than the horizontal component (Fig. 3). It is especially important to minimize artificial cross-contamination between these two wind velocity components because such an error cannot be compensated by wind-tunnel-based corrections (Wyngaard 1988). Such problems can be diagnosed by analyzing the correlation coefficient between the horizontal and vertical wind velocity components. However, this correlation coefficient for the momentum flux is in general much lower than for scalar fluxes (Kaimal and Finnigan 1994; Arya 2001), which underlines the statistical independence between the low-frequency fluctuations of the horizontal wind speed and the high-frequency fluctuations of the vertical

wind speed. Therefore, the instantaneous wind velocity changes very rapidly in time, which disagrees with the angle-of-attack concept originating from experiments with a constantly tilted instrument in a steady-state flow (van der Molen et al. 2004; Nakai et al. 2006; Nakai and Shimoyama 2012). Our results also show that angles-of-attack larger than 5° indeed lead to large flow-distortion errors for the mean wind speed, but this error becomes much smaller as soon as oscillations are superimposed on the flow. Obviously, the latter case is closer to conditions in the field. Moreover, no angle-of-attack dependent correction is found to be necessary for the measurement of fluctuations, which is in agreement with Horst et al. (2015).

Finally, in considering the different values of $RE\sigma_w$ for the different azimuth angles, the Y-cases, Y0000 and Y6000 behave similarly, as do Y3000 and Y9000, while the X cases do not show the 60° symmetry. As mentioned in the methods section, this can be expected from the symmetry of the transducer structure and the inflow signal, because the input velocity has no preferred directionality along the z-axis for the Y-cases. Hence, $RE\sigma_w$ for a Y case with azimuth angle φ is comparable with $RE\sigma_w$ for $\varphi + 60°$. Grare et al. (2016) also report a similar azimuth dependence of the flow-distortion error for the CSAT3 anemometer based on field and wind-tunnel data.

5 Conclusions

As expected, our study confirms that probe-induced flow distortion of the CSAT3 anemometer causes a dampening of both horizontal and vertical wind velocity components for all the azimuth angles and mean angles-of-attack that were tested. This overall dampening effect is caused by the drag in the first few millimetres of the measurement path in the direct vicinity of the sonic transducer, while the velocity magnitude in the centre of the measurement path is often even increased. Furthermore, our experiment confirms that probe-induced flow distortion is much smaller for unsteady wind velocities than under constant flow conditions.

Whether these fluctuations occur at frequencies of 1 or 0.1 Hz is of minor importance. Hence, the errors reported here can be considered as being spectrum-independent to some extent, for wind fluctuations of a magnitude typical for surface-layer turbulence ($\mathcal{O}(1\ \mathrm{m\ s^{-1}})$). Hence, neither stability nor measurement height influences the flow-distortion error significantly, which is in agreement with the Horst et al. (2015). Our findings also explain why wind-tunnel-based experiments with quasi-laminar flow conditions typically result in larger flow-distortion errors than field intercomparisons, and why wind-tunnel-based corrections are not transferable to turbulence measurements in the field.

We found that the CSAT3 anemometer has an improved accuracy for the measurement of fluctuations of the u-component than of the w-component, implying that the flow distortion could be reduced if the instrument were rotated by 90°, which is in agreement with the results from a field comparison of vertically- and horizontally-mounted CSAT3 anemometers (Frank et al. 2013). When mounted vertically, the probe-induced dampening effect is of 3–7% for the w-fluctuations, depending on the azimuth angle, while it is only 1–3% for the u-fluctuations. However, the regular vertical orientation probably results in a higher precision of the w-measurement.

The results for $RE\sigma_w$ are larger than the difference between different instruments of the same model found during field intercomparisons (Mauder et al. 2007). Hence, if the numerical experiment is chosen as the etalon, then a systematic error of about 5% would need to be added to the results of in situ comparisons. Reconsidering the findings of Mauder et al. (2007)

for σ_w, the agreement of the CSAT3 anemometer with some models would improve (ATI-K, R.M. Young), but become worse with others (Solent-HS, USA-1, NUW).

The transducer-shadowing correction proposed by Horst et al. (2015) reduces the magnitude of the observed probe-induced dampening effect, but it does not reflect the azimuth dependence of this error. A remaining flow-distortion error translates directly into an underestimation of scalar fluxes, such as the fluxes of sensible heat, latent heat, and CO_2, and this error will be as large as the error for σ_w, assuming that the scalar measurement does not produce any additional flow distortion due to the presence of gas analyzers.

Large-eddy simulation has been successfully applied to characterize the flow distortion of a popular sonic anemometer. Similar studies may be conducted for other sonic-anemometer models in the future. Moreover, large-eddy simulation may also be used to optimize the structural design of sonic anemometers or to develop new correction algorithms.

Acknowledgements This work was conducted within the Helmholtz Young Investigator Group "Capturing all relevant scales of biosphere-atmosphere exchange—the enigmatic energy balance closure problem", which is funded by the Helmholtz-Association through the President's Initiative and Networking Fund, and by KIT. We also gratefully acknowledge Michael Manhart (Technical University of Munich) for fruitful discussions about the simulation set-up, and we thank Campbell Scientific for providing a CAD model of the CSAT3 geometry.

References

Arya SP (2001) Introduction to micrometeorology. Academic Press, San Diego, 415 pp

Baldocchi D (2014) Measuring fluxes of trace gases and energy between ecosystems and the atmosphere—the state and future of the eddy covariance method. Glob Change Biol 20:3600–3609. doi:10.1111/gcb.12649

Campbell DT, Stanley JC (1963) Experimental and quasi-experimental designs for research. NIDA Res Monogr 107:140–158

Christen A, van Gorsel E, Vogt R, Andretta M, Rotach MW (2001) Ultrasonic anemometer instrumentation at steep slopes: wind tunnel study—field comaprison measurements. MAP Newsl 15:164–167

Dyer AJ (1981) Flow distortion by supporting structures. Boundary-Layer Meteorol 20:363–372

Dyer AJ, Garratt JR, Francey RJ, McIlroy IC, Bacon NE, Bradley EF, Denmead OT, Tsvang LR, Volkov YA, Koprov BM, Elagina LG, Sahashi K, Monji N, Hanafusa T, Tsukamoto O, Frenzen P, Hicks BB, Wesely M, Miyake M, Shaw W (1982) An international turbulence comparison experiment (ITCE-76). Boundary-Layer Meteorol 24:181–209

Foken T, Oncley SP (1995) Workshop on instrumental and methodical problems of land surface flux measurements. Bull Am Meteorol Soc 76:1191–1193

Frank JM, Massman WJ, Ewers BE (2013) Underestimates of sensible heat flux due to vertical velocity measurement errors in non-orthogonal sonic anemometers. Agric For Meteorol 171–172:72–81. doi:10.1016/j.agrformet.2012.11.005

Friebel HC, Herrington TO, Belinov AY, Benilov AY, Belinov AY, Benilov AY (2009) Evaluation of the flow distortion around the Campbell Scientific CSAT3 sonic anemometer relative to incident wind direction. J Atmos Ocean Technol 26:582–592. doi:10.1175/2008JTECHO550.1

Fureby C, Tabor G, Weller H, Gosman A (1997) A comparative study of subgrid scale models in homogeneous isotropic turbulence. Phys Fluids 9:1416–1429. doi:10.1063/1.869254

Grare L, Lenain L, Melville WK (2016) The influence of wind direction on Campbell Scientific CSAT3 and Gill R3-50 sonic anemometer measurements. J Atmos Ocean Technol 33:2477–2497. doi:10.1175/JTECH-D-16-0055.1

Goodrich JPP, Oechel WCC, Gioli B, Moreaux V, Murphy PCC, Burba G, Zona D (2016) Impact of different eddy covariance sensors, site set-up, and maintenance on the annual balance of CO2 and CH4 in the harsh Arctic environment. Agric For Meteorol 228–229:239–251. doi:10.1016/j.agrformet.2016.07.008

Hanafusa T, Fujitani T, Kobori Y, Mitsuta Y (1982) A new type sonic anemometer–thermometer for field operation. Pap Meteorol Geophys 33:1–19

Högström U, Smedman AS (2004) Accuracy of sonic anemometers: laminar wind-tunnel calibrations compared to atmospheric in situ calibrations against a reference instrument. Boundary-Layer Meteorol 111:33–54. doi:10.1023/B:BOUN.0000011000.05248.47

Horst TW, Semmer SR, Maclean G (2015) Correction of a non-orthogonal, three-component sonic anemometer for flow distortion by transducer shadowing. Boundary-Layer Meteorol 155:371–395. doi:10.1007/s10546-015-0010-3

Issa R (1985) Solution of the implicitly dsicretized fluid flow equations by operator-splitting. J Comput Phys 62:40–65

Jiménez-Buedo M, Miller LM (2010) Why a trade-off? The relationship between the external and internal validity of experiments. Theoria 69:301–321. doi:10.1387/theoria.779

Kaimal J (1978) Sonic anemometer measurement of atmospheric turbulence. In: Hanson BW (ed) Proceedings of the dynamic flow conference 1978 on dynamic measurements in unsteady flows. Springer, Dordrecht, pp 551–565

Kaimal JC (2013) Advances in meteorology and the evolution of sonic anemometry. http://www.apptech.com/wp-content/uploads/2016/08/Evolution-of-Sonic-Anemometry.pdf. Accessed 4 Feb 2017

Kaimal JC, Gaynor JE (1983) The boulder atmospheric observatory. J Appl Meteorol 22:863–880

Kaimal JC, Finnigan JJ (1994) Atmospheric boundary layer flows: their structure and measurement. Oxford University Press, New York

Kaimal JC, Wyngaard JC, Izumi Y, Cote OR (1972) Spectral characteristics of surface layer turbulence. Q J R Meteorol Soc 53:103–115

Kaimal JC, Gaynor JE, Zimmerman HA, Zimmerman GA (1990) Minimizing flow distortion errors in a sonic anemometer. Boundary-Layer Meteorol 53:103–115. doi:10.1007/BF00122466

Karniadakis GE, Triantafyllou GS (1989) Frequency selection and asymptotic states in laminar wakes. J Fluid Mech 199:441–469. doi:10.1017/S0022112089000431

Kochendorfer J, Meyers TP, Heuer MW, Frank JM, Massman WJ, Heuer MW, Frank JM, Massman WJ (2012) How well can we measure the vertical wind speed? Implications for the fluxes of energy and mass. Boundary-Layer Meteorol 145:383–398. doi:10.1007/s10546-012-9738-1

Li M, Babel W, Tanaka K, Foken T (2013) Note on the application of planar-fit rotation for non-omnidirectional sonic anemometers. Atmos Meas Tech 6:221–229. doi:10.5194/amt-6-221-2013

Loescher HW, Ocheltree T, Tanner B, Swiatek E, Dano B, Wong J, Zimmerman G, Campbell J, Stock C, Jacobsen L, Shiga Y, Kollas J, Liburdy J, Law BE (2005) Comparison of temperature and wind statistics in contrasting environments among different sonic anemometer-thermometers. Agric For Meteorol 133:119–139. doi:10.1016/j.agrformet.2005.08.009

Mauder M (2013) A comment on "How well can we measure the vertical wind speed? Implications for fluxes of energy and mass" by Kochendorfer et al. Boundary-Layer Meteorol 147:329–335. doi:10.1007/s10546-012-9794-6

Mauder M, Liebethal C, Göckede M, Leps JP, Beyrich F, Foken T (2006) Processing and quality control of flux data during LITFASS-2003. Boundary-Layer Meteorol 121:67–88. doi:10.1007/s10546-006-9094-0

Mauder M, Oncley SP, Vogt R, Weidinger T, Ribeiro L, Bernhofer C, Foken T, Kohsiek W, Bruin HaR, Liu H (2007) The energy balance experiment EBEX-2000. Part II: intercomparison of eddy-covariance sensors and post-field data processing methods. Boundary-Layer Meteorol 123:29–54. doi:10.1007/s10546-006-9139-4

Miyake M, Stewart RW, Burling HW, Tsvang LR, Koprov BM, Kuznetsov OA (1971) Comparison of acoustic instruments in an atmospheric turbulent flow over water. Boundary-Layer Meteorol 2:228–245

Nakai T, Shimoyama K (2012) Ultrasonic anemometer angle of attack errors under turbulent conditions. Agric For Meteorol 162–163:14–26. doi:10.1016/j.agrformet.2012.04.004

Nakai T, van der Molen MK, Gash JHC, Kodama Y (2006) Correction of sonic anemometer angle of attack errors. Agric For Meteorol 136:19–30. doi:10.1016/j.agrformet.2006.01.006

Roe BE, Just DR (2009) Internal and extrernal validity in economics research: tradeoffs between experiments and field data. Am J Agric Econ 91:1266–1271. doi:10.1111/j.1467-8276.2009.01295.x

Sakamoto H, Haniu H (1990) A study on vortex shedding from spheres in a uniform flow. J Fluid Eng 112:386–392. doi:10.1115/1.2909415

SanClements MD, Metzger S, Luo H, Pingintha-Durden N, Zulueta R, Loescher HW (2014) The National Ecological Observatory Network (NEON): providing free long-term ecological data on a continental scale. iLEAPS Newsletter. Issue Spec Issue Environ Res Infrastruct 23–26

Schlegel F, Stiller J, Bienert A, Maas HG, Queck R, Bernhofer C (2012) Large-eddy simulation of inhomogeneous canopy flows using high resolution terrestrial laser scanning data. Boundary-Layer Meteorol 142:223–243. doi:10.1007/s10546-011-9678-1

Tsvang LR, Koprov BM, Zubkovskii SL, Dyer AJ, Hicks B, Miyake M, Stewart RW, McDonald JW (1973) A comparison of turbulence measurements by different instruments; Tsimlyansk field experiment 1970. Boundary-Layer Meteorol 3:499–521

Tsvang LR, Zubkovskij SL, Kader BA, Kallistratova MA, Foken T, Gerstmann W, Przandka Z, Pretel J, Zelenny J, Keder J (1985) International turbulence comparison experiment (ITCE-81). Boundary-Layer Meteorol 31:325–348

van der Molen M, Gash JH, Elbers J (2004) Sonic anemometer (co)sine response and flux measurement. Agric For Meteorol 122:95–109. doi:10.1016/j.agrformet.2003.09.003

Weller HG, Tabor G, Jasak H, Fureby C (1998) A tensorial approach to computational continuum mechanics using object-oriented techniques. Comput Phys 12:620–631. doi:10.1063/1.168744

Wieser A, Fiedler F, Corsmeier U (2001) The influence of the sensor design on wind measurements with sonci anemometer systems. J Atmos Ocean Technol 18:1585–1608

Williamson CHK (1996) Vortex dynamics in the cylinder wake. Annu Rev Fluid Mech 28:477–539. doi:10.1146/annurev.fl.28.010196.002401

Wyngaard JC (1981) The effects of probe-induced flow distortion on atmospheric turbulence measurements. J Appl Meteorol 20:784–794. doi:10.1175/1520-0469(1988)045<3400:TEOPIF>2.0.CO;2

Wyngaard JC (1988) Flow-distortion effects on scalar flux measurements in the surface layer: implications for sensor design. Boundary-Layer Meteorol 42:19–26. doi:10.1007/BF00119872

Wyngaard JC, Zhang S-FF (1985) Transducer-shadow effects on turbulence spectra measured by sonic anemometers. J Atmos Ocean Technol 2:548–558. doi:10.1175/1520-0426(1985)002<0548:TSEOTS>2.0.CO;2

Yu GR, Wen X-F, Sun X-M, Tanner BD, Lee X, Chen J-Y (2006) Overview of ChinaFLUX and evaluation of its eddy covariance measurement. Agric For Meteorol 137:125–137

Zacharias S, Bogena H, Samaniego L, Mauder M, Fuß R, Pütz T, Frenzel M, Schwank M, Baessler C, Butterbach-Bahl K, Bens O (2011) A network of terrestrial environmental observatories in Germany. Vadose Zone J 10:955–973

Zhang SF, Wyngaard JC, Businger JA, Oncley SP (1986) Response characteristics of the U.W. sonic anemometer. J Atmos Ocean Technol 3:315–323. doi:10.1175/1520-0426(1986)003<0315:RCOTUS>2.0.CO;2

C. Vertically nested LES for high-resolution simulation of the surface layer in PALM (version 5.0)

Huq, S., Roo, F. D., Raasch, S., & Mauder, M. (2019). Vertically nested LES for high-resolution simulation of the surface layer in PALM (version 5.0). Geoscientific Model Development, 12 (6), 2523–2538. https://doi.org/10.5194/gmd-12-2523-2019

Geosci. Model Dev., 12, 2523–2538, 2019
https://doi.org/10.5194/gmd-12-2523-2019

Geoscientific Model Development
Open Access
EGU

Vertically nested LES for high-resolution simulation of the surface layer in PALM (version 5.0)

Sadiq Huq[1], **Frederik De Roo**[1,4], **Siegfried Raasch**[3], **and Matthias Mauder**[1,2]

[1]Institute of Meteorology and Climate Research, Atmospheric Environmental Research (IMK-IFU), Karlsruhe Institute of Technology (KIT), Kreuzeckbahnstrasse 19, 82467 Garmisch-Partenkirchen, Germany
[2]Institute of Geography and Geoecology (IfGG), Karlsruhe Institute of Technology, Kaiserstrasse 12, 76131 Karlsruhe, Germany
[3]Institute of Meteorology and Climatology, Leibniz Universität Hannover, Hanover, Germany
[4]Norwegian Meteorological Institute, Oslo, Norway

Correspondence: Matthias Mauder (matthias.mauder@kit.edu)

Received: 15 November 2018 – Discussion started: 3 December 2018
Revised: 16 April 2019 – Accepted: 4 June 2019 – Published: 28 June 2019

Abstract. Large-eddy simulation (LES) has become a well-established tool in the atmospheric boundary layer research community to study turbulence. It allows three-dimensional realizations of the turbulent fields, which large-scale models and most experimental studies cannot yield. To resolve the largest eddies in the mixed layer, a moderate grid resolution in the range of 10 to 100 m is often sufficient, and these simulations can be run on a computing cluster with a few hundred processors or even on a workstation for simple configurations. The desired resolution is usually limited by the computational resources. However, to compare with tower measurements of turbulence and exchange fluxes in the surface layer, a much higher resolution is required. In spite of the growth in computational power, a high-resolution LES of the surface layer is often not feasible: to fully resolve the energy-containing eddies near the surface, a grid spacing of O(1 m) is required. One way to tackle this problem is to employ a vertical grid nesting technique, in which the surface is simulated at the necessary fine grid resolution, and it is coupled with a standard, coarse, LES that resolves the turbulence in the whole boundary layer. We modified the LES model PALM (Parallelized Large-eddy simulation Model) and implemented a two-way nesting technique, with coupling in both directions between the coarse and the fine grid. The coupling algorithm has to ensure correct boundary conditions for the fine grid. Our nesting algorithm is realized by modifying the standard third-order Runge–Kutta time stepping to allow communication of data between the two grids. The two grids are concurrently advanced in time while ensuring that the sum of resolved and sub-grid-scale kinetic energy is conserved. We design a validation test and show that the temporally averaged profiles from the fine grid agree well compared to the reference simulation with high resolution in the entire domain. The overall performance and scalability of the nesting algorithm is found to be satisfactory. Our nesting results in more than 80 % savings in computational power for 5 times higher resolution in each direction in the surface layer.

1 Introduction

Turbulence in the atmospheric boundary layer (ABL) encompasses a wide range of scales from the boundary-layer scale down to the viscous dissipation scale. In ABL flows, Reynolds numbers (Re) of 10^8 are commonly encountered. Explicit simulation of the Navier–Stokes equations down to the dissipative scales (DNS: direct numerical simulation) for atmospheric processes is prohibitively expensive, as the required number of grid points in one direction scales with $Re^{3/4}$ (Reynolds, 1990). This corresponds to a three-dimensional ABL simulation domain with a total number of grid points of order 10^{17}. The supercomputers of today cannot fit more than 10^{12} grid points in their memory. To be able to compute turbulence processes in the atmosphere nevertheless, the concept of large-eddy simulation (LES) was introduced already a few decades ago,

e.g., Deardorff (1974), Moeng and Wyngaard (1988) and Schmidt and Schumann (1989), where the presence of a sub-grid-scheme allows that only the most energetic eddies are resolved. One of the first large-eddy simulations (LESs) by Deardorff (1974) used 64 000 grid points to simulate a domain of $5\,\mathrm{km} \times 5\,\mathrm{km} \times 2\mathrm{km}$ with a grid resolution of $(125, 125, 50)$ m. The size of one such grid cell is just sufficient to resolve the dominant large eddies, and there are just enough grid points to represent the ABL. As computing power progressed, higher resolution and larger domains became possible. By the time of Schmidt and Schumann (1989) the number of grid cells had risen to $160 \times 160 \times 48$, simulating an ABL of $8\,\mathrm{km} \times 8\,\mathrm{km} \times 2.4\,\mathrm{km}$ with a resolution of $(50, 50, 50)$ m. Khanna and Brasseur (1998) used 128^3 grid points to simulate a domain of $3\,\mathrm{km} \times 3\,\mathrm{km} \times 1\,\mathrm{km}$ to study buoyancy and shear-induced local structures of the ABL. Patton et al. (2016) used $(2048, 2048, 1024)$ grid points with a grid resolution of $(2.5, 2.5, 2)$ m to study the influence of atmospheric stability on canopy turbulence. More recently, Kröniger et al. (2018) used 13×10^9 grid points to simulate a domain of $30.72\,\mathrm{km} \times 15.36\,\mathrm{km} \times 2.56\,\mathrm{km}$ to study the influence of stability on the surface–atmosphere exchange and the role of secondary circulations in the energy exchange. The atmospheric boundary layer community has greatly benefited from the higher spatial resolution available in these LES to study turbulent processes that cannot be obtained in field measurements. Still, especially in heterogeneous terrain, near topographic elements and buildings or close to the surface, the required higher resolution is not always attainable due to computational constraints. In spite of the radical increase in the available computing power over the last decade, large-eddy simulation of high Reynolds number atmospheric flows with very high resolution in the surface layer remains a challenge. Considering the size of the domain required to reproduce boundary-layer-scale structures, it is computationally demanding to generate a single fixed grid that could resolve all relevant scales satisfactorily. Alternatively, local grid refinement is possible in the finite volume codes that are not restricted to structured grids. Flores et al. (2013) developed a solver for the OpenFOAM modeling framework to simulate atmospheric flows over complex geometries using an unstructured mesh approach. The potential of the adaptive mesh refinement technique in which the tree-based Cartesian grid is refined or coarsened dynamically, based on the flow structures, is demonstrated by van Hooft et al. (2018). In the finite difference models, a grid nesting technique can be employed to achieve the required resolution. In the nested grid approach, a parent domain with a coarser resolution simulates the entire domain, while a nested grid with a higher resolution extends only up to the region of interest. Horizontal nesting has been applied to several mesoscale models (Skamarock et al., 2008; Debreu et al., 2012). Horizontally nested LES-within-LES or LES embedded within a mesoscale simulation is available in the Weather Research and Forecast model (Moeng et al., 2007). Comparable grid nesting techniques are also widely employed by the engineering turbulence research community but often use different terminology. Nesting in codes with Cartesian grids is referred to as local or zonal grid algorithm (Kravchenko et al., 1996; Boersma et al., 1997; Manhart, 2004) and as overset mesh (Nakahashi et al., 2000; Kato et al., 2003; Wang et al., 2014) in unstructured or moving grid codes.

For our purposes, we will focus on vertical nesting; i.e., we consider a fine grid nested domain (FG) near the lower boundary of the domain and a coarse grid parent domain (CG) in the entirety of the boundary layer. While the latter's resolution ($< 50\,\mathrm{m}$) is sufficient to study processes in the outer region where the dominant eddies are large and inertial effects dominate, such coarse resolution is not sufficient where fine-scale turbulence in the surface layer region is concerned. The higher resolution achieved by the vertical nesting will then allow a more accurate representation of the turbulence in the surface layer region, by resolving its dominant eddies. For studies that require very high resolution near the surface (e.g., virtual tower measurements, wakes behind obstacles, dispersion within street canyons for large cities), a nesting approach is an attractive solution due to the reduced memory requirement. A challenge of the vertically nested simulation is that the FG upper boundary conditions need to be correctly prescribed by the CG. Though vertical nesting is less common than the horizontal nesting, it has been implemented in some LES models. A non-parallelized vertical nesting was explored by Sullivan et al. (1996), but the code is not in the public domain, and we could not find any record of further development or application of this code in publications. A LES-within-LES vertical nesting is implemented by Zhou et al. (2018) in the Advanced Regional Prediction System (ARPS) model. We would like to point out that the vertical nesting available in the Weather Research and Forecast model (Daniels et al., 2016) is not a conventional vertical nesting because the parent and the child grid still have the same vertical extent; the child grid is only more refined in the vertical.

An analysis of different nesting procedures for mesoscale simulation was performed by Clark and Hall (1991); they coined the terms "one-way" and "two-way" interactions. In one-way interaction, only the FG receives information from the CG, and there is no feedback to the CG. In two-way interaction, the FG top boundary conditions are interpolated from the CG, and the CG values in the overlapping region are updated with the FG resolved fields. The "update" process, referred to as "anterpolation" by Sullivan et al. (1996), is similar to the restriction operation in multi-grid methods. Harris and Durran (2010) used a linear 1-D shallow-water equation to study the influence of the nesting method on the solution and found the two-way interaction to be superior if the waves are well resolved. They introduce a filtered sponge boundary condition to reduce the amplitude of the reflected wave at the nested grid boundary. We will make use of the interpolation and anterpolation formulas of Clark and Farley (1984). Clark

and Hall (1991) studied two different approaches for updating the CG values, namely "post-insertion" and "pressure defect correction". The two approaches were also investigated by Sullivan et al. (1996) in their vertical nesting implementation. In the post-insertion technique, once the Poisson equation for pressure is solved in the FG, the resolved fields are then anterpolated to the CG. In the pressure defect correction approach, the pressure in the CG and FG are matched by adding a correction term to the CG momentum equations, and an anterpolation operation is not required. Though Sullivan et al. (1996) note the pressure defect correction approach to be more elegant, no significant difference in the results was reported. In the following sections we describe the technical realization and numerical aspects of the two-way nesting algorithm. In the LES model PALM, a validation simulation is set up, and the results of the nested and stand-alone simulations are compared. A second simulation is set up to evaluate the computational performance of the algorithm. The practical considerations and the limitations of the two-way nesting are then discussed.

2 Methods

2.1 Description of the standard PALM

The Parallelized Large-eddy simulation Model (PALM) is developed and maintained at the Leibniz University of Hanover (Raasch and Schröter, 2001; Maronga et al., 2015). We give a quick summary of the model here and highlight the aspects which will reappear when discussing our nesting modifications. PALM is a finite difference solver for the non-hydrostatic incompressible Navier–Stokes equations in the Boussinesq approximation. PALM solves for six prognostic equations: the three components of the velocity field (u, v, w), potential temperature (θ), humidity (q) and the sub-grid-scale kinetic energy (e). The sub-grid-scale (SGS) turbulence is modeled based on the method proposed by Deardorff (1980). The equations for the conservation of mass, energy and moisture (Eqs. 1, 2, 3 and 4) are filtered over a grid volume on a Cartesian grid. Adopting the convention of Maronga et al. (2015), the overbar denoting the filtered variables is omitted. However, the overbar is shown for SGS fluxes. The SGS variables are denoted by a double prime. The prognostic equations for the resolved variables are

$$\frac{\partial u_i}{\partial t} = -\frac{\partial u_i u_j}{\partial x_j} - \varepsilon_{ijk} f_j u_k + \varepsilon_{i3k} f_3 u_{k_{g,j}} - \frac{1}{\rho_0}\frac{\partial \pi^*}{\partial x_i} + g\frac{\theta_v - \langle\theta_v\rangle}{\theta_v}\delta_{i3} - \frac{\partial}{\partial x_j}\left(\overline{u_i'' u_j''} - \frac{2}{3}e\delta_{ij}\right), \quad (1)$$

$$\frac{\partial u_j}{\partial x_j} = 0, \quad (2)$$

$$\frac{\partial \theta}{\partial t} = -\frac{\partial u_j \theta}{\partial x_j} - \frac{\partial}{\partial x_k}\left(\overline{u_j'' \theta''}\right) - \frac{L_V}{c_p \Pi}\Psi_{q_v}, \quad (3)$$

$$\frac{\partial q_v}{\partial t} = -\frac{\partial u_j q_v}{\partial x_j} - \frac{\partial}{\partial x_k}\left(\overline{u_j'' q_v''}\right) + \Psi_{q_v}. \quad (4)$$

The symbols used in the above equations are listed in Table 1. The 1.5-order closure parameterization modified by Moeng and Wyngaard (1988) and Saiki et al. (2000) assumes a gradient diffusion parameterization (Eqs. 6, 7, 8). The prognostic equation for the SGS turbulent kinetic energy (TKE) reads as

$$\frac{\partial e}{\partial t} = -u_j\frac{\partial e}{\partial x_j} - \left(\overline{u_i'' u_j''}\right)\frac{\partial u_i}{\partial x_k} + \frac{g}{\theta_{v,0}}\overline{u_3'' \theta_v''} - 2K_m\frac{\partial e}{\partial x_j} - \epsilon, \quad (5)$$

with the SGS fluxes modeled as

$$\overline{u_i'' u_j''} - \frac{2}{3}e\delta_{ij} = -K_m\left(\frac{\partial u_i}{\partial x_j} + \frac{\partial u_j}{\partial x_i}\right), \quad (6)$$

$$\overline{u_i'' \theta''} = -K_h\frac{\partial \theta}{\partial x_i} \quad (7)$$

and

$$\overline{u_i'' q_v''} = -K_h\frac{\partial \theta}{\partial x_i}. \quad (8)$$

The eddy diffusivities are proportional to $e^{3/2}$ under convective conditions (Maronga et al., 2015). For a thorough description of the governing equations and parameterizations, see Maronga et al. (2015).

The prognostic equations are discretized on a staggered Arakawa C grid, where the scalars are evaluated in the center of the grid volume, and velocities are evaluated at the center of the faces of the grid volume in their respective direction. The advection terms are evaluated either with fifth-order upwind discretization according to Wicker and Skamarock (2002) or with a second-order scheme according to Piacsek and Williams (1970). The prognostic equations are integrated in time using a third-order Runge–Kutta (RK3) scheme. The low storage RK3 scheme with three sub-steps proposed by Williamson (1980) guarantees a stable numerical solution. The Poisson equation for pressure is solved with a fast Fourier transform (FFT) when periodic boundary conditions are applied in the lateral boundaries. There are three FFT algorithms available in PALM, with Fastest Fourier Transform in the West (FFTW) being the optimal method for large-scale simulations. Monin–Obukhov similarity theory (MOST) is assumed between the surface and the first grid point. A vertical zero pressure gradient at the surface guarantees the vertical velocity to be zero. Simulations can be driven by either prescribing the surface temperature or the surface sensible heat flux, similarly for the humidity. At the top of the simulation domain the horizontal velocities equal geostrophic wind, and the vertical velocity is set to zero. The pressure can assume either a Dirichlet condition of zero value or a Neumann condition of zero vertical gradient. The scalar values can have either a fixed value Dirichlet condition or a fixed gradient Neumann condition. The vertical gradient of SGS turbulent kinetic energy (TKE) is set to

Table 1. List of symbols in the governing equations and parameterizations.

Symbol	Description
f_i	Coriolis parameter
ρ_0	Density of dry air at the surface
π^*	Modified perturbation pressure
g	Gravitational acceleration
θ_v	Virtual potential temperature
L_v	Latent heat of vaporization
C_p	Heat capacity of dry air at constant pressure
q_v	Specific humidity
Ψ_{q_v}	Source/sink term of q_v
Π	Exner function for converting between temperature and potential temperature
K_h	SGS eddy diffusivity of heat
K_m	SGS eddy diffusivity of momentum

zero at both top and bottom boundaries. PALM is a parallelized model, and the standard way of parallelization is by dividing the three-dimensional domain into vertical columns, each of which is assigned to one processing element (PE). Each vertical column possesses a number of ghost points needed for computation of derivatives at the boundary of the sub-domains. Each PE can only access data for a single sub-domain. All PEs execute the same program on a different set of data. For optimum load balancing between the PEs, the decomposed sub-domains should have the same size. In PALM, this condition is always satisfied as only sub-domains of the same size are allowed. The data exchange between PEs needed by the Poisson solver and to update the ghost points is performed via the Message Passing Interface (MPI) communication routines.

2.2 Nested model structure

2.2.1 Fine grid and coarse grid configuration

We are interested in achieving an increased resolution only in the surface layer, the lowest 10 % of the boundary layer, where surface exchange processes occur and where eddies generated by surface heterogeneity and friction are smaller than the dominant eddies in the mixed layer. We set up the LES-within-LES case by maintaining the same horizontal extent for the FG and the CG to have the whole surface better resolved. We allow the vertical extent of the FG to be varied as needed, typically up to the surface layer height. This implementation of vertical grid nesting has two main challenges. The first challenge, that is purely technical in nature, is to implement routines that handle the communication of data between the CG and the FG. The second and the most important challenge is to ensure that the nesting algorithm yields an accurate solution in both grids. Below we use upper case symbols for fields and variables in the CG and lower case for the FG; e.g., E and e denote the sub-grid-scale turbulent kinetic energy (a prognostic variable in our LES) of CG and FG respectively. The nesting ratio is defined as the ratio of the CG spacing to the FG spacing, and $n_x = \Delta X/\Delta x$; corresponding symbols apply for y and z directions. The nesting ratios n_x, n_y and n_z have to be integers. It is possible to have either an odd or even nesting ratio, and it can be different in each direction. As the domain that is simulated in the FG is completely inside of the CG domain, each FG cell belongs to a CG cell. The two grids are positioned in such a way that a FG cell belongs to only one CG cell, and one CG cell is made up by a number of FG cells given by the product of the nesting ratios $n_x \times n_y \times n_z$. This means that if the grid nesting ratio is odd, there will be one FG cell whose center is exactly at the same position as the center of the coarse cell as shown in Fig. 1b. The collection of FG cells that correspond to one CG cell is denoted by $\mathcal{C}(I, J, K)$. The collection of yz faces of the FG that corresponds to a yz face of the CG is denoted by $\mathcal{C}_x(I_\mathrm{s}, J, K)$, where it is understood that the I_s index is an index on the staggered grid in the x direction to denote the position of the face, and this is similar for the other types of faces. We have used $f_x = 1/n_x$ to denote the inverse of the nesting ratio in the x dimension (corresponding symbols for y and z). A schematic diagram of the overlapping grids is shown in Fig. 1a.

2.2.2 Vertical nesting algorithm

We implement a two-way interaction algorithm, shown in Fig. 2, because in our first trials we found that one-way nesting did not improve the FG representation satisfactorily and hence was not pursued further. The FG prognostic quantities are initialized by interpolating the CG values in the overlapping region. Optionally, the initialization of the FG can be delayed until the CG has reached a fully turbulent state. Both grids are restricted to have identical time steps. PALM finds the largest time step for each grid such that the Courant–Friedrichs–Lewy (CFL) condition is individually satisfied, and the minimum of the two values is then chosen as the time integration step for both grids. The right-hand side of

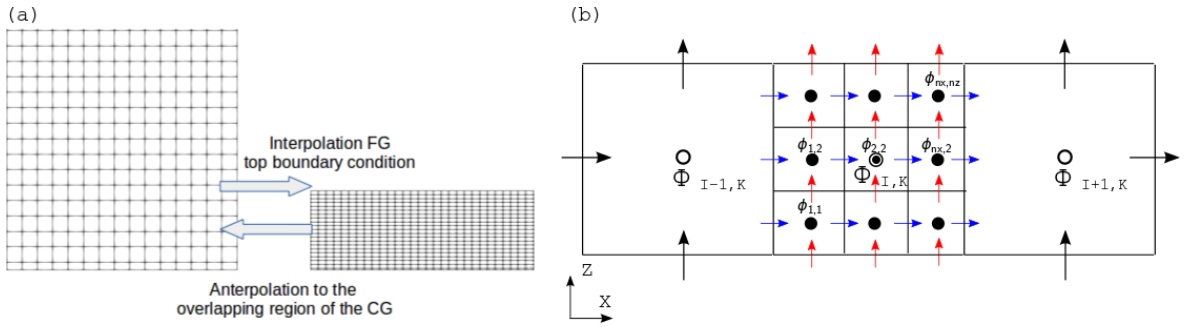

Figure 1. **(a)** Schematic of the interpolation and anterpolation between grids. The FG top boundary condition is interpolated from the CG. The CG prognostic quantities in the overlapping region are anterpolated from the FG. **(b)** Schematic of Arakawa C grid for two grids with nesting ratio of 3. The black arrows and circles are CG velocity and pressure, respectively. The blue and red arrows are horizontal and vertical velocity, respectively, in the FG. The filled black circle is the FG pressure. The symbols Φ and ϕ represent CG and FG scalar quantities. I and K are CG indices and nx and nz are the nesting ratio in x and z, respectively.

the prognostic equation except for the pressure is first computed concurrently in both grids. The values of u, v, w, θ and q are then anterpolated to the CG in the overlapping region. The CG solves a Poisson equation for pressure. The new u, v, w, θ and q fields in the CG are interpolated to set the FG Dirichlet top boundary conditions. The Poisson equation is then solved for pressure in the FG, and the vertical velocity in the FG is also updated by the pressure solver at this stage. Since all the velocity components follow a Dirichlet condition at the FG top boundary, only a Neumann condition is suitable for pressure (Manhart, 2004). PALM permits the use of a Neumann zero-gradient condition for pressure at both the top and bottom boundary. It is advisable to use a Neumann boundary condition at the top and the bottom for the CG too. The TKE is then anterpolated maintaining the Germano identity, and it is followed by the computation of SGS eddy diffusivity for heat (k_h) and momentum (k_m) in the CG. This procedure is repeated at every sub-step of the Runge–Kutta 3 time integration, and it ensures that the velocity field remains divergence free in both grids.

In the 1.5-order turbulence closure parameterization, all the sub-grid fluxes are derived from the turbulent kinetic energy and the resolved gradients at each time step. Therefore, the sub-grid fluxes do not have to be interpolated from CG to FG at the top boundary. Furthermore, in our implementation of the nesting method, we assume that most of the TKE is resolved well down to the inertial subrange, except for the lowest few grid layers. This allows us to use the zero-gradient Neumann boundary condition for TKE at the FG top boundary. We employ a simplified sponge layer by limiting the anterpolation of all prognostic quantities to one CG cell fewer than the nested height. This segregation of the anterpolation region in the CG and top boundary condition level of the FG ensures that the flow structures in the CG propagate into the FG without distortion due to numerical artifacts.

2.3 Translation between grids

2.3.1 Interpolation

For the boundary conditions at the top of the FG, the fields from the CG are interpolated to the FG, according to Clark and Farley (1984). We define the top of the FG as the boundary level just above the prognostic level of each quantity. In Eq. (10), Φ and ϕ represent CG and FG quantities, respectively. For the scalar fields, the interpolation is quadratic in all three directions. For the velocity components, the interpolation is linear in its own dimension and quadratic in the other two directions. The same interpolation formulation is also used to initialize all vertical levels of the fine grid domain at the beginning of the nested simulation. The interpolation is reversible as it satisfies the conservation condition of Kurihara et al. (1979):

$$< \phi >=< \Phi > . \tag{9}$$

For clarity, we illustrate the interpolation by focusing on one particular dimension, in this case x, but the same operation holds for y and z. The interpolation in the x dimension reads as

$$\phi_m = \eta_-^m \Phi_{I-1} + \eta_0^m \Phi_I + \eta_+^m \Phi_{I+1}, \tag{10}$$

with m running from 1 to n_x, thus producing n_x equations for each CG cell I. For the interpolation in y and z there will be two additional indices, producing $n_x \times n_y \times n_z$ equations for all the FG cells corresponding to the CG parent cell. For the quadratic interpolation a stencil with three legs is used, relating the prognostic value of a FG cell to the value of its parent CG and the values of the immediate CG neighbor on the left and on the right of the parent cell, e.g., Φ_{I-1} and Φ_{I+1} for the x direction as shown in Fig. 1b. The stencil coefficients are

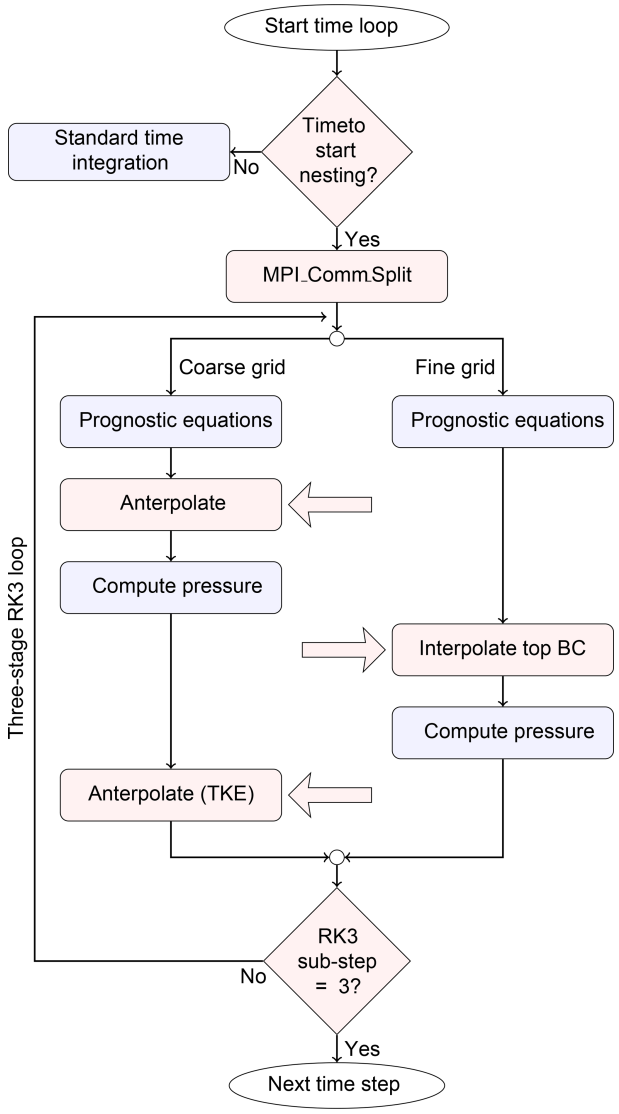

Figure 2. A flowchart of the two-way interaction algorithm. The new routines needed for the vertical nesting are highlighted in red and the standard routines are highlighted in blue. An arrow pointing to the left indicates transfer of data from FG to CG, and vice versa.

$$\begin{aligned}\eta_{-}^{m} &= \frac{1}{2}H_m(H_m-1)+\alpha,\\ \eta_{0}^{m} &= (1-H_m^2)-2\alpha,\\ \eta_{+}^{m} &= \frac{1}{2}H_m(H_m+1)+\alpha\,,\end{aligned} \tag{11}$$

with the weights H_m expressed in function of the inverse nesting ratio,

$$H_m = \frac{1}{2}((2m-1)f_x - 1)\,, \tag{12}$$

and the coefficient α is chosen such that the conservation condition of Kurihara et al. (1979) is satisfied:

$$\alpha = \frac{1}{24}\left(f_x^2 - 1\right). \tag{13}$$

It can be observed that the sum of the ηs equals 1.

2.3.2 Anterpolation

The anterpolation of the prognostic quantities is performed by an averaging procedure according to Clark and Hall (1991). The anterpolation equations for the velocities read as

$$\begin{aligned}U_{I,J,K} &= <u>_{j,k} = \sum_{j,k\in\mathcal{C}_{\mathcal{IJK}}} u_{i^*,j,k} f_y f_z\,,\\ V_{I,J,K} &= <v>_{i,k} = \sum_{i,k\in\mathcal{C}_{\mathcal{IJK}}} v_{i,j^*,k} f_x f_z\,,\\ W_{I,J,K} &= <w>_{i,j} = \sum_{i,j\in\mathcal{C}_{\mathcal{IJK}}} w_{i,j,k^*} f_x f_y\,.\end{aligned} \tag{14}$$

For the scalars it is

$$\Phi_{I,J,K} = [\phi]_{i,j,k} = \sum_{i,j,k\in\mathcal{C}_{\mathcal{IJK}}} \phi_{i,j,k} f_x f_y f_z\,. \tag{15}$$

Here the lower case indices only count over the fine grid cells that belong to that particular coarse grid cell. For each (I, J, K) tuple of a parent CG cell, there exists a set $\mathcal{C}_{\mathcal{IJK}}$ containing the (i, j, k) tuples of its corresponding children FG cells. To ensure that the nested PALM knows at all times which fine grid cells and coarse grid cells correspond, we compute this mapping for the FG and CG indices before starting the simulation, and we store it in the memory of the parallel processing element. In the Arakawa C grid discretization that PALM uses, the scalars are defined as the spatial average over the whole grid cell, and therefore it is required that the CG scalar is the average of the corresponding FG scalars in (Eq. 15). However, the velocities are defined at the faces of the cells in the corresponding dimension. Therefore in (Eq. 14) the CG velocity components are computed as the average over the FG values at the FG cells that correspond to the face of the CG cell, expressed by i^*, j^*, k^* respectively.

However, the TKE in the CG differs from the FG value, due to the different resolution of grids. In the FG the SGS motions are weaker because the turbulence is better resolved. Therefore, TKE is anterpolated such that the sum of resolved kinetic energy and TKE (SGS kinetic energy) is preserved, by maintaining the Germano identity (Germano et al., 1991):

$$E = [e] + \frac{1}{2}\sum_{n=1}^{3}([u_n u_n] - [u_n][u_n])\,. \tag{16}$$

Here the straight brackets are the spatial average over the coarse grid cell ($f_x f_y f_z \times \sum_{i,j,k\in\mathcal{C}_{IJK}}$), and the n index runs

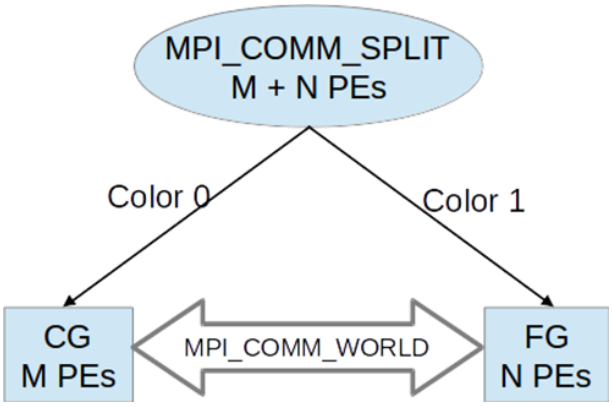

Figure 3. Schematic of the MPI processor grouping. The data exchange between the two groups is performed via the global communicator. *M* and *N* are the number of processors for CG and FG respectively.

over the three spatial dimensions. In other words, to obtain the CG TKE from the average FG TKE, we add the variance of the FG velocity components over the FG cells comprising the CG cell. Therefore CG TKE is always larger than FG TKE.

2.4 Parallel inter-grid communication

MPI is the most widely used large-scale parallelization library. The atmosphere–ocean coupling in PALM has been implemented following MPI-1 standards (Esau, 2014; Maronga et al., 2015). We follow a similar approach for the MPI communications and have adopted MPI-1 standards for our nesting implementation. Concurrent execution of the two grids is achieved with the MPI_COMM_SPLIT procedure. The total available processors are split into two groups, denoted by color 0 or 1 for CG and FG respectively; see Fig. 3. The data between the processors of the same group are exchanged via the local communicator created during the splitting process, whereas the data between the two groups are exchanged via the global communicator MPI_COMM_WORLD.

Based on the nesting ratio and the processor topology of the FG and the CG group, a mapping list is created and stored. Given the local PE's 2-D processor co-ordinate, the list will identify the PEs in the remote group to/from which data need to be sent/received; the actual communication then takes place via the global communicator. There are three types of communication in the nesting scheme:

i. *Initialization of the FG*. (Send data from coarse grid to fine grid.) This is performed only once.

ii. *Boundary condition for the FG top face*. (Send data from coarse grid to fine grid.)

iii. *Anterpolation*. (Send data from fine grid to coarse grid.)

The exchange of arrays via MPI_SENDRECV routines is computationally expensive. Therefore, the size of the arrays communicated is minimized by performing the anterpolation operation in the FG PEs and storing the values in a temporary 3-D array that is later sent via the global communicator to the appropriate CG PE. This approach is more efficient than performing the anterpolation operation on the CG which has fewer PEs and needs communication of larger arrays from the FG. Furthermore, the array data that need to be communicated during the anterpolation operation and for setting the FG boundary condition are not contiguous in memory. The communication performance is enhanced by creating an MPI-derived data type that ensures that the data are sent contiguously. Within the RK3 sub-steps, when one grid executes the pressure solver, the other grid has to wait, leading to more computational time at every sub-step. However, the waiting time can be minimized by effective load balancing; i.e., the number of grid points per PE in the CG should be kept lower than in the FG. The reduction in workload per CG PE is achieved with a few additional cores. The reduction in computational time per step in the CG means the waiting time on the FG PE is also reduced.

3 Results and discussion

3.1 Simulation setup for the nesting validation test

To evaluate the accuracy of the two-way nesting algorithm, we set up a convective boundary layer simulation. Two overlapping grids with a nesting ratio of 5 in the lateral and vertical direction are employed. The simulation parameters are listed in Table 2. A stand-alone reference simulation with the same resolution as the coarse grid (SA-C) and another reference with the same resolution as the fine grid (SA-F) are performed for comparison. The grid configuration and the computational resources used are listed in Table 3. The simulations were performed in a local computing cluster; each compute node has 64 GB of main memory and a 2.8 GHz Ivy Bridge processor with 20 cores. The simulation domain has periodic boundary conditions in the lateral direction. The Dirichlet boundary condition is applied for velocity at the top and bottom boundaries, the vertical velocity component is set to zero and the horizontal components are set to geostrophic wind. At the top and bottom boundaries, the pressure and humidity are set to a zero gradient Neumann condition. The potential temperature is set to a Neumann condition at the bottom, and the gradient is determined by MOST based on the prescribed surface heat flux and roughness length. The gradient of the initial profile is maintained at the top boundary. In PALM, u_g and v_g represents the u and v component of the geostrophic wind at the surface. The u and v initial profiles are set to be constant, equal to the value of the geostrophic wind component in the domain, and the vertical velocity is initialized to zero in the domain. The potential

temperature is initialized to a constant value of 300 K up to 800 m, and above 800 m a lapse rate of 1 K (100 m)$^{-1}$ is prescribed. The humidity profile is initialized to a constant value of 0.005 kg kg^{-1}. The simulation is driven by prescribing a surface heat flux of 0.1 K m s^{-1} and a surface humidity flux of 4×10^{-4} kg kg^{-1} m s^{-1}. The domain is more than 4 times larger in the horizontal than the initial boundary layer height.

3.2 Analysis of the simulations

In a two-way nesting it is important that the flow structures are propagated from the FG to CG and vice versa, without any distortion. In Fig. 4, the contours in the CG region overlapping the FG have similar structures as the FG. The higher resolution in the FG enables more detailed contours, whereas the anterpolated CG contours are smoother. Furthermore, in the CG region beyond the overlapping region, no distortion of the contours is observed, indicating that the anterpolation does not introduce sharp gradients in the CG.

Vertical profiles are used for quantitative comparison of the nested and the reference simulations. The turbulent fluctuations (e.g., θ'', w'') are defined as the spatial deviations from the instantaneous horizontal average. The turbulent fluxes (e.g., $<\overline{w''\theta''}>$, $<\overline{u''u''}>$) are obtained using the spatial covariance and are then horizontally averaged. All the horizontally averaged profiles (e.g., $<\theta>$, $<w''\theta''>$) are also averaged over time, but we omit the conventional overline notation for readability. The convective velocity scale (w_*) and temperature scale (θ_*) obtained from SA-F are used to normalize the profiles. The convective velocity is calculated as $w_* = (g\ \theta_0^{-1}\ H_\mathrm{s}\ z_i)^{1/3}$, where g is the gravitational acceleration, θ_0 is the surface temperature and z_i is the boundary layer height in the simulation. The convective temperature scale is calculated as $\theta_* = H_\mathrm{s}\ w_*^{-1}$. In Fig. 5a and c, the vertical profiles of difference between the potential temperature ($<\theta>$) and its surface value normalized by the convective temperature scale are plotted. Since the FG profiles are superior to the CG in the overlapping region, the anterpolated CG values are not plotted. In Fig. 5a, there is no visible difference between the stand-alone and the nested simulations. However, in the region closer to the surface, plotted in Fig. 5c, a better agreement between the SA-F and FG is observed. The potential temperature variance ($<\theta''\theta''>$) normalized by the square of the temperature scale (θ_*^2) is shown in Fig. 5b and d. Here too FG provides better accuracy close to the surface.

In the vertical heat flux ($<w''\theta''>$) profiles in Fig. 6, the FG has good agreement with the SA-F in the surface layer for the resolved, SGS and the total flux profiles. In the CG regions above the nested grid height, a good agreement with the SA-C is found as well. The improvement due to the two-way nesting is seen in Fig. 6d and e, where the effects of low grid resolution of the SA-C in resolved and SGS fluxes are evident. However, no grid-dependent difference in the profile is observed in the total flux.

The resolved variances of u, v and w normalized by the square of the convective velocity (w_*^2) are plotted in Fig. 7. The FG v and w FG profiles have a better agreement with the SA-F than the u variance. The u and v variances in Fig. 7d and e lie between SA-C and SA-F, indicating that the resolved variances are improved compared to the SA-C but not sufficiently resolved to match SA-F. At the nesting height the variances deviate more from the SA-F and approach the CG values. Due to conservation of total kinetic energy across the nest boundary, more CG TKE is contained in the sub-grid scale. Consequently, the resolved CG variances could have an undershoot as compared to SA-F, resulting in an undershoot of the FG variances too at the nesting height. Above the nesting height, the variance of u, v and w in CG is similar to SA-C.

The resolved vertical velocity skewness in Fig. 8 shows good agreement between the FG and SA-F close to the surface. However, at the nesting height a small kink in the skewness is noticeable. Zhou et al. (2018) observe that the magnitude of the kink in the higher-order profiles can be minimized by increasing the depth of the sponge layer. Our simplified sponge layer approach appears to be unable to effectively minimize the kinks at the nesting height. The resolved skewness in CG is lower than SA-C, possibly due to larger SGS TKE in the CG, as seen in Fig. 8d. The SGS TKE in Fig. 8d shows an exact match between FG and SA-F close to the surface and only marginal difference at the nesting height. However, CG values are considerably different from the SA-C values close to the surface due to the anterpolation maintaining the Germano identity for conservation of kinetic energy across the grids. In the coarse-resolution SA-C, near the surface, the SGS turbulence model appears to insufficiently model the SGS effects. Above the nesting height the CG is similar to SA-C.

The horizontal spectra of SGS turbulent kinetic energy and vertical velocity are plotted in Fig. 9 at two levels, one within the nested grid and one above the nested grid height. The FG TKE spectra in Fig. 9c perfectly overlap the SA-F spectra. The CG spectra have higher energy than the SA-C; this corresponds to the higher CG TKE values observed in Fig. 8c. As the limit of the grid resolution is reached at high wavenumber, the drop in the CG spectra is marginally shifted compared to SA-C. This improvement at high wavenumber is due to feedback from the FG. Similarly, the vertical velocity spectra in Fig. 8d show marginal improvement at high wavenumber for the CG with respect to SA-C. While the FG agrees with SA-C at high wavenumber and at the spectra peak, at low wavenumber FG follows the CG spectra. At the level above the nested grid, the CG spectra agree with SA-C for both TKE and the vertical velocity.

3.3 Computational performance

The computational resources used in the simulations discussed above are listed in Table 3. The resources needed

Table 2. Simulation parameters for the nesting validation test.

Simulation parameters	Value
Domain size:	$4.0 \times 4.0 \times 1.65\,\mathrm{km}^3$
Fine grid vertical extent:	320 m
Kinematic surface heat flux:	$H_\mathrm{s} = 0.1\,\mathrm{K\,m\,s^{-1}}$
Kinematic surface humidity flux:	$\lambda E_\mathrm{s} = 4 \times 10^{-4}\,\mathrm{kg\,kg^{-1}\,m\,s^{-1}}$
Geostrophic wind:	$u_\mathrm{g} = 1\,\mathrm{m\,s^{-1}}$, $v_\mathrm{g} = 0\,\mathrm{m\,s^{-1}}$
Roughness length:	0.1 m
Simulated time:	10 800 s
Spin-up time:	9000 s
Averaging interval:	1800 s

Table 3. Grid configuration of the nested and stand-alone reference domains.

Case	No. of grid points	$(\mathrm{d}x, \mathrm{d}y, \mathrm{d}z)$ m	CPU cores	Core hours	Grid points per core	Time steps
Coarse grid (CG)	$200 \times 200 \times 80 = 3.2 \times 10^6$	20, 20, 20	20	376	1.6×10^5	17 136
Fine grid (FG)	$1000 \times 1000 \times 80 = 80 \times 10^6$	4, 4, 4	80	1503	1.0×10^6	17 136
Total				1879		
Stand-alone coarse (SA-C)	$200 \times 200 \times 80 = 3.2 \times 10^6$	20, 20, 20	20	8	1.6×10^5	3226
Stand-alone fine (SA-F)	$1000 \times 1000 \times 400 = 400 \times 10^6$	4, 4, 4	400	8234	1.0×10^6	18 343

Table 4. Number of grid points in nested and non-nested FG domain.

Case	No. of grid points
Coarse grid	$840 \times 840 \times 288 = 0.20 \times 10^9$
Fine grid	$4200 \times 4200 \times 360 = 6.35 \times 10^9$
Total	6.55×10^9
Non-nested FG	$4200 \times 4200 \times 360 = 6.35 \times 10^9$

by SA-C is only 8 core hours. While the nested simulations needed about 1879 core hours, the SA-F needed about 4 times more core hours than the nested simulation. As the resolution is increased from 20 m in SA-C to 4 m in SA-F, the number of time steps increased more than 5 times as higher resolution demands a smaller time step size. Though the number of time steps in FG is similar to SA-F, limiting the nested grid in the vertical direction has reduced the number of CPU cores needed, and higher resolution in the surface layer is achieved at a reduced computational cost.

Several factors influence the computational performance of an LES code. Some factors depend on the hardware; e.g., the number of grid points per PE depends on the memory available per node. On the other hand, the communication time for data exchange between the PEs depends on the topology of the domain decomposition. The best performance in terms of communication time in a stand-alone run is achieved when the number of sub-domains in the x and y directions is equal. In that case the number of ghost points at the lateral boundaries is optimally minimized. In a nested simulation, the load per PE, i.e., the number of grid points per PE, in the two grids varies. As the speed of the model integration depends on the PE load, the load balancing between the fine and coarse grid has an effect on the computational performance of the nested simulation. Keeping these factors in mind, we designed the nested simulation domains listed in Table 4 for the purpose of assessing the computational performance, as the total number of processors is varied. To avoid load balancing bias in the scalability analysis, the ratio between the number of PEs for CG and FG is kept constant in all the five runs listed in Table 5. Keeping the processor ratio constant implies that the ratio between the number of grid points per PE in CG and FG is also held constant. Consequently, in this performance test, the FG has 1.25 times more grid points per PE than the CG in all the processor configurations tested. To compare the performance of the nested model against the non-nested version of PALM under equivalent work load, a grid with the same dimensions of the FG is set up. This non-nested grid also has the same load per PE and same number of cores as the FG. Such a non-nested setup is acceptable for comparison since the number of PEs in CG is negligible compared to the PE in FG in our setup (e.g., 14 400 PEs in FG and only 576 PEs in CG). A pure stand-alone simulation with FG resolution throughout the boundary layer was not performed as it would need about 2.5×10^{10}

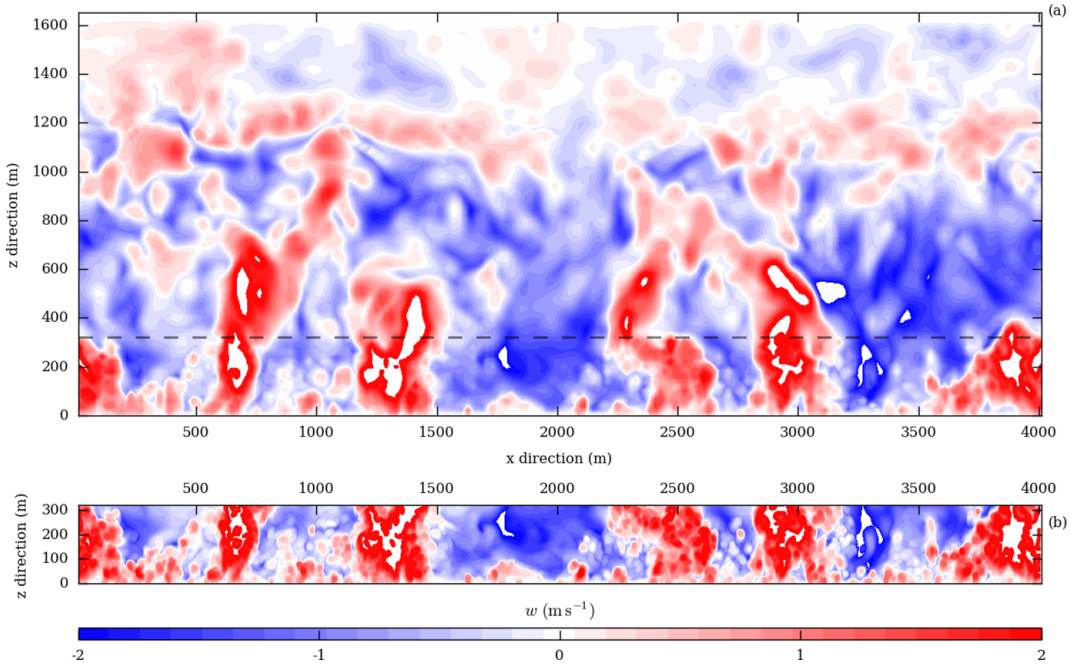

Figure 4. Instantaneous contours of vertical velocity, **(a)** CG and **(b)** FG, at the vertical $x-z$ cross section at the center of the domain after 10 800 s of the simulation. The dashed line in **(a)** marks the top of the overlapping region. Flow structures in the FG, which are similar but more detailed than the CG, qualitatively indicate the improvement to the surface layer resolution with the two-way nesting.

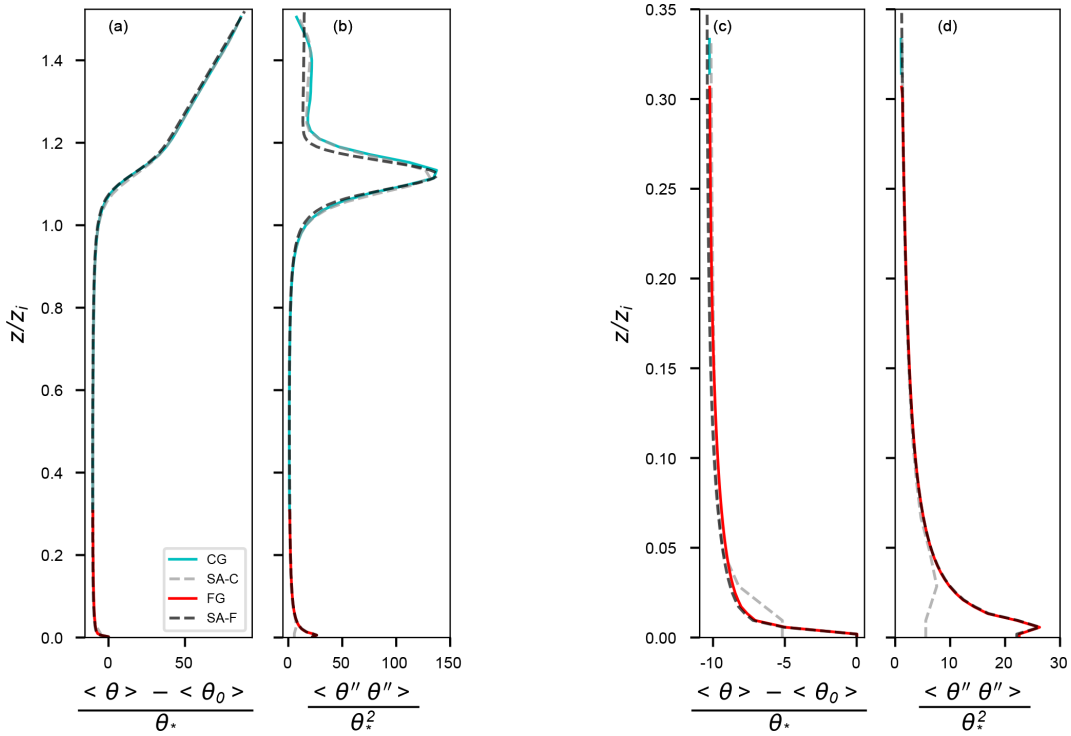

Figure 5. Vertical profile of horizontally averaged potential temperature normalized by the surface value **(a, c)** and variance of potential temperature normalized by θ_*^2 **(b, d)**. The nested grid profiles agree well with the SA-F in the surface layer. The improvement of the two-way nesting, at the boundary layer height, is seen in the good agreement in the profiles of CG and SA-F in **(b)**.

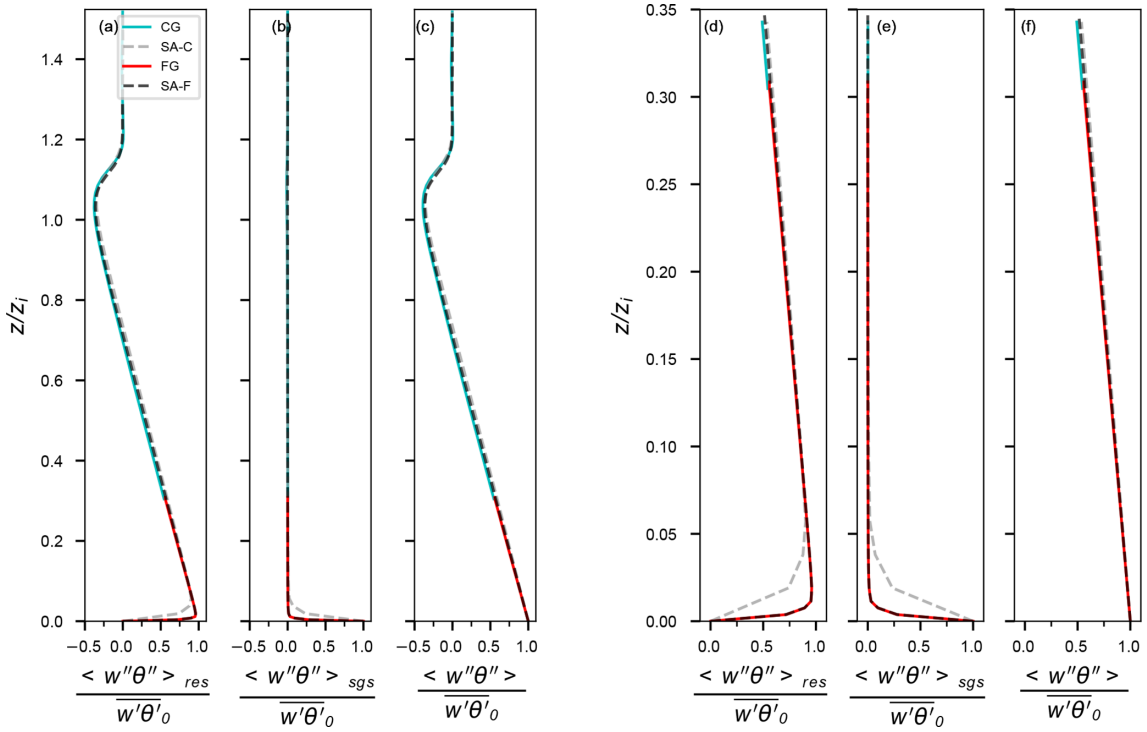

Figure 6. Vertical profile of horizontally averaged heat flux normalized by the surface heat flux – resolved **(a, d)**, sub-grid **(b, e)** and total flux **(c, f)**. The two-way nesting significantly improves the resolved and SGS fluxes in the surface layer.

Table 5. Grid configuration of the nested and non-nested FG domain.

	Nested					Non-nested FG		
Run	Total PE	CG PE	FG PE	Avg. time per step (s)	Efficiency (%)	Total PE	Avg. time per step (s)	Efficiency (%)
A	1664	64	1600	44.0	100	1600	14.9	100
B	3744	144	3600	19.9	98	3600	6.7	99
C	7488	288	7200	10.3	95	7200	3.6	92
D	8736	336	8400	9.3	90	8400	3.4	84
E	14 976	576	14 400	5.6	87	14 400	2.3	74

grid points, and such a large domain was computationally not feasible. The performance is measured in terms of the time taken to simulate one time step. To increase the accuracy of this performance measurement, the simulation is integrated for 10 time steps, and the average of the time per step is plotted. The results presented in Fig. 10 show close to linear scaling for up to 14 976 PEs in both nested and stand-alone runs. The difference in time per step between the nested and stand-alone runs can be interpreted as the additional computational time needed by the nesting algorithm. A jump in the time taken to compute one step is observed when more than 8192 PEs are used. This is a hardware-dependent increase in communication time as the nodes are grouped as "islands" on SuperMUC system at the Leibniz Supercomputing Centre. The communication within the nodes of the same island is faster than the communication across multiple islands. The strong scaling efficiency in Table 4 is calculated, keeping the run with the lowest number of PEs as the reference. As the number of grid points per PE is reduced from run A to E as shown in Table 5, the nested runs show slightly better efficiency than the non-nested runs. The average time per step of the nested grid is 3 times higher than the non-nested setup for run A, but the factor decreases to about 2.5 for run E. This improvement is possibly due to reduction in waiting time between the FG and CG as the number of grid points per PE decreases.

3.4 Practical considerations

In this paragraph we summarize some guidelines for using this nesting approach. In PALM, the user has the choice to

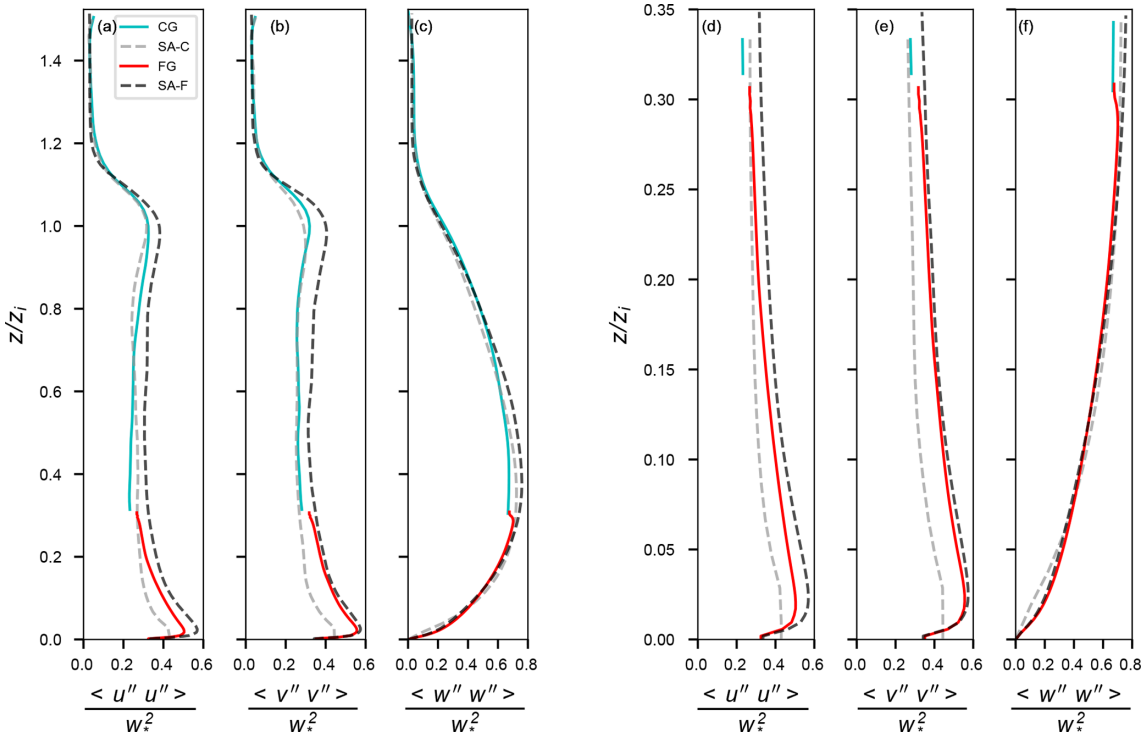

Figure 7. Vertical profile of horizontally averaged resolved variance of u **(a, d)**, v **(b, e)**, and w **(c, f)** normalized by w_*^2. The variance of v and w shows better agreement with the stand-alone reference in the surface layer.

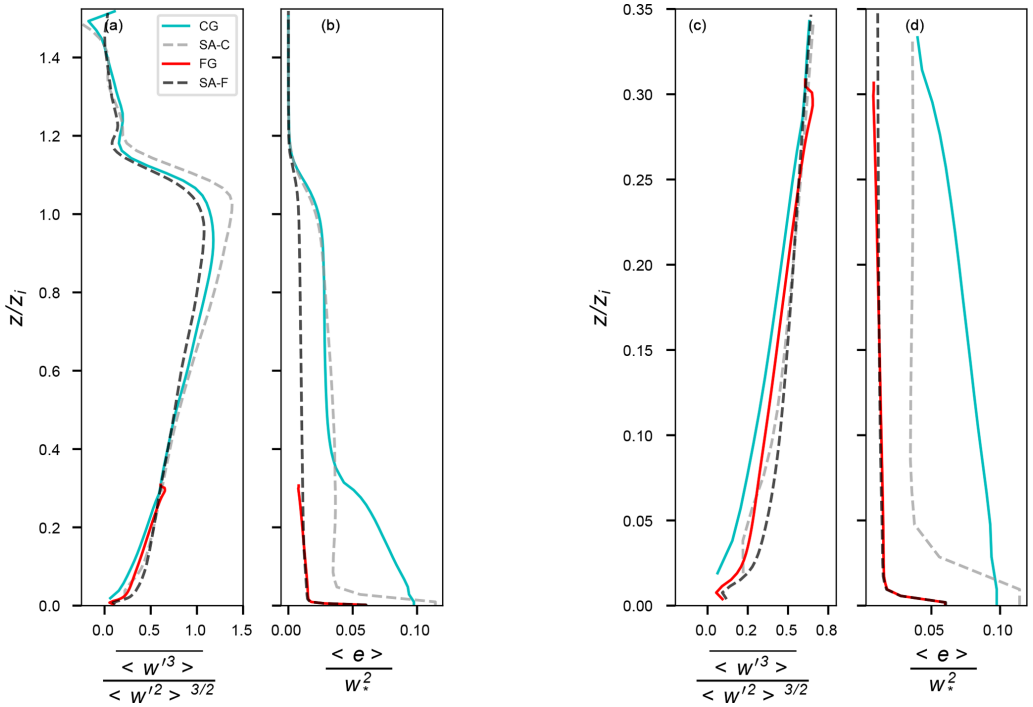

Figure 8. Vertical profile of horizontally averaged resolved vertical velocity skewness **(a, c)** and SGS turbulent kinetic energy e **(b, d)** normalized by w_*^2. The SGS TKE in the CG is higher than SA-C as a result of anterpolation maintaining the Germano identity.

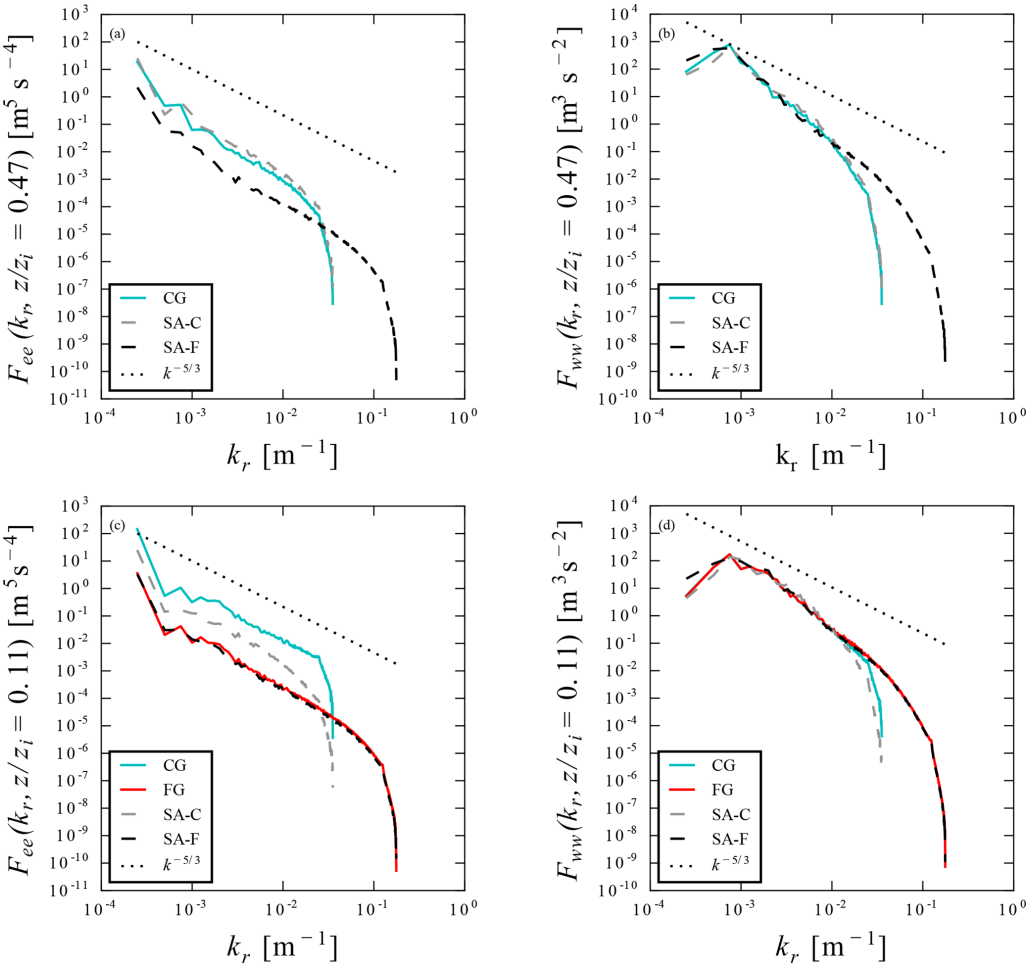

Figure 9. Spectra of SGS turbulent kinetic energy (e) **(a, c)** and vertical velocity (w) **(b, d)**. At $z/z_i = 0.47$ **(a, b)** and at $z/z_i = 0.11$ **(c, d)**, k_r is the horizontal wavenumber.

select between Wicker–Skamarock (Wicker and Skamarock, 2002) and Piacsek–Williams (Piacsek and Williams, 1970) for the advection scheme. Similarly, for solving the Poisson equation for the pressure, the user can choose between the FFT or multi-grid-based solver. During the development and the validation of the two-way nesting, only the Wicker–Skamarock advection scheme and FFT-based pressure solvers were tested. The two-way nesting supports only periodic boundary conditions in the horizontal for both CG and FG, and therefore an FFT-based pressure solver is an appropriate choice. However, to be able to use multi-grid solvers, e.g., in nonperiodic horizontal boundary conditions, modifications to the two-way nesting algorithm will be needed. The large-scale forcing feature in PALM is found to be compatible with the nesting algorithm without further modifications. Other features like canopy parameterization, radiation models and land surface models have not been tested.

Our implementation of the vertical nesting allows only integer nesting ratios in all directions. The height of the nested domain has a direct influence on the accuracy of the two-way nesting algorithm. Based on our trials (not shown) we recommend that the FG covers at least 12 grid levels of the CG. For better computational performance we recommend that the number of grid points per PE in the CG is kept at only 40 % to 80 % of the FG value. The reduced work load of the CG is expected to minimize the waiting time of the FG during the concurrent time advancement by the quicker CG pressure solver step. However, the actual improvement in performance will depend on the memory available, processor speed and the inter-node communication architecture of the computing cluster, and the optimal load balancing can only be found through trials. Furthermore, the choice of the domain size is often restricted by the topology of the processor decomposition. In a 2-D decomposition, the number of grid points along the x direction should be an integer multiple of the number of PEs along x and similarly for the y direction. This condition has to be individually satisfied for the CG and the FG. Though our nesting technique makes resolving the surface layer resolution down to 0.5 m for a moderately large

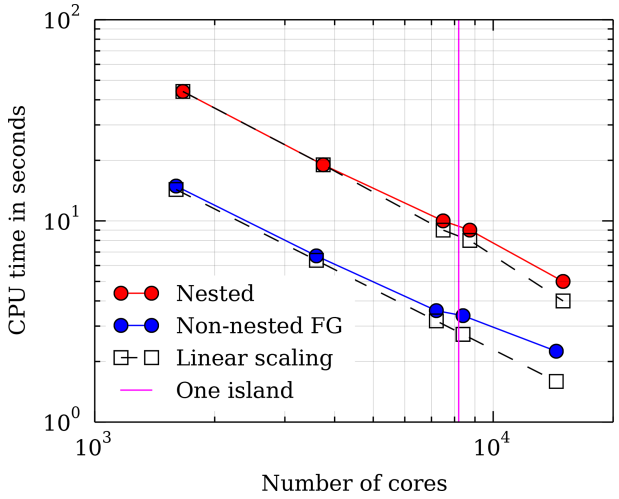

Figure 10. The nested simulations show close to linear scalability. A non-nested domain with same number of grid points as the FG is plotted to benchmark the scalability of the standard version of PALM on the same machine. The difference between the blue and the red line is approximately equal to the additional computational time needed by the nesting routines. The simulations were performed on SuperMUC at the Leibniz Supercomputing Centre. Each node has 32 GB of main memory and two Sandy Bridge processors with 2.7 GHz; each processor has eight cores (Anastopoulos et al., 2013).

domain computationally feasible, care should be taken to ensure the validity of such LES. In PALM, the height of the first grid point should be at the least twice greater than the local surface-roughness parameter. This technical restriction is common to all models that employ MOST and ensures the proper evaluation of the logarithm needed in the calculation of u^*. Furthermore, Basu and Lacser (2017) recently recommended that MOST boundary conditions should be adapted for very high resolution LES, where the first grid point is smaller than 2–5 times the height of the roughness elements.

4 Summary

We presented a two-way grid nesting technique that enables high-resolution LES of the surface layer. In our concurrently parallel algorithm, the two grids with different resolution overlap in the region close to the surface. The grids are coupled, i.e the interpolation of the boundary conditions and the feedback to the parent grid are performed, at every sub-step of the Runge–Kutta time integration. The anterpolation of the TKE involves the Germano identity to ensure the conservation of total kinetic energy. The exchange of data between the two grids is achieved by MPI communication routines, and the communication is optimized by derived data types. Results of the convective boundary layer simulation show that grid nesting improves the vertical profiles of variance and the fluxes in the surface layer. In particular, the profiles of the vertical temperature flux are improved. The current vertical nesting only works with periodic boundary conditions and with the same horizontal extent in both the domains. The nested simulation needs 4 times less computational time than a full high-resolution simulation for comparable accuracy in the surface layer. The scalability of the algorithm on up to 14 976 CPUs is demonstrated.

Code availability. The Parallelized Large-eddy simulation Model (PALM) is developed and maintained by the PALM group, Institute of Meteorology and Climatology, Leibniz University Hannover (Raasch and Schröter, 2001; Maronga et al., 2015). The code is distributed under the GNU General Public License. The code (revision 2712) is available at https://palm.muk.uni-hannover.de/trac/browser/palm?rev=2712 (last access: 24 June 2019).

Author contributions. SH was the main developer of the model code, with FDR as side developer, SR supporting the code development and MM, SR and FDR supervising the development. The experiment was designed by SH, FDR, SR and MM and carried out by SH, who also performed the validation. Visualization was done by SH and the original draft written by SH and FDR, with review and editing by SR and MM. MM was responsible for funding acquisition and administration.

Acknowledgements. This work was conducted within the Helmholtz Young Investigators Group “Capturing all relevant scales of biosphere-atmosphere exchange – the enigmatic energy balance closure problem”, which is funded by the Helmholtz Association through the President’s Initiative and Networking Fund and by KIT. Computer resources for this project have been provided by the Leibniz Supercomputing Centre under grant pr48la. We thank Gerald Steinfeld for sharing his original notes and code of a preliminary nesting method in PALM. We also thank Matthias Sühring and Farah Kanani-Sühring of the PALM group for their help in standardizing and porting the code, and we thank Michael Manhart for fruitful discussions.

Financial support. This research has been supported by the Helmholtz Association (grant no. VH-NG-843).

The article processing charges for this open-access publication were covered by a Research Centre of the Helmholtz Association.

Review statement. This paper was edited by Christoph Knote and reviewed by Lucas Harris and two anonymous referees.

References

Anastopoulos, N., Nikunen, P., and Weinberg, V.: Best Practice Guide – SuperMUC v1.0. PRACE – Partnership for Advanced Computing in Europe 2013, available at: http://www.prace-ri.eu/best-practice-guide-supermuc-html (last access: 24 June 2019), 2013.

Basu, S. and Lacser, A.: A Cautionary Note on the Use of Monin–Obukhov Similarity Theory in Very High-Resolution Large-Eddy Simulations, Bound.-Lay. Meteorol., 163, 351–355, https://doi.org/10.1007/s10546-016-0225-y, 2017.

Boersma, B. J., Kooper, M. N., Nieuwstadt, F. T. M., and Wesseling, P.: Local grid refinement in large-eddy simulations, J. Eng. Math., 32, 161–175, https://doi.org/10.1023/A:1004283921077, 1997.

Clark, T. L. and Farley, R. D.: Severe downslope windstorm calculations in two and three spatial dimensions using anelastic interactive grid nesting: A possible mechanism for gustiness, J. Atmos. Sci., 41, 329–350, https://doi.org/10.1175/1520-0469(1984)041<0329:SDWCIT>2.0.CO;2, 1984.

Clark, T. L. and Hall, W. D.: Multi-domain simulations of the time dependent Navier Stokes equation: Benchmark error analyses of nesting procedures, J. Comput. Phys., 92, 456–481, https://doi.org/10.1016/0021-9991(91)90218-A, 1991.

Daniels, M. H., Lundquist, K. A., Mirocha, J. D., Wiersema, D. J., and Chow, F. K.: A New Vertical Grid Nesting Capability in the Weather Research and Forecasting (WRF) Model, Mon. Weather Rev., 144, 3725–3747, https://doi.org/10.1175/mwr-d-16-0049.1, 2016.

Deardorff, J. W.: Three-dimensional numerical study of the height and the mean structure of a heated planetary boundary layer, Bound.-Lay. Meteorol., 7, 81–106, https://doi.org/10.1007/BF00224974, 1974.

Deardorff, J. W.: Stratocumulus-capped mixed layers derived from a three-dimensional model, Bound.-Lay. Meteorol., 18, 495–527, https://doi.org/10.1007/BF00119502, 1980.

Debreu, L., Marchesiello, P., Penven, P., and Cambon, L.: Two-way nesting in split-explicit ocean models: Algorithms, implementation and validation, Ocean Model., 49–50, 1–21, https://doi.org/10.1016/j.ocemod.2012.03.003, 2012.

Esau, I.: Indirect air–sea interactions simulated with a coupled turbulence-resolving model, Ocean Dynam., 64, 689–705, https://doi.org/10.1007/s10236-014-0712-y, 2014.

Flores, F., Garreaud, R., and Muñoz, R. C.: CFD simulations of turbulent buoyant atmospheric flows over complex geometry: Solver development in OpenFOAM, Comput. Fluids, 82, 1–13, https://doi.org/10.1016/j.compfluid.2013.04.029, 2013.

Germano, M., Piomelli, U., Moin, P., and Cabot, W. H.: A dynamic subgrid scale eddy viscosity model, Phys. Fluid A, 3, 1760–1765, https://doi.org/10.1063/1.857955, 1991.

Harris, L. M. and Durran, D. R.: An Idealized Comparison of One-Way and Two-Way Grid Nesting, Mon. Weather Rev., 138, 2174–2187, https://doi.org/10.1175/2010mwr3080.1, 2010.

Kato, C., Kaiho, M., and Manabe, A.: An Overset Finite-Element Large-Eddy Simulation Method With Applications to Turbomachinery and Aeroacoustics, J. Appl. Mech., 70, 32–43, https://doi.org/10.1115/1.1530637, 2003.

Khanna, S. and Brasseur, J. G.: Three-Dimensional Buoyancy- and Shear-Induced Local Structure of the Atmospheric Boundary Layer, J. Atmos. Sci., 55, 710–743, https://doi.org/10.1175/1520-0469(1998)055<0710:tdbasi>2.0.co;2, 1998.

Kravchenko, A., Moin, P., and Moser, R.: Zonal Embedded Grids for Numerical Simulations of Wall-Bounded Turbulent Flows, J. Comput. Phys., 127, 412–423, https://doi.org/10.1006/jcph.1996.0184, 1996.

Kröniger, K., De Roo, F., Brugger, P., Huq, S., Banerjee, T., Zinsser, J., Rotenberg, E., Yakir, D., Rohatyn, S., and Mauder, M.: Effect of Secondary Circulations on the Surface-Atmosphere Exchange of Energy at an Isolated Semi-arid Forest, Bound.-Lay. Meteorol., 169, 209–232, https://doi.org/10.1007/s10546-018-0370-6, 2018.

Kurihara, Y., Tripoli, G. J., and Bender, M. A.: Design of a Movable Nested-Mesh Primitive Equation Model, Mon. Weather Rev., 107, 239–249, https://doi.org/10.1175/1520-0493(1979)107<0239:doamnm>2.0.co;2, 1979.

Manhart, M.: A zonal grid algorithm for DNS of turbulent boundary layers, Comput. Fluids, 33, 435–461, https://doi.org/10.1016/S0045-7930(03)00061-6, 2004.

Maronga, B., Gryschka, M., Heinze, R., Hoffmann, F., Kanani-Sühring, F., Keck, M., Ketelsen, K., Letzel, M. O., Sühring, M., and Raasch, S.: The Parallelized Large-Eddy Simulation Model (PALM) version 4.0 for atmospheric and oceanic flows: model formulation, recent developments, and future perspectives, Geosci. Model Dev., 8, 2515–2551, https://doi.org/10.5194/gmd-8-2515-2015, 2015.

Moeng, C.-H. and Wyngaard, J. C.: Spectral analysis of large-eddy simulations of the convective boundary layer, J. Atmos. Sci., 45, 3573—3587, https://doi.org/10.1175/1520-0469(1988)045<3573:SAOLES>2.0.CO;2, 1988.

Moeng, C.-H., Dudhia, J., Klemp, J., and Sullivan, P.: Examining Two-Way Grid Nesting for Large Eddy Simulation of the PBL Using the WRF Model, Mon. Weather Rev., 135, 2295–2311, https://doi.org/10.1175/MWR3406.1, 2007.

Nakahashi, K., Togashi, F., and Sharov, D.: Intergrid-Boundary Definition Method for Overset Unstructured Grid Approach, AIAA J., 38, 2077–2084, https://doi.org/10.2514/2.869, 2000.

Patton, E. G., Sullivan, P. P., Shaw, R. H., Finnigan, J. J., and Weil, J. C.: Atmospheric Stability Influences on Coupled Boundary Layer and Canopy Turbulence, J. Atmos. Sci., 73, 1621–1647, https://doi.org/10.1175/jas-d-15-0068.1, 2016.

Piacsek, S. A. and Williams, G. P.: Conservation properties of convection difference schemes, J. Comput. Phys., 198, 500–616, https://doi.org/10.1016/0021-9991(70)90038-0, 1970.

Raasch, S. and Schröter, M.: PALM – A large-eddy simulation model performing on massively parallel computers, Meteorol. Z., 10, 363–372, https://doi.org/10.1127/0941-2948/2001/0010-0363, 2001.

Reynolds, W. C.: The potential and limitations of direct and large eddy simulations, in: Whither Turbulence? Turbulence at the Crossroads, edited by: Lumley, J. L., Springer Berlin Heidelberg, Berlin, Heidelberg, 313–343, https://doi.org/10.1007/3-540-52535-1_52, 1990.

Saiki, E. M., Moeng, C.-H., and Sullivan, P. P.: Large-eddy simulation of the stably stratified planetary boundary layer, Bound.-Lay. Meteorol., 95, 1–30, https://doi.org/10.1023/A:1002428223156, 2000.

Schmidt, H. and Schumann, U.: Coherent structure of the convective boundary layer derived from large-

eddy simulations, J. Fluid. Mech., 200, 511–562, https://doi.org/10.1017/S0022112089000753, 1989.

Skamarock, W., Klemp, J., Dudhia, J., Gill, D., Barker, D., Wang, W., Huang, X.-Y., and Duda, M.: A Description of the Advanced Research WRF Version 3, https://doi.org/10.5065/d68s4mvh, 2008.

Sullivan, P. P., McWilliams, J. C., and Moeng, C.-H.: A grid nesting method for large-eddy simulation of planetary boundary layer flows, Bound.-Lay. Meteorol., 80, 167–202, https://doi.org/10.1007/BF00119016, 1996.

van Hooft, J. A., Popinet, S., van Heerwaarden, C. C., van der Linden, S. J. A., de Roode, S. R., and van de Wiel, B. J. H.: Towards Adaptive Grids for Atmospheric Boundary-Layer Simulations, Bound.-Lay. Meteorol., 167, 421–443, https://doi.org/10.1007/s10546-018-0335-9, 2018.

Wang, G., Duchaine, F., Papadogiannis, D., Duran, I., Moreau, S., and Gicquel, L. Y.: An overset grid method for large eddy simulation of turbomachinery stages, J. Comput. Phys., 274, 333–355, https://doi.org/10.1016/j.jcp.2014.06.006, 2014.

Wicker, L. J. and Skamarock, W. C.: Time-splitting methods for elastic models using forward time schemes, Mon. Weather Rev., 130, 2008–2097, https://doi.org/10.1175/1520-0493(2002)130<2088:TSMFEM>2.0.CO;2, 2002.

Williamson, J. H.: Low-storage Runge-Kutta schemes, J. Comput. Phys., 35, 48–56, https://doi.org/10.1016/0021-9991(80)90033-9, 1980.

Zhou, B., Xue, M., and Zhu, K.: A Grid-Refinement-Based Approach for Modeling the Convective Boundary Layer in the Gray Zone: Algorithm Implementation and Testing, J. Atmos. Sci., 75, 1143—1161, https://doi.org/10.1175/jas-d-17-0346.1, 2018.

D. High-resolution ensemble LES energy balance closure study of the LITFASS-2003 campaign

Huq, S., De Roo, F., Sühring, M., Wanner, L., & Mauder, M. (2023). High-resolution ensemble LES energy balance closure study of the LITFASS-2003 campaign. Meteorologische Zeitschrift (under review).

Meteorol. Z. (Contrib. Atm. Sci.), Early Access DOI 10.1127/metz/20xx/xxxx

High-resolution ensemble LES energy balance closure study of the LITFASS-2003 campaign

SADIQ HUQ[1], FREDERIK DE ROO[1,4], MATTHIAS SÜHRING[3,6], LUISE WANNER[1,2], MATTHIAS MAUDER[1,2,5]*

[1]Institute of Meteorology and Climate Research, Atmospheric Environmental Research (IMK-IFU), Karlsruhe Institute of Technology (KIT), Garmisch-Partenkirchen, Germany
[2]Institute of Hydrology and Meteorology, TUD Dresden University of Technology, Tharandt, Germany
[3]Institute of Meteorology and Climatology, Leibniz University Hannover, Hanover, Germany
[4]Norwegian Meteorological Institute, Oslo, Norway
[5]Institute of Geography and Geoecology, Karlsruhe Institute of Technology, Karlsruhe, Germany
[6]Pecanode GmbH, Germany

(Manuscript received November 4, 2023; in revised form 0, xxxx; accepted 0, xxxx)

Abstract

The imbalance between the measured available energy and the sum of the turbulent fluxes lead to the energy balance closure problem. In spite of several experimental and modelling studies, the reasons for the lack of closure are not fully understood, particularly, in a heterogeneous terrain. The LITFASS-2003 campaign in Northeastern Germany was designed to develop and to assess different area-averaging strategies of the surface fluxes over a heterogeneous land surface. The micrometeorological measurements of the campaign were targeted at local fluxes over different types of land surface that are essential to study the energy balance closure problem for a complex land surface where the secondary circulations induced by surface heterogeneity are suspected to influence the surface energy budget imbalance. To assess the influence of the secondary circulations we perform large-eddy simulations of a 5.4 x 5.4 km^2 sub-region of the LITFASS area with a flat topography and composed mainly of agricultural land. The boundary conditions for the simulation domain is derived from the experimental data collected on 30 May 2003. To capture the spatial variation of the fluxes, the surface fluxes of latent and sensible heat flux in the simulated domain are prescribed by composite fluxes derived from multiple surface flux stations operated during the experiment. A grid resolution of 1 m in the vertical and 2 m in the horizontal directions up to 72 m from the ground is achieved by employing an LES-within-LES model. A total of five realizations of the domain is performed to calculate ensemble averages to separate the heterogeneity effect from the turbulence fluctuations and the 30-minute time averaging ensures more representative statistics. We find the underestimation to be systematic and to increase with height. At a typical eddy covariance tower height of 10 m, we find the dispersive flux represents up to 5% of the prescribed surface fluxes, which partially explains the imbalance in the field measurements.

Keywords: Convective boundary layer, Dispersive flux, Energy balance closure, Large-eddy simulation, Secondary circulation

1 Introduction

Several experimental studies on the biosphere-atmosphere exchange show that the surface energy balance is not closed at most measurement sites (WILSON et al., 2002; ONCLEY et al., 2007; FRANSSEN et al., 2010), i.e. the sum of the net radiation and the ground heat flux is not equal to the sum of the sensible and latent heat fluxes. Many reasons for this energy balance closure (EBC) problem are found in the literature, including instrumental errors, data processing errors and the lack of canopy heat storage terms. MAUDER et al. (2020) review the many potential reasons for surface energy imbalance and discuss the challenges associated with measuring the turbulent fluxes. More and more evidence points to the inability of single tower measurements to capture the sub-mesoscale transport, where turbulent fluxes are systematically underestimated in the presence of secondary circulations. There is sufficient evidence to show that the horizontal flux divergence and the advection terms are not negligible in many cases (MODEROW et al., 2006; DE ROO and MAUDER, 2018; WANNER et al., 2022; AKINLABI et al., 2022; ZHOU et al., 2023). A single tower measurement cannot capture the fluxes originating from a spatial covariation, so-called dispersive fluxes (RAUPACH and SHAW, 1982), therefore a spatially-resolving multi-tower analysis needs to be performed to include the energy associated with dispersive fluxes induced by secondary circulations, which manifest locally as horizontal flux divergence and advection terms, e.g. ENGELMANN and BERNHOFER (2016), MAUDER et al. (2008) and MARGAIRAZ et al. (2020).

The flow in the Atmospheric Boundary Layer (ABL) is generally turbulent. Therefore, high-frequency (> 10Hz) measurements are necessary to capture this transport and analysis based on localized measurements rely on the validity of Taylor's frozen turbulence assumption to quantify vertical fluxes (TAYLOR, 1938). However, in the presence of secondary circulations, which are a very common phenomenon during unstable stratification, this assumption is violated as these circulations are not propagated by the mean wind (MAHRT, 1998). A convenient computational technique to study the spatial variability of turbulence in the ABL, is large-eddy simulation (LES). LES resolves the turbulence above a grid-dependent cutoff scale, below which the turbulence becomes more generic and can be (statistically) predicted by simpler models (MASON, 1989). By this approach, the computational resources needed are reduced in comparison to direct numerical simulations, while an accurate representation of the turbulence above the cutoff scale can be achieved.

KANDA et al. (2004) were among the first to employ LES to study the EBC problem. Based on the virtual tower measurements in the dry simulation they showed that a single tower measurements systematically underestimate the turbulent fluxes. They use the term "turbulent organized structure" and described the local advection effects associated with this kind of secondary circulations that are not captured by single tower measurements. Interestingly, they noted that weak thermal surface inhomogeneity in surface heating may lead to an improved closure, while stronger inhomogeneity leads to a poorer closure. The LES study of STEINFELD et al. (2007) further emphasized the need for spatially distributed measurements to overcome the limitations of single eddy-covariance tower measurements. They found the imbalance to be smaller than 5% for observation heights < 20 m, and then increasing with height. However, the imbalance is often significantly higher for near-surface field measurements and can exceed 30%. According to INAGAKI et al. (2006), inhomogeneity in surface heating weakens turbulent organized structures (TOS) due to formation of thermally-induced mesoscale circulations (TMC) and at higher wind speeds, TOS are advected at sufficient speeds to maintain the validity of ergodicity assumption, which leads to a better EBC. HUANG et al. (2008) found a set of non-dimensional functions to describe the dependence of flux imbalance on u_*/w_* and z/z_i, where u_*, w_* and z_i are friction velocity, convective velocity and boundary layer height, respectively. They also investigated the effect of secondary circulations on the CO2 flux besides the fluxes of sensible and latent heat.

The EBC problem has also been investigated by dedicated experiments, the first one being the EBEX-2000 field campaign conducted in Central California (ONCLEY et al., 2007). This experiment was designed to quantify local advection amongst other possible explanations for an systematic bias in flux measurements. Hence, ten eddy-covariance towers were deployed over an area of approximated 1 km^2 over a cotton field, but this set-up was too small and homogeneous to measure significant advective fluxes. Another large-scale experiment with multiple eddy-covariance towers was the 'Lindenberg Inhomogeneous Terrain — Fluxes between Atmosphere and Surface:

a long-term Study' campaign in 2003 (LITFASS-2003) in Brandenburg, Germany, around the boundary-layer test site Falkenberg of the German Meteorological Service (DWD). A special focus of this campaign was on the effect of surface heterogeneity on turbulent transport processes in an area of 10 km x 10 km (BEYRICH and MENGELKAMP, 2006), and hence this experiment was also well-suited to study the EBC problem (FOKEN et al., 2010).

While previous studies on other sites (e.g. EDER et al., 2015) have already given indications for the reasons leading to a poor closure of the energy balance, using a combination of tower measurements and LES, these studies have been limited by the resolution of typically >10 m to capture the turbulent behaviour closer to the surface. We address this limitation with the aid of a vertically nested grid (HUQ et al., 2019) that allows us to achieve much higher grid spacing close to the surface while still maintaining a sufficiently large domain to capture the low frequency turbulent organized structures over this LITFASS-2003 landscape. MARONGA et al. (2014) noted that in their simulation and in the previous studies for this area of MARONGA and RAASCH (2013) and SÜHRING and RAASCH (2013) the fluxes from the single eddy-covariance stations were erroneously used to prescribe the lower boundary condition, which resulted in too strong surface fluxes. To overcome this issue, we use the composite fluxes derived from multiple energy balance stations over the same vegetation type as described in BEYRICH et al. (2006). Hence, the aim of this study is to investigate the influence of secondary circulations on the flux measurement and the related lack of energy balance closure. To this end we conduct a high-resolution LES study for a specific day of the LITFASS-2003 campaign by using vertical grid nesting. These simulations will be driven by the composite fluxes derived from field measurements over all relevant land-cover types in the study area. We perform ensemble runs to separate heterogeneity effect from the turbulence fluctuations. In addition, we employ time averaging to achieve more representative statistics of the virtual measurements.

In the following section, the LES tool and the simulation set-up are described along the data analysis steps. In Sect. 3 the results of the ensemble simulations are analysed both qualitatively and quantitatively. The influence of advection and flux divergence on the energy balance closure are then discussed in Sect. 4. Our findings are summarized along with recommendations for future analysis in Sect. 5.

2 Methods

2.1 The LES Model

The PArallelized Large-eddy simulation Model (PALM) version 4.0 is used in this study (RAASCH and SCHRÖTER, 2001; MARONGA et al., 2015). PALM discretises the non-hydrostatic incompressible Navier-Stokes equations in the Boussinesq approximation using the Finite Difference Method on a staggered Arakawa C grid (ARAKAWA and LAMB, 1977). Prognostic equations for the components of the velocity field (u,v,w), potential temperature (θ) and humidity (q) are solved. In addition, PALM solves an equation for the sub-grid scale kinetic energy (e). The 1.5-order sub-grid-scale turbulence model based on DEARDORFF (1980) assumes the gradient-diffusion parametrization modified by MOENG and WYNGAARD (1988) and SAIKI et al. (2000). The scalar and momentum advection terms are discretised by a fifth-order upwind scheme according to WICKER and SKAMAROCK (2002). The lower boundary condition for the horizontal momentum equation is derived from Monin-Obukhov similarity theory (MOST). The six prognostic equations are integrated in time using a third-order Runge-Kutta scheme (WILLIAMSON, 1980).

2.2 Set-up of high resolution vertically nested LES

The LITFASS-2003 experiment area encompasses several land-use classes each having different roughness characteristics and varying surface heat flux. A complete description of the experiment site and the instrumentation set-up is available in BEYRICH and MENGELKAMP (2006). We selected a 5.4 x 5.4 km^2 area such that the measurement station A4 (Maize), A5 (Triticale), A6 (Maize) and the tall tower station GM (Grass) are well within the simulation domain since especially A6 was equipped with additional and higher quality instrumentation to measure the entire

[ht]

Table 1: Grid configuration and simulation parameters

Simulation Parameters	Value
Parent domain size	5.4 x 5.4 x 2.2 km^3
Child grid vertical extent	72 m
Parent grid resolution (dx,dy,dz)	6 m, 6 m, 3 m
Child grid resolution (dx,dy,dz)	2 m, 2 m, 1 m
Surface heat flux, H_0	time-varying interpolated composite fluxes following BEYRICH et al. (2006) (Fig. 1c)
Surface humidity flux, LE_0	time-varying interpolated composite fluxes following BEYRICH et al. (2006) (Fig. 1d)
Geostrophic wind	$u_g = -2$ m s^{-1} (Easterly), $v_g = 0$ m s^{-1}
Roughness length	depending on vegetation type from CORINE dataset (Fig. 1b)
Density, ρ	1.204 Kg K^{-1}
Specific heat of air, C_p	1005 J Kg^{-1} K^{-1}
Latent heat of vaporization, L_v	$2.5 \cdot 10^6$ J Kg^{-1}
Simulated time	12600 s (10:30 UTC - 14:00 UTC)
Spin-up time	10800 s (13:30 UTC - 13:30 UTC)
Data capture and temporal-averaging interval	1800 s (13:30 UTC - 14:00 UTC)
Number of realizations for ensemble statistics	5

energy balance. We simulate a 3.5 hours period on the 30 May 2003 around noon, the local time is UTC+1. The chosen day was characterized by clear skies and weak Easterly geostrophic wind of 2 m s^{-1}. The former condition is ideal to avoid spatial variability in the incoming radiation and the weaker wind is still computationally feasible as higher wind speeds need smaller time steps. Considering the Easterly winds, the virtual towers are positioned at the Western side of the domain. The different land-use classes and the tower locations are shown in Fig. 1. The high resolution at the surface is made possible by vertical grid nesting, where a child grid at fine resolution sits within a parent grid at a coarser resolution. The coarse grid parent domain extends vertically up to 2212 m, the vertical resolution is kept constant at 3 m up to a height of 2000 m and thereafter the grid is stretched by a factor of 1.01. The vertical extent of the fine grid child domain is 72 m, the vertical grid resolution is kept constant at 1 m. The horizontal grid resolution of the coarse grid and the fine grid are 6 m and 2 m,respectively. This corresponds to a grid nesting ratio of 3 in both horizontal and vertical directions. The total number of grid points in the parent and child grid are 583.2 x 10^6 and 486.72 x 10^6, respectively. Such large number of grid points demanded a total 2592 CPUs for one simulation. One simulation needed approximately 1 million core hours. The simulation parameters and grid configuration are listed in Table 1. I

Periodic boundary conditions can be applied in the lateral dimensions as the horizontal extent of the parent and the child grid are identical. This allows the Poisson equation for pressure to be solved with a computationally efficient Fast Fourier Transform algorithm. The velocity at the bottom is set to Dirichlet condition corresponding to zero vertical and horizontal velocity. The vertical velocity at the top of the parent domain is zero and the horizontal velocity is equal to the geostrophic wind. For the scalar quantities potential temperature, humidity, turbulent kinetic energy and pressure we apply Neumann conditions at the bottom and at the top. The top boundary conditions for the child grid are interpolated from the parent grid (HUQ et al., 2019). In the employed two-way nesting approach the coarse grid is updated by "anterpolation" (feedback) from the fine grid after each time step.

The surface roughness for each land-use class is obtained from the Coordinated Information on the European Environment (CORINE) dataset, published by the European Environment Agency, modified by MARONGA and RAASCH (2013). However, the surface roughness of the forest had to be reduced from the original 1.5 m to 0.45 m to comply with the requirements of MOST where the surface roughness cannot be more than half the vertical grid spacing. The surface values of potential temperature, humidity, sensible heat flux and latent heat flux too vary depending on the land-use type. The surface fluxes available at 30-minute intervals were linearly interpolated in time during the duration of the simulation as shown in Fig. 1. A variable time step was allowed up to a spin-up phase of 3 hours where PALM computes a time step such that the Courant-Friedrichs-Lewy (CFL) condition is satisfied

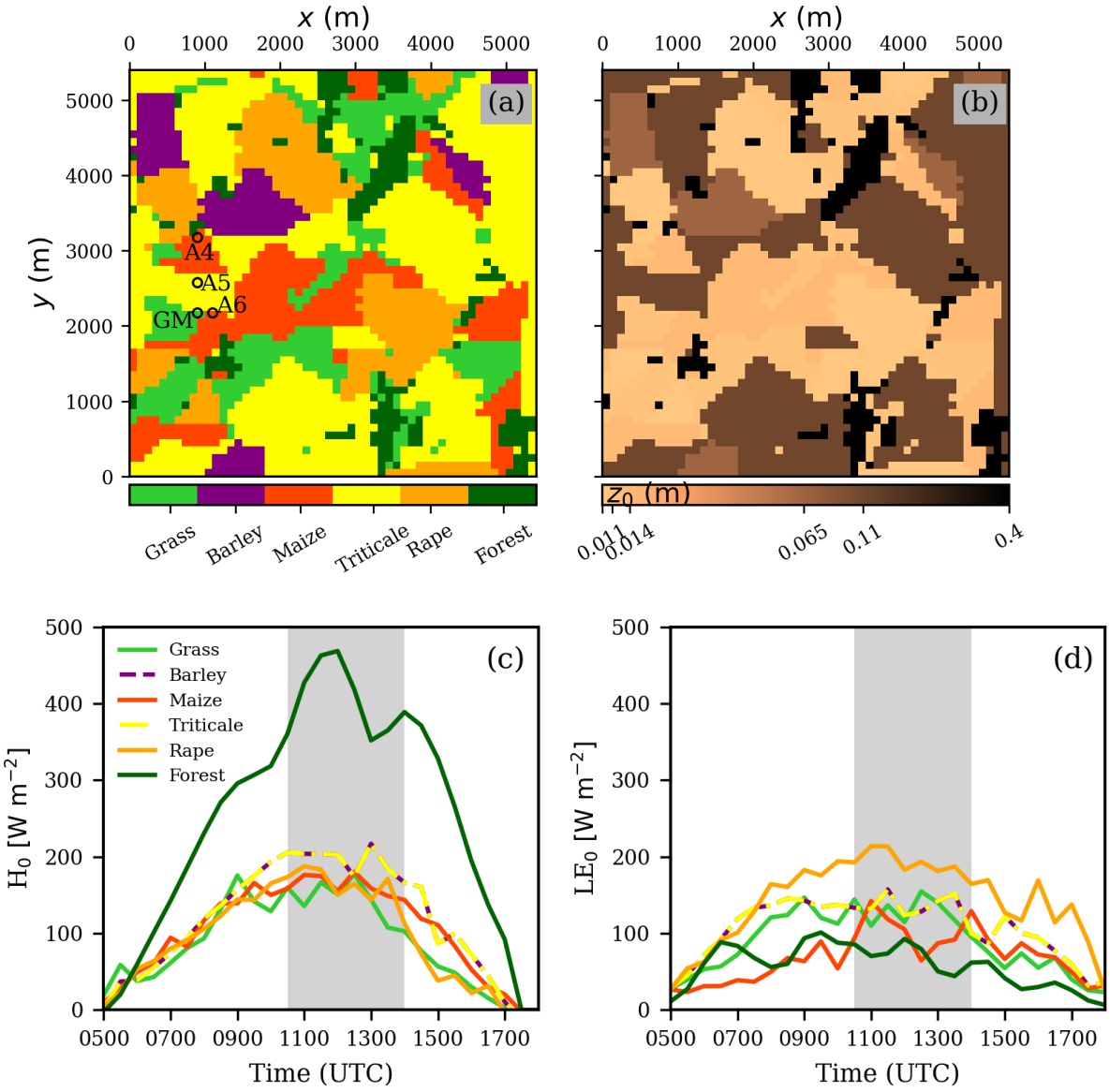

Figure 1: The vegetation classification derived from the CORINE dataset for the simulated area with the position of the virtual towers corresponding to the in-situ measurement towers indicated by labels A6, A4, GM and A5 (a) and surface roughness (b). The interpolated time series of composite fluxes of sensible (c) and latent (d) heat fluxes at the surface on 30 May 2003; the shaded portion indicates the period simulated in this study. Barley and Triticale are grouped together in composite flux calculation, however, the surface roughness of the two vegetation are not identical.

in both the grids. In the last 30 minutes of the simulation a conservative fixed time step of 0.05 s is prescribed. To perform ensemble analysis we repeat the simulation by adding an initial perturbation that is controlled by a random seed. The influence of numerical round-off errors on the ensemble statistics is prevented by compiling the model code with appropriate floating point operation flags to ensure that the simulation remains deterministic for the prescribed random seed. The five realizations of the domain are referred to as LIT-A, LIT-B, LIT-C, LIT-D and LIT-E in the following sections.

2.3 Data Post-Processing and Analysis

The energy balance ratio (EBR) represents the amount of simulated turbulent flux to the prescribed surface flux. In equation 2.1, w, θ and q are vertical velocity, potential temperature and humidity, respectively. The first term in the

numerator is the measured sensible heat flux and the second term is the latent heat flux. In the denominator, H_0 and L_0 represent the surface sensible and latent heat fluxes, respectively,

$$EBR = \frac{\rho \cdot C_p \cdot \overline{w'\theta'} + \rho \cdot L_v \cdot \overline{w'q'}}{H_0 + LE_0}; \tag{2.1}$$

where ρ, C_p and L_v are air density, specific heat of air and latent heat of vaporization, respectively. Since time-averaged turbulent flux was not a standard output in PALM 4.0, an user code was employed to calculate the total flux at each time step and only the time-averaged total flux is written at the end of each simulation. The term w"θ" represents the sub-grid scale flux and the overbar denotes time-averaging.

$$\overline{w\theta} = \overline{w \cdot \theta + w"\theta"}. \tag{2.2}$$

The sensible heat flux can then be calculated from the total flux, $\overline{w}$ and $\overline{\theta}$ as

$$\overline{w'\theta'} = \overline{w\theta} - \overline{w} \cdot \overline{\theta}. \tag{2.3}$$

The dispersive sensible flux (H_{disp}) can then be computed as,

$$\langle \overline{w^*}\,\overline{\theta^*} \rangle = \langle (\overline{w} - \langle \overline{w} \rangle) \cdot \left(\overline{\theta} - \langle \overline{\theta} \rangle\right) \rangle; \tag{2.4}$$

where the angle brackets indicate horizontal spatial mean and the asterisk indicates deviation from the spatial mean. Similarly, the vertical latent heat fluxes and dispersive latent heat fluxes (LE_{disp}) are calculated by replacing θ with specific humidity, q in Eqs. 2.3 and 2.4. The ensemble fluxes are computed as arithmetic mean of the member runs (Eqs. 2.5 and 2.6) and the kinematic vertical fluxes are convert to dynamic fluxes,

$$H_{ens} = \rho \cdot C_p \cdot \frac{1}{N} \sum_{i=1}^{N} \overline{w'\theta'}_i, \tag{2.5}$$

$$LE_{ens} = \rho \cdot L_v \cdot \frac{1}{N} \sum_{i=1}^{N} \overline{w'q'}_i. \tag{2.6}$$

The ensemble EBR (Eq. 2.7) too is computed as arithmetic mean since the 30-min averaged surface flux in the denominator of equation 2.1 is identical in all the runs.

$$EBR_{ens} = \frac{1}{N} \sum_{i=1}^{N} EBR_i. \tag{2.7}$$

3 Results

We present a brief qualitative analysis before presenting the statistical analysis of the simulations in order to demonstrate the plausibility of the simulations. All the results presented in this section are time averaged over the last 30 minutes of the simulated period. All results are obtained from the nested child grid unless stated otherwise. The vertical velocity contours of an XZ-plane cutting across the A6 site are shown in Fig. 2. There are noticeable

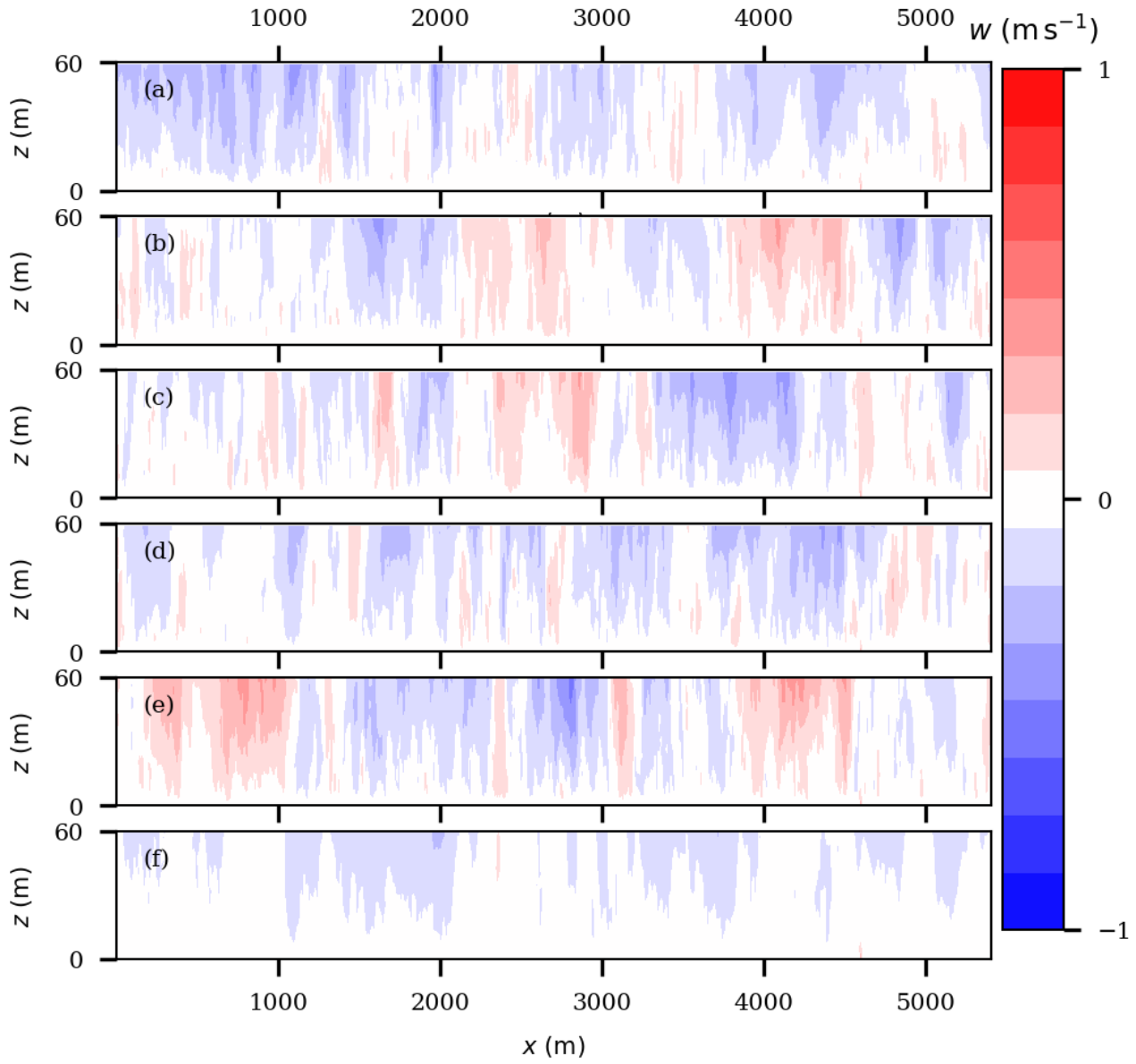

Figure 2: The time-averaged vertical velocity of the XZ plane cross-section cutting across the A6 measurement site. Panels from top to bottom correspond to realizations LIT-A, LIT-B, LIT-C, LIT-D, LIT-E and the ensemble averaged w of the five realizations, respectively. Persistent secondary circulation are present even after temporal and ensemble averaging.

differences in the up and down drafts patterns between the multiple realizations even after time averaging. The bottom plot indicates the presence of persistent secondary circulations that do not disappear even after ensemble averaging.

The velocity vector plotted at a height of 10 m and coloured by the velocity magnitude in Fig. 3 (a) shows the vectors are predominantly oriented in the direction of the mean wind but with noticeable areas of convergence and divergence. Particularly, in the northern section of the domain we observe convergence zone characterized by low velocity magnitude that is typical of a roll like structure. A similar convergence zone is also noticeable in the region close to the A6 towers. The magnitude of vorticity visualized in Fig. 3 (b) is high in the regions with high surface roughness. This is more noticeable in the north-east corner of the domain where the high vorticity can be interpreted as forest edge-effect.

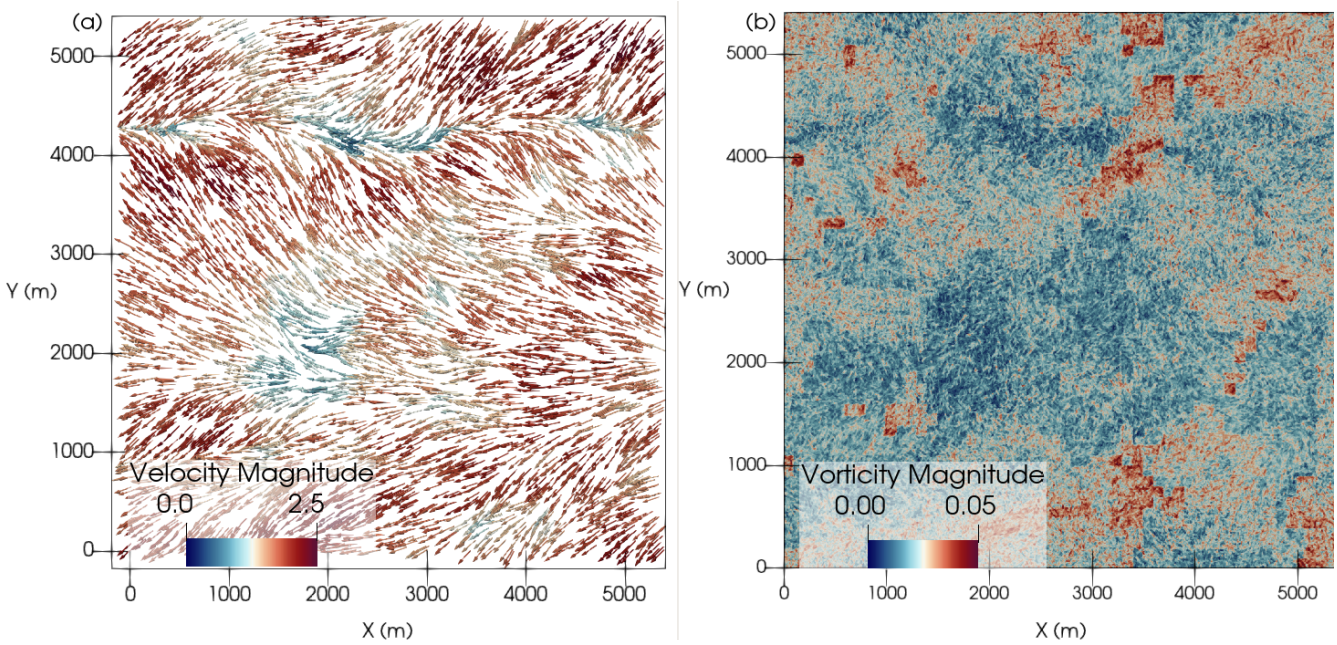

Figure 3: The time-averaged three-dimensional velocity vector of a horizontal slice at 10 m height coloured by the velocity magnitude (a). The convergence zone characterized by low velocity magnitude, in the northern section, is typical of a roll like structure. The vorticity magnitude (b) visualized at the same slice; higher magnitudes are observed at areas with higher surface roughness. Both (a) and (b) are parent grid output of one realization – LIT-C.

The sensible heat flux, latent heat flux and energy balance ratio at a height of 10 m are shown in Fig. 4 for an arbitrary realization LIT-C and for the ensemble of all realizations. The sensible and latent heat flux at the horizontal slice show the surface heterogeneity has an influence on the turbulent fluxes at 10 m height for both LIT-C and the ensemble fluxes. The ensemble EBR clearly shows areas of over and under closure. Particularly, the edge effects of different land-use classes are more pronounced. On the contrary, the realization LIT-C in Fig. 4(c) shows no obvious pattern though some areas of overclosure, underclosure and regions of ideal closure are distributed throughout the horizontal slice. As annotated in Fig. 4 (f) the horizontally averaged EBR of the ensemble domain at 10 m is 0.97. Interestingly, the horizontally averaged EBR of LIT-C and the ensemble remains the same even as the observed pattern is considerably different.

The spatial variability of the fluxes and the energy balance ratio are visualized with the help of Probability Density Function (PDF) of the ensemble in Fig. 5. The PDF for different levels show that the vertical fluxes decreases with height and the median lies below one in all cases. The EBR PDFs have similar shape as those for the sensible heat flux. The tails of PDFs to the left indicate that the underclosure is systematic with strong dependence on the height. Whereas the tail on the right show that the overclosure is not systematic and not dependent on the height. However, the tails of the latent heat flux PDFs show dependence with height both above and below one.

Dispersive fluxes, which represent the vertical transport by secondary circulations, normalized by the surface flux (Fig. 6) indicate that both H_{disp} and LE_{disp} increase with height for all ensemble members. However, the increase of LE_{disp} is stronger than that of H_{disp} and stays stronger over longer vertical distance. But such increase with height is not observed in the humidity profile (data not shown). The slope of the time-averaged humidity profile was found to be similar to the potential temperature profile.

The ensemble-averaged vertical profiles of sensible and latent heat flux at A6, A4, GM and A5 sites are shown in Fig. 7 (a,b,c and d) and the vertical profiles of EBR are shown in 7 (e,f,g and h), respectively. The results of the bottom 5 m of the simulation are not shown as MOST dominates in the first few grid points. At all sites sensible heat flux is greater than the latent heat flux. The turbulent flux profile at the A6 feature considerable differences

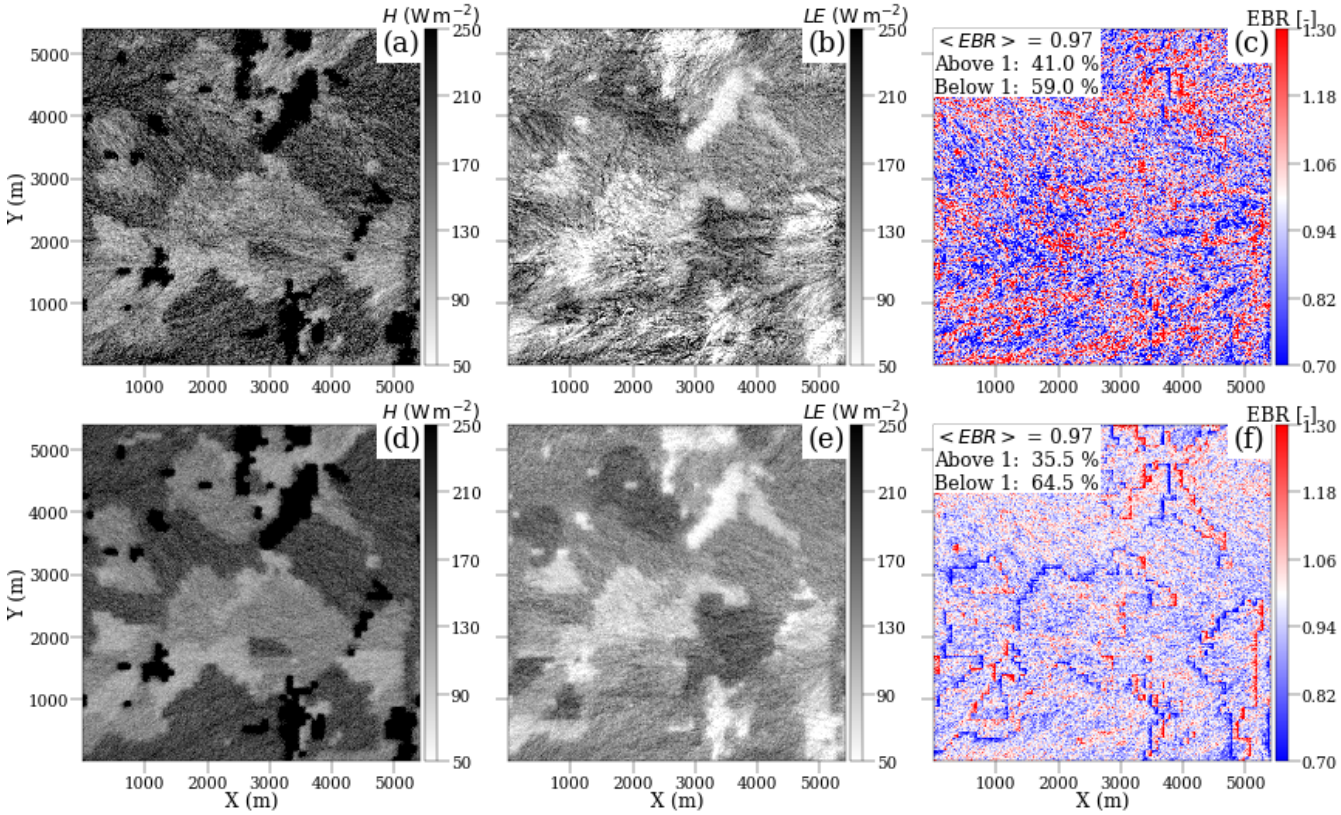

Figure 4: Time-averaged sensible heat flux, latent heat flux and EBR at a height of 10 m; for one realization LIT-C (top) and for the ensemble average of realizations (bottom). Areas of under- and overestimation near the edge of land-use classes are pronounced in ensemble EBR (f).

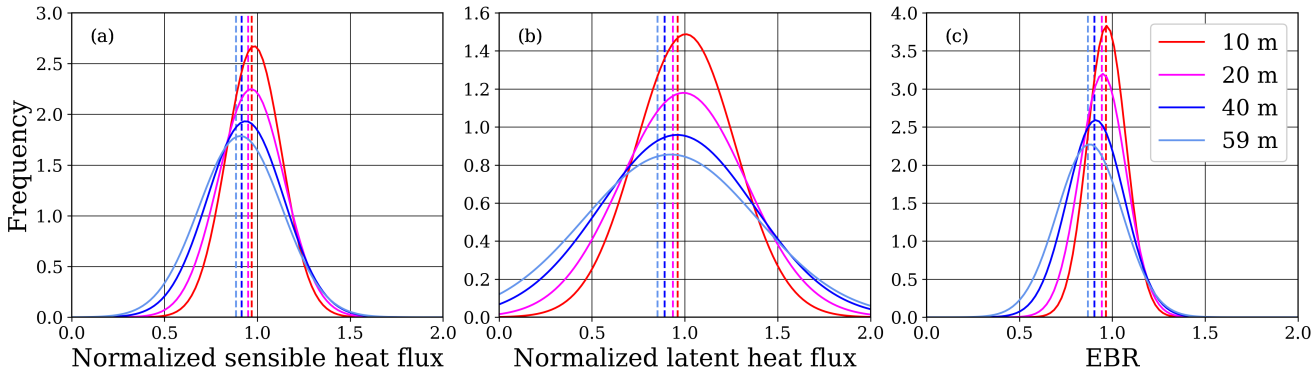

Figure 5: Probability density function at different height levels describing the horizontal variability of the ensemble-averaged sensible heat flux (a) and latent heat flux (b), normalized by the respective surface flux. The probability density function of the ensemble-averaged EBR is shown in (c). The median (dashed lines) is below one in all cases. The left tail and peak of PDF (c) shows underestimation is systematic with dependence on height.

compared to GM even though both sites are only a few meters apart. These differences are also noticeable in the EBR, while A6 has a slight overclosure, underclosure dominates above 20 m at the GM site.

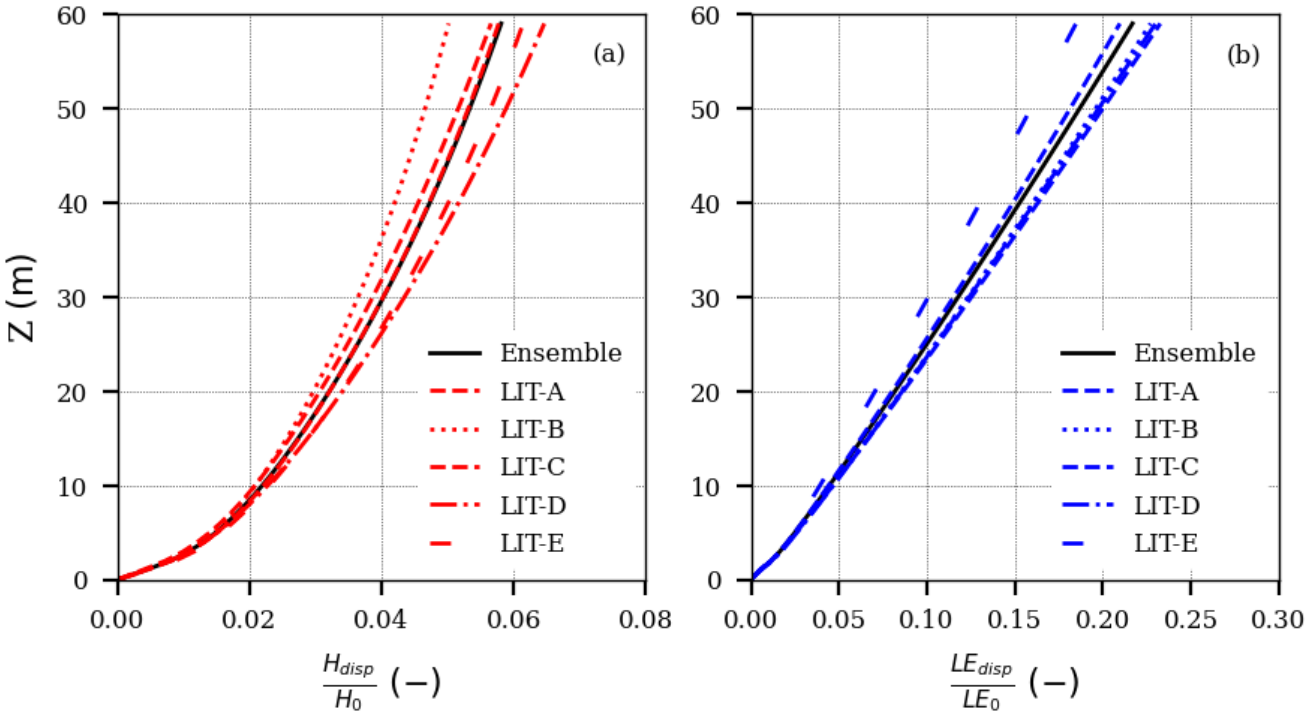

Figure 6: Dispersive sensible (a) and latent (b) heat fluxes normalized by surface fluxes. Both H_{disp} and LE_{disp} increase with height for all realizations but LE_{disp} shows stronger increase with height.

4 Discussion

It is pertinent to discuss the general limitations of the large-eddy simulations before interpreting the results. The primary limitations arises at the lower boundary where MOST is widely used in all atmospheric models including majority of the LES models. A detailed discussion on the applicability and limitation of MOST can be found in Foken (2006), Basu and Lacser (2017), Maronga et al. (2020) and Stiperski and Calaf (2023). Since the turbulence in the near-wall region is parametrised we avoid discussing the results in lowest grid levels. We focus our discussion at 10 m, a typical measurement height of the EC towers. The second limitation in LES studies is the grid resolution while the vertical resolution is crucial the aspect ratio should also not be compromised. Previous LES studies on Energy Balance Closure have been restricted by the vertical grid resolution preventing the visualization of the structures near the surface layer (De Roo et al., 2018). Our simulation with 1 m and 2 m resolution in the vertical and horizontal directions, respectively, makes it computationally feasible without compromising on low aspect ratio that is ideally needed by the isotropic subgrid model. The vector field in Fig. 3 (a) qualitatively shows the turbulence structures resolved at 10 m made possible by increased resolution. The peak boundary layer height (Z_i) observed in our simulation is 1250 m. This is lower than the 1800 m Z_i observed by Maronga and Raasch (2013) for same time of the day. The lower Z_i in our simulation could be partially due to the use of composite fluxes which are not as strong as the tower fluxes used by Maronga and Raasch (2013).

Another limitation often overlooked is the need for multiple realizations of the simulation domain. The spread of the ensemble member noticeable in Fig. 6 is a clear indication that one realization of the domain is not sufficient. Ensemble statistics calculated from multiple realizations provide better confidence. While higher number of realizations provide better statistics we have to acknowledge the computational resource limitations in achieving ideal statistics. Furthermore, in Fig. 2 we see the structures formed by the updrafts and downdrafts extending down to the surface layer even after 30-min averaging in all runs. The structures are also noticeable even in the ensemble contour supporting the prevalent hypothesis of the secondary circulation as the cause of the energy balance closure

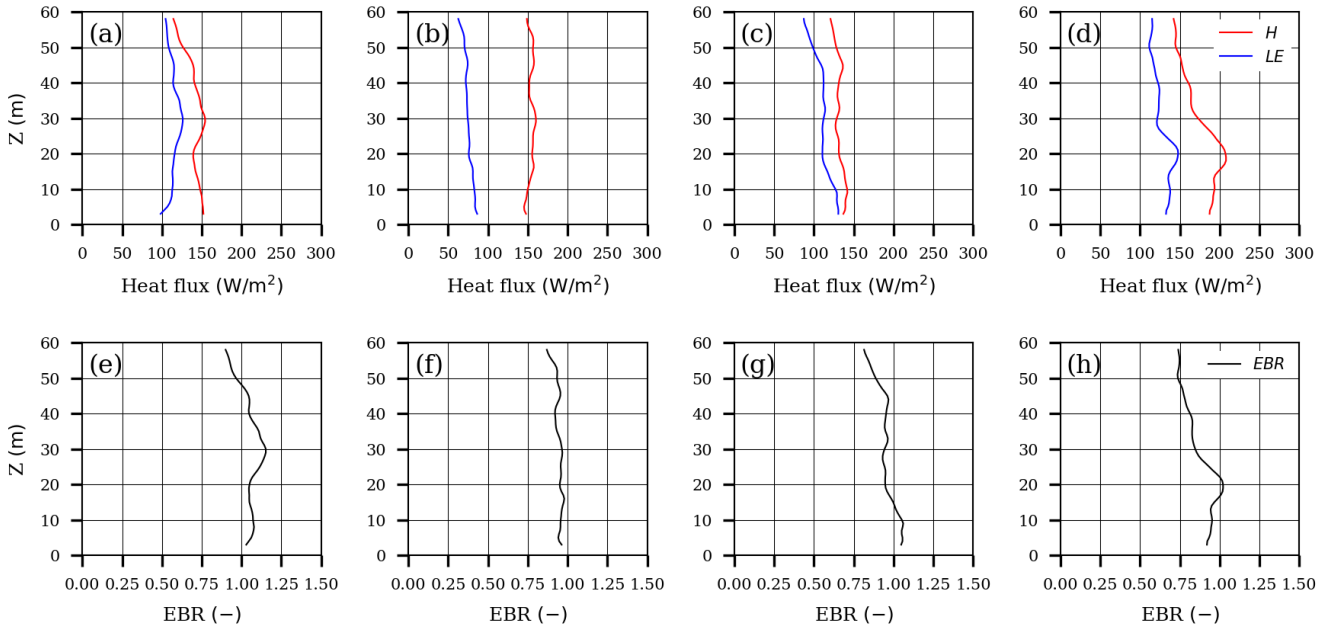

Figure 7: Time-averaged and ensemble-averaged vertical profile of turbulent heat fluxes (top) and EBR (bottom); from left to right for sites A6 (Maize), A4 (Maize), GM (Grass) and A5 (Triticale). In all cases, *H* is greater than *LE*. There are noticeable differences between A6 and GM even though the virtual towers are only a few meters apart.

problem as the single-tower EC systems cannot capture these persistent circulations. The spatial plots of sensible and latent heat fluxes at a height of 10 m, in Fig. 4a and Fig. 4b, shows that the fluxes correlate with the surface heterogeneity even at this height. This is in accordance with MARONGA and RAASCH (2013) were they investigated the influence of the blending height for the same day as in this study. The pattern of the fluxes still appears noisy; this is because the turbulent fluctuations that superimpose the mean fluxes have not vanished even after 30-min time averaging. In comparison, the fluxes of Fig. 4d and Fig. 4e are less noisy as the ensemble averaging has removed some of the fluctuations that still remained after time averaging. The effect of the ensemble average is evident in Fig. 4f where the EBR clearly shows the edge-effects in the areas where there is change in surface heterogeneity.

In Fig. 6, the calculated dispersive fluxes at 10 m height account for 2% and 5% of the sensible and latent heat flux at the surface, respectively. None of the previously conducted LES studies on the EBC problem found any significant underestimation at that height due to their limited grid resolution. Nevertheless, this range is still much smaller than the imbalance of the actual field measurements. This discrepancy could either mean that the grid resolution of our simulation is still not sufficient or that the imbalance from the field measurements has also other reasons than transport by secondary circulations, e.g. neglected storage terms (heat or biochemical), instrumental biases, mismatch of flux footprints etc. , which can alter the magnitude of the energy balance residual. Additionally, LES using prescribed fluxes, as in this study, cannot capture the feedback between secondary circulation and the surface temperature via convergence and divergence zones. A coupled land-surface model should be employed to include such second-order effects. In most of our virtual tower measurements, the imbalance increases with height, which is in accordance with previous studies and with our understanding of the underlying process of secondary circulations that weaken in intensity towards the ground.

Regarding the partitioning of the residual, DE ROO et al. (2018) found larger underestimation of sensible heat flux than the latent heat flux in the surface layer in an idealized simulation of homogeneous terrain. While we are unable to fully explain the reason for higher dispersive flux of latent heat, we suspect that entrainment of dry air could be a factor causing a different response to secondary circulations in comparison to the transport of sensible heat. The studies of MARONGA and RAASCH (2013) and UHLENBROCK et al. (2004) also found a greater

contribution of the mesoscale fluxes to the latent heat flux for the same LITFASS-2003 experiment. EDER et al. (2014) report equal partitioning of the mesoscale energy transport between the sensible and the latent hear flux for heterogeneous landscape in Canada. Therefore, it seems that this behaviour depends on the specific distribution of land-cover types and perhaps also on the meteorological conditions.

5 Conclusions

We presented a high-resolution LES designed and analysed to study energy balance closure in a heterogeneous farmland-dominated landscape. We chose the LITFASS-2003 experiment to conduct these simulations because of the wealth of observations and LES studies previously conducted for the same study area. This allows us to compare our results with a consolidated set of different kinds of data. We isolated heterogeneity effects from the turbulence fluctuations by calculating ensemble averages. Consistent with some previous studies we found evidence to support secondary circulations to be a significant cause of the lack of closure observed in field campaigns, as the associated vertical transport cannot be measured by EC towers. In contrast to previously published studies, we have investigated the effect of these circulations on virtual EC measurements with an unprecedented vertical resolution of 1 m in the vertical and 2 m in the horizontal direction, which allows for more a realistic representation of characteristic features of the turbulent flow near the surface.

The calculated ensemble of the dispersive fluxes show that this otherwise often neglected vertical transport increases with height and at a height of 10 m they account for up to 5% of the prescribed surface fluxes of sensible and latent heat. While this is an evidence of energy that cannot be measured by approaches assuming Taylor's frozen hypothesis, such as single-tower EC, the magnitude of this systematic bias is still low compared to the total imbalance at many sites, which is on the order of 15% on average (FOKEN et al., 2010; STOY et al., 2013). We also found evidence to support the notion that the underclosure occurs more frequently than overclosure with a strong dependence on the height. The underclosure increases to a value of up to 15% for a height of 60 m.

Future studies designed to study the energy balance closure problem should aim to achieve even higher resolution to fully understand the full contribution of the dispersive fluxes to the imbalance. A land-surface model should be employed at the lower boundary condition to allow for potential feedbacks between secondary circulations and surface fluxes. It is also essential to consider the other terms like storage and local advection that are not included in our analysis. A control volume approach, as used by DE ROO and MAUDER (2018) and EDER et al. (2015), may provide more insight on the energy partitioning. Lastly, flux footprint analyses may lead to a better comparison of the virtual measurements with the turbulence measured in the field.

Acknowledgements

This work was conducted within the Helmholtz Young Investigators Group "Capturing all relevant scales of biosphere-atmosphere exchange – the enigmatic energy balance closure problem", which is funded by the Helmholtz-Association through the President's Initiative and Networking Fund, and by KIT. Computer resources for this project have been provided by the Leibniz Supercomputing Centre under grant: pr48la. We also gratefully acknowledge Frank Beyrich (German Meteorological Service) for suggestions on a previous version of this manuscript.

References

AKINLABI, E., B. MARONGA, M.G. GIOMETTO, D. LI, 2022: Dispersive fluxes within and over a real urban canopy: A large-eddy simulation study. – Boundary-Layer Meteorology (1), 93–128, DOI: 10.1007/s10546-022-00725-6.

ARAKAWA, A., V.R. LAMB, 1977: Computational design of the basic dynamical processes of the UCLA general circulation model. – In: Methods in Computational Physics: Advances in Research and Applications, Elsevier, 173–265, DOI: 10.1016/b978-0-12-460817-7.50009-4.

BASU, S., A. LACSER, 2017: A cautionary note on the use of monin–obukhov similarity theory in very high-resolution large-eddy simulations. – Boundary-Layer Meteorology (2), 351–355, DOI: 10.1007/s10546-016-0225-y.

BEYRICH, F., H.T. MENGELKAMP, 2006: Evaporation over a heterogeneous land surface: EVA_GRIPS and the LITFASS-2003 experiment—an overview. – Boundary-Layer Meteorology **121**, 5–32, DOI: 10.1007/s10546-006-9079-z.

BEYRICH, F., J.P. LEPS, M. MAUDER, J. BANGE, T. FOKEN, S. HUNEKE, H. LOHSE, A. LÜDI, W.M.L. MEIJNINGER, D. MIRONOV, U. WEISENSEE, P. ZITTEL, 2006: Area-averaged surface fluxes over the litfass region based on eddy-covariance measurements. – Boundary-Layer Meteorology (1), 33–65, DOI: 10.1007/s10546-006-9052-x.

DE ROO, F., M. MAUDER, 2018: The influence of idealized surface heterogeneity on virtual turbulent flux measurements. – Atmospheric Chemistry and Physics (7), 5059–5074, DOI: 10.5194/acp-18-5059-2018.

DE ROO, F., S. ZHANG, S. HUQ, M. MAUDER, 2018: A semi-empirical model of the energy balance closure in the surface layer. – PLOS ONE (12), e0209022, DOI: 10.1371/journal.pone.0209022.

DEARDORFF, J.W., 1980: Stratocumulus-capped mixed layers derived from a three-dimensional model. – Bound.-Lay. Meteorol. **18**, 495–527, DOI: 10.1007/BF00119502.

EDER, F., M. SCHMIDT, T. DAMIAN, K. TRÄUMNER, M. MAUDER, 2015: Mesoscale eddies affect near-surface turbulent exchange: Evidence from lidar and tower measurements. – Journal of Applied Meteorology and Climatology **54**, 189–206, DOI: 10.1175/jamc-d-14-0140.1.

EDER, F., F.D. ROO, K. KOHNERT, R.L. DESJARDINS, H.P. SCHMID, M. MAUDER, 2014: Evaluation of two energy balance closure parametrizations. – Boundary-Layer Meteorology (2), 195–219, DOI: 10.1007/s10546-013-9904-0.

ENGELMANN, C., C. BERNHOFER, 2016: Exploring eddy-covariance measurements using a spatial approach: The eddy matrix. – Boundary-Layer Meteorology **161**, 1–17, DOI: 10.1007/s10546-016-0161-x.

FRANSSEN, H.H., R. STÖCKLI, I. LEHNER, E. ROTENBERG, S. SENEVIRATNE, 2010: Energy balance closure of eddy-covariance data: A multisite analysis for european FLUXNET stations. – Agricultural and Forest Meteorology (12), 1553–1567, DOI: 10.1016/j.agrformet.2010.08.005.

FOKEN, T., 2006: 50 years of the monin–obukhov similarity theory. – Boundary-Layer Meteorology (3), 431–447, DOI: 10.1007/s10546-006-9048-6.

FOKEN, T., M. MAUDER, C. LIEBETHAL, F. WIMMER, F. BEYRICH, J.P. LEPS, S. RAASCH, H.A.R. DEBRUIN, W.M.L. MEIJNINGER, J. BANGE, 2010: Energy balance closure for the LITFASS-2003 experiment. – Theoretical and Applied Climatology (1-2), 149–160, DOI: 10.1007/s00704-009-0216-8.

HUANG, J., X. LEE, E.G. PATTON, 2008: A modelling study of flux imbalance and the influence of entrainment in the convective boundary layer. – Boundary-Layer Meteorology (2), 273–292, DOI: 10.1007/s10546-007-9254-x.

HUQ, S., F. DE ROO, S. RAASCH, M. MAUDER, 2019: Vertically nested LES for high-resolution simulation of the surface layer in PALM (version 5.0). – Geoscientific Model Development **12**, 2523–2538, DOI: 10.5194/gmd-12-2523-2019.

INAGAKI, A., M.O. LETZEL, S. RAASCH, M. KANDA, 2006: Impact of surface heterogeneity on energy imbalance: A study using LES. – Journal of the Meteorological Society of Japan **84**, 187–198, DOI: 10.2151/jmsj.84.187.

KANDA, M., A. INAGAKI, M.O. LETZEL, S. RAASCH, T. WATANABE, 2004: LES study of the energy imbalance problem with eddy covariance fluxes. – Boundary-Layer Meteorology **110**, 381–404, DOI: 10.1023/b:boun.0000007225.45548.7a.

MAHRT, L., 1998: Flux sampling errors for aircraft and towers. – Journal of Atmospheric and Oceanic Technology (2), 416–429, DOI: 10.1175/1520-0426(1998)015<0416:fsefaa>2.0.co;2.

MARGAIRAZ, F., E.R. PARDYJAK, M. CALAF, 2020: Surface thermal heterogeneities and the atmospheric boundary layer: The relevance of dispersive fluxes. – Boundary-Layer Meteorology (3), 369–395, DOI: 10.1007/s10546-020-00509-w.

MARONGA, B., S. RAASCH, 2013: Large-eddy simulations of surface heterogeneity effects on the convective boundary layer during the LITFASS-2003 experiment. – Boundary-Layer Meteorology **146**, 17–44, DOI: 10.1007/s10546-012-9748-z.

MARONGA, B., O.K. HARTOGENSIS, S. RAASCH, F. BEYRICH, 2014: The effect of surface heterogeneity on the structure parameters of temperature and specific humidity: A large-eddy simulation case study for the LITFASS-2003 experiment. – Boundary-Layer Meteorology **153**, 441–470, DOI: 10.1007/s10546-014-9955-x.

MARONGA, B., M. GRYSCHKA, R. HEINZE, F. HOFFMANN, F. KANANI-SÜHRING, M. KECK, K. KETELSEN, M.O. LETZEL, M. SÜHRING, S. RAASCH, 2015: The parallelized large-eddy simulation model (palm) version 4.0 for atmospheric and oceanic flows: model formulation, recent developments, and future perspectives. – Geoscientific Model Development **8**, 2515–2551, DOI: 10.5194/gmd-8-2515-2015.

MARONGA, B., C. KNIGGE, S. RAASCH, 2020: An improved surface boundary condition for large-eddy simulations based on monin–obukhov similarity theory: Evaluation and consequences for grid convergence in neutral and stable conditions. – Boundary-Layer Meteorology (2), 297–325, DOI: 10.1007/s10546-019-00485-w.

MASON, P.J., 1989: Large-eddy simulation of the convective atmospheric boundary layer. – Journal of the Atmospheric Sciences (11), 1492–1516, DOI: 10.1175/1520-0469(1989)046<1492:lesotc>2.0.co;2.

MAUDER, M., R.L. DESJARDINS, E. PATTEY, Z. GAO, VAN R. HAARLEM, 2008: Measurement of the sensible eddy heat flux based on spatial averaging of continuous ground-based observations. – Boundary-Layer Meteorology (1), 151–172, DOI: 10.1007/s10546-008-9279-9.

MAUDER, M., T. FOKEN, J. CUXART, 2020: Surface-energy-balance closure over land: A review. – Boundary-Layer Meteorology , DOI: 10.1007/s10546-020-00529-6.

MOENG, C.H., J.C. WYNGAARD, 1988: Spectral analysis of large-eddy simulations of the convective boundary layer. – J. Atmos. Sci. **45**, 3573–3587, DOI: 10.1175/1520-0469(1988)045<3573:SAOLES>2.0.CO;2.

MODEROW, U., C. FEIGENWINTER, C. BERNHOFER, 2006: Estimating the components of the sensible heat budget of a tall forest canopy in complex terrain. – Boundary-Layer Meteorology (1), 99–120, DOI: 10.1007/s10546-006-9136-7.

ONCLEY, S.P., T. FOKEN, R. VOGT, W. KOHSIEK, H.A.R. DEBRUIN, C. BERNHOFER, A. CHRISTEN, VAN E. GORSEL, D. GRANTZ, C. FEIGENWINTER, I. LEHNER, C. LIEBETHAL, H. LIU, M. MAUDER, A. PITACCO, L. RIBEIRO, T. WEIDINGER, 2007: The energy balance experiment EBEX-2000. part i: overview and energy balance. – Boundary-Layer Meteorology (1), 1–28, DOI: 10.1007/s10546-007-9161-1.

RAASCH, S., M. SCHRÖTER, 2001: Palm - a large-eddy simulation model performing on massively parallel computers. – Meteorologische Zeitschrift **10**, 363–372, DOI: 10.1127/0941-2948/2001/0010-0363.

RAUPACH, M.R., R.H. SHAW, 1982: Averaging procedures for flow within vegetation canopies. – Boundary-Layer Meteorology (1), 79–90, DOI: 10.1007/bf00128057.

SAIKI, E.M., C.H. MOENG, P.P. SULLIVAN, 2000: Large-eddy simulation of the stably stratified planetary boundary layer. – Bound.-Lay. Meteorol. **95**, 1–30, DOI: 10.1023/A:1002428223156.

STEINFELD, G., M.O. LETZEL, S. RAASCH, M. KANDA, A. INAGAKI, 2007: Spatial representativeness of single tower measurements and the imbalance problem with eddy-covariance fluxes: results of a large-eddy simulation study. – Boundary-Layer Meteorology **123**, 77–98, DOI: 10.1007/s10546-006-9133-x.

STIPERSKI, I., M. CALAF, 2023: Generalizing monin-obukhov similarity theory (1954) for complex atmospheric turbulence. – Physical Review Letters (12), DOI: 10.1103/physrevlett.130.124001.

STOY, P.C., M. MAUDER, T. FOKEN, B. MARCOLLA, E. BOEGH, A. IBROM, M.A. ARAIN, A. ARNETH, M. AURELA, C. BERNHOFER, A. CESCATTI, E. DELLWIK, P. DUCE, D. GIANELLE, VAN E. GORSEL, G. KIELY, A. KNOHL, H. MARGOLIS, H. MCCAUGHEY, L. MERBOLD, L. MONTAGNANI, D. PAPALE, M. REICHSTEIN, M. SAUNDERS, P. SERRANO-ORTIZ, M. SOTTOCORNOLA, D. SPANO, F. VACCARI, A. VARLAGIN, 2013: A data-driven analysis of energy balance closure across FLUXNET research sites: The role of landscape scale heterogeneity. – Agricultural and Forest Meteorology 137–152, DOI: 10.1016/j.agrformet.2012.11.004.

SÜHRING, M., S. RAASCH, 2013: Heterogeneity-induced heat-flux patterns in the convective boundary layer: Can they be detected from observations and is there a blending height?—a large-eddy simulation study for the LITFASS-2003 experiment. – Boundary-Layer Meteorology **148**, 309–331, DOI: 10.1007/s10546-013-9822-1.

TAYLOR, G.I., 1938: The spectrum of turbulence. – Proceedings of the Royal Society of London. Series A - Mathematical and Physical Sciences (919), 476–490, DOI: 10.1098/rspa.1938.0032.

UHLENBROCK, J., RAASCH, S., HENNEMUTH, B, ZITTEL, P, MEIJNINGER, WML, 2004: Effects of land surface heterogeneities on the boundary layer structure and turbulence during LITFASS-2003: large-eddy simulations in comparison with turbulence measurements. – In: 6th Symposium on boundary layers and turbulence. American Meteorological Society, Portland (Maine), paper 9,3.

WANNER, L., F.D. ROO, M. SÜHRING, M. MAUDER, 2022: How does the choice of the lower boundary conditions in large-eddy simulations affect the development of dispersive fluxes near the surface?. – Boundary-Layer Meteorology (1), 1–27, DOI: 10.1007/s10546-021-00649-7.

WICKER, L.J., W.C. SKAMAROCK, 2002: Time-splitting methods for elastic models using forward time schemes. – Mon. Wea. Rev. **130**, 2008–2097, DOI: 10.1175/1520-0493(2002)130<2088:TSMFEM>2.0.CO;2.

WILLIAMSON, J.H., 1980: Low-storage runge-kutta schemes. – J. Comput. Phys. **35**, 48–56, DOI: 10.1016/0021-9991(80)90033-9.

WILSON, K., A. GOLDSTEIN, E. FALGE, M. AUBINET, D. BALDOCCHI, P. BERBIGIER, C. BERNHOFER, R. CEULEMANS, H. DOLMAN, C. FIELD, A. GRELLE, A. IBROM, B. LAW, A. KOWALSKI, T. MEYERS, J. MONCRIEFF, R. MONSON, W. OECHEL, J. TENHUNEN, R. VALENTINI, S. VERMA, 2002: Energy balance closure at FLUXNET sites. – Agricultural and Forest Meteorology (1-4), 223–243, DOI: 10.1016/s0168-1923(02)00109-0.

ZHOU, Y., M. SÜHRING, X. LI, 2023: Evaluation of energy balance closure adjustment and imbalance prediction methods in the convective boundary layer – a large eddy simulation study. – Agricultural and Forest Meteorology 109382, DOI: 10.1016/j.agrformet.2023.109382.